Thesis for the degree of Doctor of Philosophy

The Josephson parametric oscillator - From microscopic studies to single-shot qubit readout

Philip Krantz

Quantum Device Physics Laboratory
Department of Microtechnology and Nanoscience (MC2)
CHALMERS UNIVERSITY OF TECHNOLOGY
Göteborg, Sweden 2016

The Josephson parametric oscillator
- From microscopic studies to single-shot qubit readout

Philip Krantz, Göteborg, April 2016

ISBN 978-91-7597-374-6

Doktorsavhandlingar vid Chalmers tekniska högskola
Ny serie nr. 4055
ISSN 0346-718X

Technical Report MC2 - 337
ISSN 1652-0769

Quantum Device Physics Laboratory
Department of Microtechnology and Nanoscience (MC2)
Chalmers University of Technology
SE–412 96 Göteborg, Sweden
Telephone: +46 (0)31-772 1000

Front cover illustration: Animation of the sample layout used to demonstrate the single-shot readout of a superconducting qubit using a Josephson parametric oscillator.

Printed by Chalmers Reproservice, Chalmers University of Technology
Göteborg, Sweden, April 2016

The Josephson parametric oscillator
- From microscopic studies to single-shot qubit readout
PHILIP KRANTZ
Department of Microtechnology and Nanoscience
Chalmers University of Technology
Göteborg, Sweden 2016

Abstract

Circuit quantum electrodynamics (cQED) is a prominent platform for quantum information processing, in which microwave photons are confined into resonant cavities coupled to superconducting quantum bits (qubits). The large effective dipole moment of the qubit, in combination with the high energy density of the quasi 1-D resonator allow these systems to enter the so-called strong coupling regime. The quantum state of the qubit can then be assessed by probing the frequency of the resonator, protecting the qubit from otherwise losing its energy to the environment. However, eventhough this so-called dispersive readout technique has proven useful, it is often in itself insufficient to render single-shot readout performance — one of the crucial tasks required for realizing a quantum computer.

This thesis describes the demonstration of a single-shot readout technique for superconducting quantum bits, based on coupling the qubit to a frequency-tunable resonator. The backbone of our device is a 5 GHz quarter-wavelength coplanar waveguide resonator, terminated at one end by a non-linear inductance provided by a superconducting quantum interference device (SQUID). The SQUID acts as a flux-controlled boundary condition, which effectively changes the electrical length of the resonator. This enables the modulation of the resonant frequency by coupling microwave magnetic flux into the SQUID, using an on-chip transmission line. The modulation occurs on a timescale much faster than the photon loss out of the resonator and if the pump strength exceeds a threshold value set by the damping rate of the resonator, an intense photon field will build up inside the resonator — known as "parametric oscillations".

By heterodyne detection of the output signal from the Josephson parametric oscillator (JPO), we first extracted two leading nonlinear effects of the system (dominating in different limits of applied magnetic flux). Next, we couple a qubit to the JPO and demonstrate that we can encode its quantum state onto the strong output field of the parametric oscillator (or lack thereof), rendering a signal-to-noise ratio sufficient for single-shot state detection and therefore also obviating a quantum-limited parametric amplifier.

The thesis also contains results from microscopic studies of the Josephson junctions, which we use to provide the necessary nonlinearities in the above mentioned devices. In particular, we show how the microstructure of the barrier layer and its atomic composition can be used to infer important electrical properties of the junctions. This knowledge allows us to better tailor the properties of Josephson-based devices.

Keywords: Superconducting circuits, resonators, parametric oscillators, Josephson junction, SQUID, quantum bit, quantum information, circuit quantum electrodynamics, pumpistor

This thesis is dedicated to
Iris Vilhelmina Krantz

List of appended publications

This thesis is based on the work contained in the following publications:

I. **Investigation of nonlinear effects in Josephson parametric oscillators used in circuit QED**
P. Krantz, Y. Reshitnyk, W. Wustmann, J. Bylander, S. Gustavsson, W. D. Oliver, T. Duty, V. Shumeiko, and P. Delsing
New Journal of Physics **15**, 105002 (2013).

II. **Single-shot read-out of a superconducting qubit using a Josephson parametric oscillator**
P. Krantz, A. Bengtsson, M. Simoen, S. Gustavsson, V. Shumeiko, W. D. Oliver, C. M. Wilson, P. Delsing, and J. Bylander
Nature Communications **7**, 11417 (2016).

III. **The pumpistor: a linearized model of a flux-pumped superconducting quantum interference device for use as a negative-resistance parametric amplifier**
K.M. Sundqvist, S. Kintaş, M. Simoen, **P. Krantz**, M. Sandberg, C.M. Wilson, and P. Delsing
Applied Physics Letters **103**, 102603 (2013).

IV. **Characterization of a multimode coplanar waveguide parametric amplifier**
M. Simoen, C. W. S. Chang, **P. Krantz**, J. Bylander, W. Wustmann, V. Shumeiko, P. Delsing, and C. M. Wilson
Journal of Applied Physics **118**, 154501 (2015)

V. **Direct observation of the thickness distribution of ultra thin AlO_x barriers in $Al/AlO_x/Al$ Josephson junctions**
L. J. Zeng, S. Nik, T. Greibe, **P. Krantz**, C. M. Wilson, P. Delsing, and E. Olsson
Journal of Physics D: Applied Physics **48**, 395308 (2015).

VI. **The atomic details of the interfacial interaction between the bottom electrode of $Al/AlO_x/Al$ Josephson junctions and HF-treated Si substrates**
L. J. Zeng, **P. Krantz**, S. Nik, P. Delsing, and E. Olsson
Journal of Applied Physics **117**, 163915 (2015).

Publications outside of the scope of this thesis:

VII. **Correlation between Al grain size, grain boundary grooves and local variations in oxide barrier thickness of $Al/AlO_x/Al$ tunnel junctions by transmission electron microscopy**
S. Nik, **P. Krantz**, L. J. Zeng, T. Greibe, H. Pettersson, S. Gustafsson, P. Delsing, and E. Olsson
Submitted manuscript (2016).

VIII. **Fabrication of large dimension aluminum air-bridges for superconducting quantum circuits**
M. Abuwasib, **P. Krantz**, and P. Delsing
Journal of Vacuum Science and Technology B **31**, 031601 (2013).

IX. **Niobium and aluminum Josephson junctions fabricated with a damascene CMP process**
Abelaziz Ramzi, Serge A. Charlebois, and **P. Krantz**
Physics Procedia **36**, 211-216 (2012).

X. **Coupling of an erbium spin ensemble to a superconducting resonator**
M. U. Staudt, I-C Hoi, **P. Krantz**, M. Sandberg, M. Simoen, P. Bushev, N. Sangouard, M. Afzelius, V. S. Shumeiko, G. Johansson, P. Delsing, and C. M. Wilson
Journal of Physics B: At., Mol. and Opt. Phys. **45**, 124019 (2012).

XI. **An on-chip Mach-Zehnder interferometer in the microwave regime**
S. Schuermans, M. Simoen, M. Sandberg, **P. Krantz**, C. M. Wilson, and P. Delsing
IEEE Transactions on Applied Superconductivity **21**, no. 3 (2011).

Acknowledgements

The work contained in this thesis would not have been possible without the assistance and support from many people. First of all, I would like to express my sincere gratitude to my supervisor and examiner Prof. Per Delsing for giving me the opportunity to carry out my doctoral studies in his group. Per is a very motivating and inspiring leader, who always has an open door and mind for discussing new ideas and providing important guidance. Second, I would like to thank my co-supervisor Associate Prof. Jonas Bylander for taking me on as a visiting student at MIT, where I learned a lot about measurement techniques. Also, despite of your heavy workload you have always helped me out when I needed it the most. You are truly a good supervisor and friend.

Thank you Michaël, Arsalan, and Andreas for being the best possible friends, both in the office and outside. Thank you Andreas for being my co-pilot during the last year. It has been very fun working with you and I wish you all the best in the future. Many thanks goes all the people at QDP for creating a nice work environment: Mathieu, Matthias, Martin, Thomas, Samuel, André, Io-Chun, Seckin, Sebastian, Niclas, Kyle, Ida-Maria, Maria, Ben, Astghik, Marco, Reza, Thilo, Sophie, Simon, Thomas, Andrey, Saroj, Sergey, Arseniy, Avgust, Tord, Leonid, Elsebeth, Floriana, Jie, Alexei, Luca, Baladitya, Maxim, Riccardo, Pier Paolo, Minshu, David, Grigory, Gustav, Jan, Staffan, Lars, Maria, and Susannah.

I am also very grateful for all the theory discussions I had with the people at Applied Quantum Physics laboratory: Vitaly, Waltraut, Göran, Anton, and Lars. Without all of you, I would not know much about our measured devices. Many thanks goes to the staff of the Nanofabrication laboratory for all the processing related assistance, especially Henrik, Kaija, John, and Mats.

In addition to all of you mentioned above, there are several people with whom we got the honor to collaborate: The group at Massachusetts Institute of Technology: Terry Orlando, Will Oliver, Simon Gustavsson, Xiaoyue Jin, and Fei Yan. The group at University of New South Wales and University of Queensland in Australia: Tim Duty, Yarema Rushitnyk, and Jean-Loup Smirr. The Microscopy group at Chalmers: Samira Nik, Lunjie Zeng, and Eva Olsson.

Finally, all my love to my family: Sören, Inger, Linda, Henrik, and Tove as well as to my wonderful wife Eli and my new family: Saide, Setare, and Afsar. Thank you so much for your endless love and for never stop believing in me. Without you, I would not be where I am today!

Philip Krantz
Göteborg, April, 2016

List of symbols

Constants

$\hbar$	Reduced Planck constant	$h/2\pi \approx 1.1 \times 10^{-34}$ Js
e	Elementary charge	$\approx 1.6 \times 10^{-19}$ C
c	Speed of light in vacuum	$\approx 3 \times 10^{8}$ m/s
k_{B}	Boltzmanns constant	$\approx 1.4 \times 10^{-23}$ J/K
Φ_0	Magnetic flux quantum	$h/2e \approx 2.0 \times 10^{-15}$ Wb
R_{Q}	Quantum of resistance	$h/(4e^2) = R_K/4 \approx 6.5\mathrm{k}\Omega$
m	Electron mass	$\approx 9.11 \times 10^{-31}$ kg

Chapter 1: Introduction

$\psi(\mathbf{r})$	Superconducting wave function
$\varphi(\mathbf{r})$	Phase of the superconducting wavefunction
$\rho(\mathbf{r})$	Pair density
I_{c}	Critical current of Josephson junction
φ	Phase difference across Josephson junction ($\varphi_1 - \varphi_2/2$)
Φ_{dc}	dc magnetic flux
Φ_{ac}	ac magnetic flux
L_{s}^0	Inductance of SQUID at zero-flux and bias ($\Phi_0/(2\pi I_c)$)
γ	Complex propagation constant
Z_{c}	Characteristic impedance ($\sqrt{L/C}$)
v_{ph}	Phase velocity ($1/\sqrt{LC}$)
g,w	Gap and center conductor width of CPW
l	Length of resonator
λ	Wavelength of resonator

Chapter 2: Theory

The tunable resonator

C_{c}	Coupling capacitor
f_0	Resonance frequency ($\omega_0/2\pi$)
ϵ_{eff}	Effective dielectric constant
S_{11}	Complex reflection coefficient ($\lvert S_{11}\rvert \mathrm{e}^{i\arg(S_{11})}$)
Q_{i}	Internal quality factor ($\omega_r/2\Gamma_R$)
Q_{e}	External quality factor ($\omega_r/2\Gamma_0$)
Q_{tot}	Total quality factor ($(1/Q_{\mathrm{i}} + 1/Q_{\mathrm{e}})^{-1} = \omega_r/2\Gamma$)
δf	Probe−resonator detuning ($f - f_0$)
F	dc-flux bias ($\pi\Phi_{\mathrm{dc}}/\Phi_0$)
γ_0	Inductive participation ratio (L_{s}^0/Ll)
$\omega_{\lambda/4}$	Bare angular resonator frequency
ω_p	Angular parametric pump frequency

The parametric oscillator

Φ_{i}	Canonical flux at node i
ϵ	Pump amplitude
ϵ'	Normalized pump amplitude ($\epsilon Q_{\mathrm{tot}}/\omega_r\omega_p$)
δ	Pump−resonator detuning ($\omega_p/2-\omega_r$)
δ'	Normalized pump−resonator detuning (δ/Γ)
α	Duffing nonlinearity parameter
α'	Normalized Duffing parameter ($3\alpha/4\Gamma\omega_p$)
q_1,q_2	In-phase and quadrature voltages
g	Parametric voltage gain
β	Pump−induced nonlinearity parameter
θ_p,θ_s	Pump and signal phases
$\Delta\theta$	Phase angle between pump and signal ($2\theta_s-\theta_p$)

The transmon qubit

C_{g}	Gate capacitance
C_{s}	Shunt capacitance
C_{J}	Josephson capacitance
C_Σ	Total qubit capacitance ($C_{\mathrm{g}}+C_{\mathrm{s}}+C_{\mathrm{J}}$)
V_{g}	Gate voltage
Δ	Superconducting gap (1.76 k_BT_c)
n_{g}	Reduced gate charge ($C_{\mathrm{g}}V_{\mathrm{g}}/2e$)
E_{c}	Charging energy ($e^2/2C_\Sigma$)
E_{J}	Josephson energy ($\Phi_0 I_{\mathrm{c}}/2\pi$)
R_{n}	Normal state resistance
$\|0\rangle$,$\|1\rangle$	Ground- and first excited qubit states
ω_a	Qubit transition frequency
α_r	Relative anharmonicity ($(E_{12}-E_{01})/E_{01}$)
$\hat{\sigma}_z$	Pauli's z-matrix ($\|0\rangle\langle 0\|-\|1\rangle\langle 1\|$)
$\hat{a}^\dagger$,$\hat{a}$	Creation and annihilation operators
$\hat{\sigma}_+$,$\hat{\sigma}_-$	Atomic transition operators ($\|1\rangle\langle 0\|, \|0\rangle\langle 1\|$)
$\hat{n}$	Photon number operator ($\hat{a}^\dagger\hat{a}$)
g, g_{01}	Qubit−resonator coupling rate
Ω_R	Vacuum Rabi frequency ($\sqrt{n}g/\pi$)
Δ	Qubit−resonator detuning ($\omega_a-\omega_r$)
T_1	Qubit relaxation time
T_2	Qubit dephasing time

Chapter 3: Experiments

P_{ox}	Oxidation pressure
t_{ox}	Oxidation time
η	Evaporation angle

The microstructure of Josephson junctions

$\langle l \rangle$	Average junction thickness
σ_l	Standard deviation of junction thickness
$P_{90\%}$	Active junction area accounting for 90 % of its conductance
λ	Barrier attenuation length
ϕ	Barrier height

Chapter 4: Results

A	Intra−resonator field amplitude ($\|A\|^2$ number of photons)
B	Resonator probe field ($\|B\|^2$ has units of photons/s)
C	Outgoing field ($\|C\|^2$ has units of photons/s)

List of abbreviations

cQED	circuit Quantum ElectroDynamics
Qubit	Quantum bit
SQUID	Superconducting QUantum Interference Device
SEM	Scanning Electron Microscope
CPW	CoPlanar Waveguide
TEM	Transverse ElectroMagnetic (or Transmission Electron Microscope)
STEM	Scanning TEM
GIF	Gatan Imaging Filter
EELS	Electron Energy Loss Spectroscopy
EFTEM	Energy Filtering TEM
ELNES	Energy Loss Near Edge Structure
CPB	Cooper Pair Box
CNC	Computer Numerical Control
PCB	Printed Circuit Board

Table of Contents

Chapter 1

1 Introduction

1.1 Motivation

In 1982, R. P. Feynman [1] suggested an alternative to using "classical" computers when simulating and solving problems of quantum mechanical nature. He argued that quantum systems could be modeled with much greater efficiency by using a processor whose architecture, in itself, is based on the laws of quantum mechanics. This was the starting point for the quest of the so-called *quantum computer*, where quantum information would be encoded into quantum bits (qubits). By utilizing properties such as superposition and entanglement associated with quantum objects, this processor would not only be able to perform parallel operations offering new ways to substantially increase the processing power compared with its classical counterpart, but also vastly change the ways of which we think around computation.

Even though several algorithms have been created for quantum computation, the development of its hardware has proven to be a big challenge. The practical obstacle is due to the issue of isolating qubits from their environment[1], while maintaining sufficient control to coherently manipulate them. In fact, as the number of qubits increase in the processors, the field of quantum information technology gradually evolves from being physics oriented into an engineering field of research. Before a large-scale quantum processor can be realized, there are a number of crucial tasks that all need to be solved [2]. This thesis is devoted to solving one such task, namely to develop an efficient detector efficiently able to read out the state of the qubit, with high fidelity and in a single measurement – known as single-shot readout.

The foundation of the theory behind the system described in this thesis, introduced by P. A. M. Dirac almost one century ago and developed by R. P. Feynman about seventy years ago, is known as *quantum electrodynamics* (QED) – a quantum mechanical theory of the interaction between light and matter – further discussed in section 1.4. Among the different technological platforms that have been developed for processing quantum information, we utilize circuit quantum electrodynamics (cQED) [3,4], in which the qubits are realized by lithographically defined superconducting circuits on a chip, also refered to as *artificial atoms* due to their similar anharmonic energy spectra as found in real atoms. These artificial atoms are de-

[1] Since any unwanted interaction with the system will extract information and thus decohere the system.

signed such that they interact with light of a specific wavelength in the microwave regime. To increase the interaction strength between the light field and the artificial atoms, the light is confined within superconducting resonators to which the atoms are coupled[2].

If the qubit is strongly coupled to the resonator, *i.e.* when the coupling rate between the two is dominant over other time scales in the system, the qubit exerts a state-dependent shift of the resonator frequency that can be used to assess the state of the qubit, without directly probing the qubit. This technique is known as *dispersive readout* and is commonly used in cQED. However, when using a linear resonator, this method suffers from poor performance in terms of fidelity since it requires a low-power probe signal. To overcome this obstacle, researchers have exploited the nearly lossless nonlinearity of superconducting Josephson junctions to develop various amplification schemes, adding only the minimum amount of noise allowed by the laws of quantum mechanics.

This thesis is about a new single-shot readout scheme, based on mapping the state of the qubit onto the dynamics of a Josephson parametric oscillator (JPO), schematically depicted in Fig. 1.1. Our JPO consists of a quarter wavelength resonator, blue in Fig. 1.1(a), which we short to ground via two parallel Josephson junctions, forming a *superconducting quantum interference device*, (SQUID). By threading a magnetic-flux through the loop of the SQUID, we can tune the Josephson inductance of the SQUID and therefore even tune the resonant frequency of the JPO along a cosine-shaped curvature. If we, in addition to a fixed dc-flux bias, also introduce an on-chip fast tuning line, its frequency can be modulated fast (at twice the frequency of the resonator) around a static flux bias point, the strong field of so-called parametric oscillations build up inside the resonator. By coupling a qubit (red in Fig. 1.1(a)) to the JPO, we show that we can operate the system in such a way that the dynamics of the qubit gets mapped onto the parametric oscillator, yielding a strong enough output to support single-shot discrimination of the two states of the qubit, see Fig. 1.1(b)-(c).

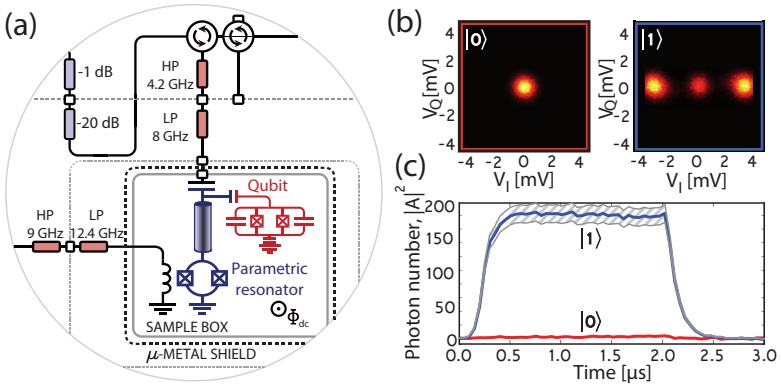

Figure 1.1: **(a)** Schematic drawing the cryogenic reflectometry setup for the JPO. **(b)** IQ-histograms of the parametric oscillation output from the device, where the excited qubit state $|1\rangle$ (in blue) is encoded in high oscillation amplitude, whereas the ground state $|0\rangle$ (in red) corresponds to an empty resonator. **(c)** Intra-resonator field amplitude for the two states as a function of time.

[2]The superconducting resonator also acts as a bandpass filter, protecting the qubit from spurious radiation of light with frequencies different than the mode of the resonator.

1.2 Superconductivity

In 1911, H. K. Onnes [5] made a ground breaking discovery in physics. He concluded that the electrical resistance of mercury abruptly dropped by several orders of magnitude when the metal was cooled down below a critical temperature, T_c. This phenomenon, now known as *superconductivity* turned out to be true also for many other metals, only at different critical temperatures. In his lectures on physics, Feynman discusses in short terms the origin to why superconductivity is observed for many metals [6]. The interaction between the electrons in the metal and the vibrations of its atom lattice (phonons) give rise to small effective attractions between the electrons. Therefore, it is energetically favorable for them to form pairs rather than staying separated. This has the remarkable effect that the electrons, which are Fermi particles (fermions) with spin 1/2, will become Bose particles (bosons) as they appear in such a pair (with a total spin of zero). Intuitively, two negatively charged particles would repell each other. However, the two electrons get coupled via a positively charged ion lattice through phonons induced by the electrons. This has the consequence that the electron pairs, known as Cooper-pairs, will form a condensate[3].

Since the superconducting state of a metal takes place at very low temperatures, Cooper-pairs will be bound to stay in their lowest energy state. The Cooper-pair bonds are, however, weak and are therefore easily broken if only a small thermal energy acts on them. The thermal energy needed to break up the Cooper-pairs is given by the energy gap 2Δ and is related to the critical temperature for the superconductor at hand. The wave function of the Cooper-pairs in their lowest energy state can be written

$$\psi(\mathbf{r}) = \sqrt{\rho(\mathbf{r})}\mathrm{e}^{\mathrm{i}\varphi(\mathbf{r})}, \tag{1.1}$$

where $\rho(\mathbf{r})$ is the pair density and $\varphi(\mathbf{r})$ is the quantum mechanical phase.

The peculiar properties of superconductors that have been discovered during the past century, have opened completely new fields of research. One of the most important features is the tunneling of these Cooper-pairs through thin barriers, separating two superconductors. This element, known as the *Josephson junction*, allows for the creation of non-linear, nearly dissipationless circuit elements and is the topic of next section. For more elaborate explanation of superconductivity, the reader is referred to textbooks on the topic, such as [7, 8].

1.2.1 The Josephson effects

Within the context of the superconducting devices presented in this thesis, as well as all other theses on circuit QED, the Josephson junction is the most fundamental building block from which most other non-linear properties originate.

In 1962, about fifty years after the discovery of superconductivity, B. D. Josephson made the theoretical prediction that when two superconductors are put in close vicinity of each other, forming a weak link known as a Josephson junction, a zero-voltage tunneling current of Cooper-pairs could flow through the junction [9], see Fig. 1.2(a). In order for the tunneling to take place, the thickness of the insulating

[3] Since the Cooper-pairs are bosons, there is no limit to how many particles can occupy the same state.

barrier needs to be thin enough for the wave functions in Eq. (1.1) of each superconducting electrode to overlap with each other as they decay exponentially into the barrier, see Fig. 1.2(b). Josephson described this tunneling phenomenon in terms of two effects:

The *dc Josephson effect* relates the tunneling current, I, flowing through the junction with the phase difference, φ, across it

$$I = I_c \sin(\varphi), \tag{1.2}$$

where I_c is the critical current of the junction, *i.e.* the maximum super current it can support before switching into its resistive branch. The *ac Josephson effect* relates the voltage across the junction, V, with the time-derivative of the phase difference

$$V = \left(\frac{\hbar}{2e}\right)\frac{d\varphi}{dt} = \left(\frac{\Phi_0}{2\pi}\right)\frac{d\varphi}{dt}, \tag{1.3}$$

where $\Phi_0 = h/(2e)$ denotes the magnetic flux quantum.

In this thesis, the Josephson junctions are implemented in parallel pairs, forming so-called Superconducting Quantum Interference Devices, (SQUIDs). We extend Eq. (1.2) and (1.3) to this case, see Fig. 1.2(c), with the junctions denoted "1" and "2". The first Josephson relation in (1.2) now gets modified to

$$I = I_{c1}\sin(\varphi_1) - I_{c2}\sin(\varphi_2). \tag{1.4}$$

Due to the fact that flux in the superconducting loop is quantized [8], we get the following quantization condition

$$\varphi_1 + \varphi_2 + 2\pi\frac{\Phi}{\Phi_0} = 2\pi n, \tag{1.5}$$

where n is the number of flux quantum in the loop. By choosing the case of one flux quantum, $(n = 1)$, and using relations (1.4) and (1.5), the total current flowing through the two junctions can be expressed as

$$\begin{aligned} I = (I_{c1} + I_{c2})\cos\left(\pi\frac{\Phi}{\Phi_0}\right)\sin\left(\frac{\varphi_1 - \varphi_2}{2}\right) - \\ (I_{c1} - I_{c2})\sin\left(\pi\frac{\Phi}{\Phi_0}\right)\cos\left(\frac{\varphi_1 - \varphi_2}{2}\right). \end{aligned} \tag{1.6}$$

For the application throughout this thesis, the critical currents needed allow us to make the junction areas relatively large as compared with the grain size of the Aluminum. The two junctions can therefore be fabricated almost identical, yielding $I_{c1} \approx I_{c2}$. Thus, relation (1.6) reduces to only its first term

$$I = I_c \cos\left(\pi\frac{\Phi}{\Phi_0}\right)\sin(\varphi), \tag{1.7}$$

where we have introduced an effective critical current $I_c = I_{c1} + I_{c2} = 2I_{c1}$ and an effective phase difference $\varphi = (\varphi_1 - \varphi_2)/2$.

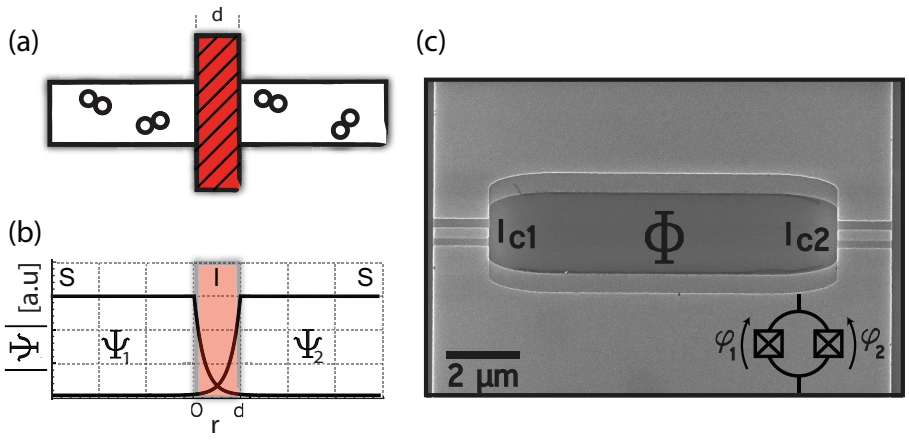

Figure 1.2: **(a)** Schematic drawing of a Josephson junction composed of two superconducting electrodes, separated by a thin insulating barrier of thickness d. **(b)** The wavefunctions of the two identical superconductors in **(a)**. The exponential decay of the wavefunctions for the electrodes have a small overlap, allowing a supercurrent to flow through the junction. **(c)** Scanning electron micrograph of an Al SQUID, fabricated on a SiO_2 substrate. The two Josephson junctions have critical currents I_{c1} and I_{c2}, respectively. **Inset:** Circuit element representation of a SQUID.

1.2.2 The Josephson nonlinear inductance

Another important feature of the Josephson junction is that it accumulates energy from the tunneling Cooper-pairs, known as *Josephson energy*, resulting in a non-linear inductance. We can derive this *Josephson inductance* of the SQUID from the time derivative of the current flowing through it,

$$\frac{dI}{dt} = I_c \left|\cos(\pi\Phi/\Phi_0)\right| \cos(\varphi) \frac{d\varphi}{dt}, \tag{1.8}$$

where the absolute value of the flux term can be dropped when considering a single flux quantum. Using Eq. (1.3) and re-arranging the terms of Eq. (1.8), the voltage across the junction can be related with the time-derivative of the current,

$$V = \frac{\hbar}{2e} \frac{1}{I_c \left|\cos(\pi\Phi/\Phi_0)\right| \cos(\varphi)} \frac{dI}{dt}. \tag{1.9}$$

Recalling that $V = L(dI/dt)$, the Josephson inductance can by identified as

$$L_s = \frac{\hbar}{2e} \frac{1}{I_c \left|\cos(\pi\Phi/\Phi_0)\right| \cos(\varphi)} = \frac{L_s^0}{\left|\cos(\pi\Phi/\Phi_0)\right| \cos(\varphi)}, \tag{1.10}$$

where $L_s^0 = \hbar/(2eI_c) = \Phi_0/(2\pi I_c)$ is the SQUID inductance at zero applied flux and zero bias current.

1.3 Microwave theory of transmission lines

When designing a microscopic superconducting circuit, operated at microwave frequencies, an essential aspect of the work is dedicated to modelling its geometrical dimensions. The transmission lines used in this thesis are coplanar waveguides (CPW), named after its inventor C. P. Wen [10]. This design resembles that of a flattened coaxial cable, with a center conductor of width, w separated from ground planes on each side by gaps of width, g, see Fig. 1.3(a). Just like in the coaxial cable, the propagating microwaves in the line give rise to transverse electromagnetic (TEM) waves. We can study the properties of the transmission line using the telegraph equations [11], where the transmission line is represented by a series of infinitesimally short segments of length $dz \to 0$, see Fig. 1.3(b). Each segment is composed of a distributed resistance and inductance represented by a series resistor, Rdz, and inductor, Ldz, respectively. The dielectric material separating the center conductor from the ground planes is represented by a shunt resistor with conductance, Gdz and the capacitance by a shunt capacitor, Cdz. Thus, R,L,G, and C represent the circuit quantities per unit length dz. The voltage and current at position z along the line can be written as

$$\begin{cases} V(z) = V^+ \mathrm{e}^{-\gamma z} + V^- \mathrm{e}^{\gamma z} \\ I(z) = I^+ \mathrm{e}^{-\gamma z} - I^- \mathrm{e}^{\gamma z} \end{cases}, \tag{1.11}$$

where $\gamma = \sqrt{(R + i\omega L)(G + i\omega C)}$ is the complex propagation constant at the angular microwave frequency, ω. $V^{\pm}, I^{\pm}$ denote the voltage and current amplitudes of the waves travelling forward (+) and backward (-), respectively. From these, the characteristic impedance of the line can be expressed as

$$Z_c = \frac{V^+}{I^+} = \sqrt{\frac{R + i\omega L}{G + i\omega C}}. \tag{1.12}$$

For a superconducting transmission line, we can assume very small losses. Thus, the resistors can be neglected and the characteristic impedance and phase velocity can be expressed as

$$Z_c \approx \sqrt{\frac{L}{C}}, \qquad v_{\mathrm{ph}} = \frac{1}{\sqrt{LC}}. \tag{1.13}$$

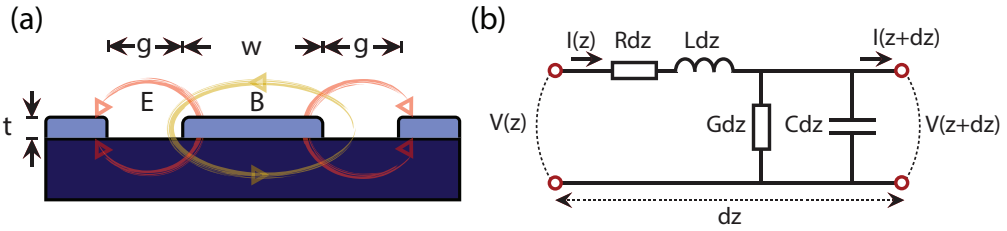

Figure 1.3: **(a)** Cross-section of a coplanar waveguide design with metal thickness t, center conductor of width w, separated to the ground planes by gaps of width g. The electric field from the center conductor to ground is marked with red, whereas the magnetic field surrounding the center conductor is marked with yellow. **(b)** Lumped-element representation of a short unit segment of the transmission line.

1.4 Circuit quantum electrodynamics

The theory of Quantum Electrodynamics (QED) was introduced by P. A. M. Dirac in the 1920s [12], and describes the interaction between electromagnetic radiation and matter. In his work, Dirac pioneered the view of the radiation and atom as a unified system and computed the coefficient of spontaneous emission of atoms, which agreed with Einstein's previously presented theory [13]. Inspired by Dirac's and Einstein's work, S-I Tomonaga [14], J. Schwinger [15], and R.P. Feynman [16] further developed the theory of QED for which they were awarded the Nobel prize in physics 1965.

In nature, however, the interactions between individual atoms and photons are very weak due to the large mode volume of the field in combination with the small dipole moment of the atom, imposing an obstacle for studying these phenomena experimentally. This practical issue was solved as cavity QED evolved [17, 18], where Rydberg atoms with large moments are introduced between two highly reflective mirrors, forming a resonant cavity supporting only specific frequency modes as set by the distance between the mirrors, see Fig. 1.4(a). At the resonant frequency of the cavity, an enhancement of the field inside the resonator yields a strong photon-atom coupling due to the fact that the photons get many chances to interact with the atoms. In addition, the mode structure of the resonator protects the atoms from vacuum fluctuations at off-resonant frequencies and thereby reduces spontaneous emission. These high quality resonators, in combination with the large dipole moment of the Rydberg atoms, thus enable the observation of coherent energy exchange between the cavity and the atoms. In fact, cavity QED offers the possibility to construct the fundamental building block of a quantum processor, where the computational basis is encoded into two eigenstates of the atomic energy spectrum [1]. However, in order to realize a large scale processor, it is favorable to be able to completely control and tailor the properties of the atoms as well as storing them for a long time.

In 2004, cavity QED and quantum optics technologically merged with the experimental advances of superconducting circuits fabricated using nanofabrication techniques. The result was the field of circuit QED (cQED) [3, 4], where the optical cavities were replaced with microwave resonators with resonant frequencies in the GHz-range, see Fig. 1.4(b). In turn, the atoms were replaced by mesoscopic artificial objects with atom-like energy spectra. These are referred to as superconducting qubits or artificial atoms. The quasi one-dimensional architecture of the transmission line resonators gives a very small mode volume. This allows the interaction between the atom and resonator to enter into the strong coupling regime, where the coupling rate is much greater than both the rate at which photons leaves the resonator and the quantum coherence time of the artificial atom.

Circuit QED has over the past decade proven to be a promising platform for realizing various building blocks needed to develop a large scale quantum computer. One of the necessary components required is a reliable and effective readout scheme, to assess the states of the qubits. In this work, a superconducting qubit is coupled to a Josephson parametric oscillator, which acts as a readout device to measure the state of the qubit in a single-shot.

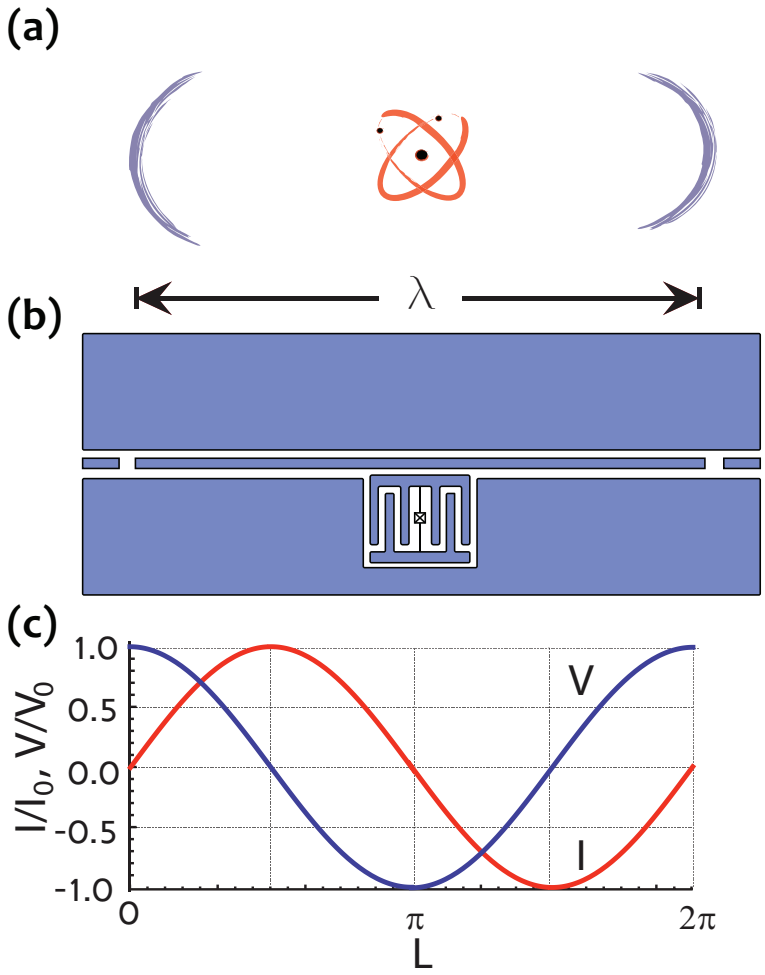

Figure 1.4: **(a)** Cartoon of cavity QED where an atom is stored in an optical cavity defined in between two highly reflective mirrors. **(b)** The corresponding picture in circuit QED, where the atom is replaced by an artificial atom and the resonator is defined by a piece of CPW transmission line, in this case open at both ends.**(c)** The voltage (in blue) and current (in red) as function of position of the resonator. The artificial atom has the strongest capacitive coupling to the resonator where the voltage has a maximum.

1.5 Structure of the thesis

The thesis is organized as follows: In Chapter 2, the necessary theoretical framework is introduced, starting out with the construction of superconducting resonators and how these are characterized using microwave photons. Next, we extend the system to the frequency tunable resonator and introduce the notion of parametric pumping in the JPO. In Appended paper I, the two dominant nonlinearities of the JPO are studied and characterized. Then, we introduce a linearized impedance model of the flux-pumped parametric resonator, known as *the pumpistor*, covered in Appended paper III. In the end of this chapter, we couple a superconducting transmon qubit to the JPO, operated as a sensitive detector of the qubit state in Appended paper II. In this chapter, the reader is also introduced to dispersive read-out of the qubit as well as how we assess the different quantum coherence times from the qubit. The chapter is then closed with a short theoretical description of the mechanism used for the Josephson parametric oscillator readout.

In Chapter 3, the experimental aspects of the projects are outlined. Here, the reader is first introduced to the methods used to design the parametric device. Then, the main fabrication methods are described, followed by a closer look at the microstructure of the most important part of our circuits, namely the Josephson junctions. The microstructure details of Josephson junctions is analyzed in Appended papers V and VI. This chapter is then concluded with a brief description of the cryogenic measurement techniques used to characterize the parametric samples.

In Chapter 4, the main results from the devices are presented. First, the static characterization techniques, when the resonator frequency is changed using a dc-coil. Here, we also describe how the Duffing nonlinearity of the system can be used to calibrate the gain of the amplifier chain, necessary to assess the resonator photon number. Second, the parametric character of the device is revealed using an on-chip rf line to modulate the resonant frequency of the resonator. Then follows an introduction to the analysis performed for the Josephson parametric oscillator readout. This chapter is then closed by a brief overview of the measurements on the multimode parametric amplifier.

Finally, in Chapter 5 we conclude the thesis with a summary and present an outlook, discussing potential future directions based on this work.

Chapter 2

Background

The purpose of this chapter is to convey a solid theoretical background, so that the reader can gain insight into the main results presented in the appended papers, in particular the Josephson parametric oscillator (JPO) used as a single-shot qubit readout in a circuit QED setting.

The beginning of this chapter is devoted to the basic properties of linear superconducting resonators. Next, a couple of Josephson junctions are added to the resonator, making it tunable in frequency by means of an applied magnetic flux. Three different theoretical frameworks for the parametric properties of the device are presented. To illustrate the main properties of the circuit, we first follow the formalism and analysis by C. M. Wilson *et al.* [19], based on quantum network theory developed by B. Yurke and J. S. Denker [20]. After that, we make the connection to the field amplitude formalism used in Appended papers I and II, developed by Wustmann and Shumeiko [21].We then make a side step and introduce a linearized impedance model of a parametrically pumped resonator called "the pumpistor" (Appended paper III), developed by K. M. Sundqvist *et al.* [22] and suitable for more complex implementation of the parametrically pumped SQUID. Finally, we introduce the transmon superconducting qubit, before the chapter is concluded with a brief outline about the underlying phenomena of the Josephson parametric oscillator readout (Appended paper II).

2.1 Superconducting resonators

One of the fundamental building blocks used in circuit QED is the superconducting resonator. Throughout this thesis, we use quarter wavelength resonators, realized by a coplanar waveguide transmission line of length, $l = \lambda/4$, see Fig. 2.1(a). In one end we interrupt the center conductor and thus define a coupling capacitor, C_c, through which the resonator is probed using reflectometry measurements. In the other end, the center conductor is shorted to ground.

Even though the distributed resonator has multiple modes, its fundamental resonant frequency, f_0, can be modeled using a single-mode, lumped element representation of the circuit, see Fig. 2.1(b), when it is probed close to its fundamental mode frequency. The resonant frequency can be written as

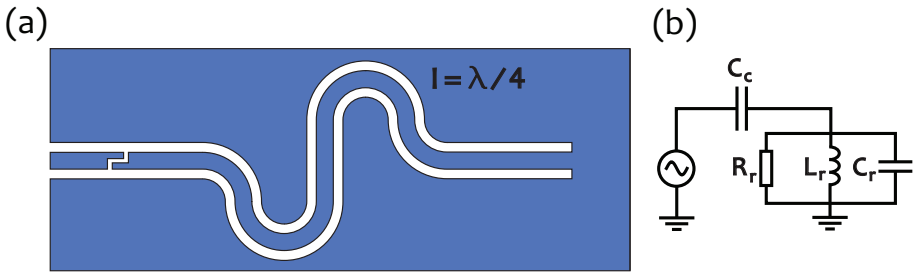

Figure 2.1: **(a)** The quarter-wavelength resonator consists of a CPW transmission line, defined between a coupling capacitor, C_c, in one end and shorted to ground in the other. **(b)** Close to the resonant frequency, the response of the system can be modeled using a lumped element LCR resonator.

$$f_0 = \lambda^{-1} v_{\text{ph}} = \frac{c}{4l\sqrt{\epsilon_{\text{eff}}}}, \tag{2.1}$$

where the phase velocity, $v_{\text{ph}} = c/\sqrt{\epsilon_{\text{eff}}}$ is expressed in terms of the effective dielectric constant, ϵ_{eff}, set by the dielectric environment surrounding the resonator and the speed of light in vacuum, c.

2.1.1 Reflected microwave response

In this section, we will briefly discuss how we can extract the fundamental properties of the resonator by fitting the measured reflected magnitude, $|S_{11}|$, and phase, $\arg(S_{11})$. For the full derivation, the reader is referred to Appendix B.

From the reflection coefficient, S_{11}, we extract the fundamental resonance frequency, f_0, and two quality factors of the system, *i.e.* the resonators ability to store energy. The total (or loaded) quality factor, Q_{tot} is defined as the ratio between stored to dissipated energy per radian. Moreover, the photon loss rate can be divided into internal loss rate $\Gamma_R = f_0/(2Q_i)$ taking into account the photons dissipated inside the device, and external loss rate $\Gamma_0 = f_0/(2Q_e)$ referring to the photons leaving the resonator via the coupling capacitor. The total quality factor can be expressed in terms of these two contributions as

$$Q_{\text{tot}} = \left(\frac{1}{Q_i} + \frac{1}{Q_e}\right)^{-1}. \tag{2.2}$$

The starting point when deriving a fit function for the reflected response is to conclude that it is related to the impedance of the lumped element circuit, Z_r, and the probe line, $Z_0 \approx 50\,\Omega$ [11], as

$$S_{11} = \frac{Z_r - Z_0}{Z_r + Z_0}, \tag{2.3}$$

where the total impedance of the coupling capacitor and the RLC resonator in Fig. 2.1(b) is given as

$$Z_r = \frac{1}{i\omega C_c} + \left(\frac{1}{R_r} + \frac{1}{i\omega L_r} + i\omega C_r\right)^{-1}. \tag{2.4}$$

After some algebra and implementation of appropriate approximations, elaborated in Appendix B, the complex reflection coefficient takes the form

$$S_{11} = \frac{\delta f^2 + (\Gamma_R^2 - \Gamma_0^2) + i2\Gamma_0\delta f}{\delta f^2 + (\Gamma_R + \Gamma_0)^2}, \tag{2.5}$$

where $\delta f = f - f_0$ denotes the detuning away from resonance. From Eq. (2.5), the magnitude and phase of the reflection coefficient can be derived as

$$|S_{11}| = \sqrt{\mathrm{Re}\left[S_{11}\right]^2 + \mathrm{Im}\left[S_{11}\right]^2} = \frac{\sqrt{\left(\delta f^2 + (\Gamma_R^2 - \Gamma_0^2)\right)^2 + (2\Gamma_0\delta f)^2}}{\delta f^2 + (\Gamma_R + \Gamma_0)^2}, \tag{2.6}$$

$$\arg(S_{11}) = \arctan\left(\frac{\mathrm{Im}\left[S_{11}\right]}{\mathrm{Re}\left[S_{11}\right]}\right) = \arctan\left(\frac{2\Gamma_0\delta f}{\delta f^2 + (\Gamma_R + \Gamma_0)^2}\right). \tag{2.7}$$

From Eq. (2.2), we see that there are three possible coupling regimes between the internal and external quality factors. If $Q_i < Q_e$, the resonator is *undercoupled* and the photons tend to get dissipated inside the resonator prior to leaking out via the coupling capacitor, see Fig. 2.2(a). When the two quality factors are matched, $Q_i = Q_e$, the resonator is *critically coupled* and the magnitude response deviates from the otherwise Lorentzian line shape and drops down to zero exactly at resonance, see Fig. 2.2(b). The third, and usually most preferred regime is when $Q_i > Q_e$ and the resonator is *overcoupled*, see Fig. 2.2(c). In this case, most photons leave the system through the coupling capacitor and can thus get detected and measured.

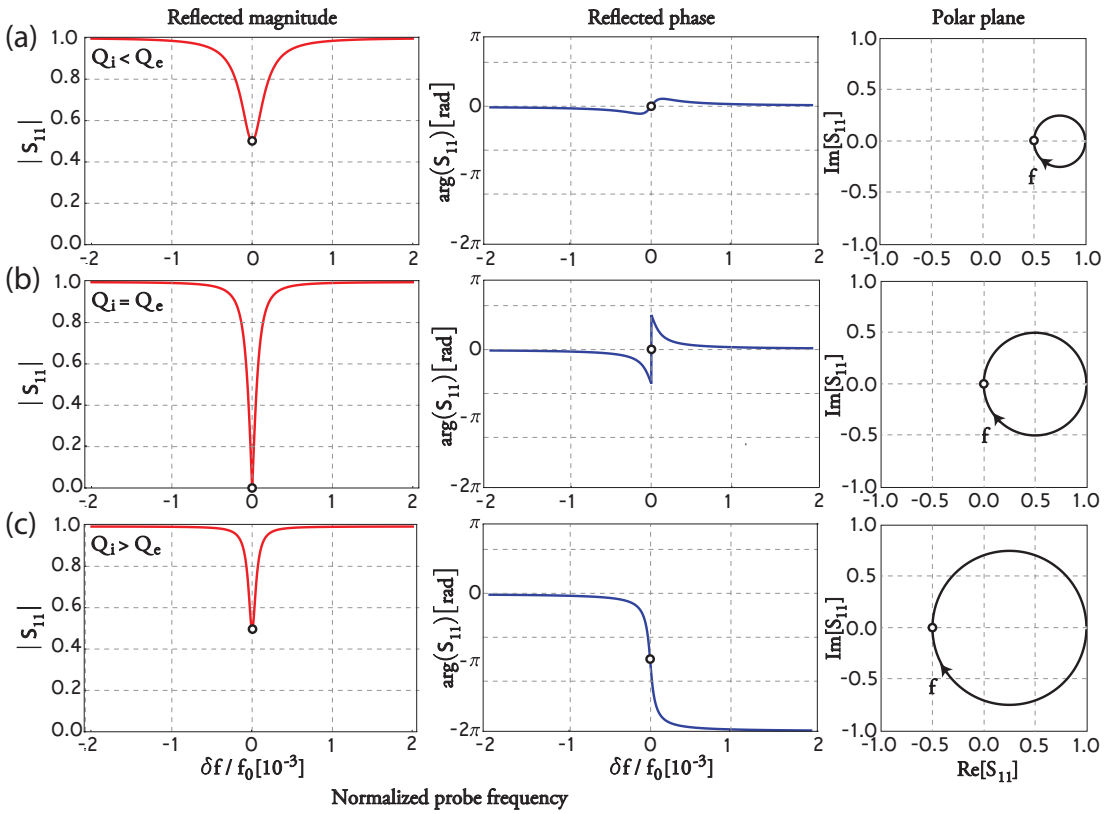

Figure 2.2: The reflected magnitude and phase responses of the quarter-wavelength resonator as a function of the normalized probe frequency in its three different coupling regimes: **(a)** undercoupled when $Q_e < Q_i$, **(b)** critically coupled when $Q_e = Q_i$, and **(c)** overcoupled when $Q_e > Q_i$. The plots on the right-hand side are the polar representation of the three coupling regimes. The small black circles indicate the point at which the probe is at resonance.

2.1.2 The frequency-tunable resonator

In this work, we use an extended and well-studied version of the CPW resonator, where its resonant frequency is made tunable [23–26]. In this section, we will see how this modification not only adds another degree of freedom to the system, but also vastly expands its number of applications.

In the previous section 2.1, the distributed superconducting resonator was modelled as a lumped element LC-oscillator (close to its resonant frequency). A resonator with tunable frequency can be realized if either its total inductance or capacitance is tunable. Here we choose to introduce a tunable inductance by shorting the resonator to ground via two Josephson junctions in parallel, forming a SQUID[1]. The Josephson inductance will then take part in the total inductance of the resonator, with a participation ratio, $\gamma_0 \approx 5 - 10\%$, tailorable in fabrication, see Fig. 2.3(a). Moreover, the tuning is accomplished by threading the loop of the SQUID with magnetic flux, see Fig. 2.3. This has the consequence of tuning the electrical length of the resonator, see Fig. 2.3(b). The modulated Josephson inductance thus gets mapped onto a modulated resonant frequency, well approximated as [23],

$$\omega_r(F) \approx \frac{\omega_{\lambda/4}}{1 + \gamma_0 / |\cos(F)|}, \tag{2.8}$$

where $F = \pi\Phi_{\mathrm{dc}}/\Phi_0$ is the applied dc-flux, and $\omega_{\lambda/4} = \omega_r|_{\gamma_0=0}$ denotes the bare resonant frequency, in the absence of the Josephson inductance. From Eq. (2.8), we see that the shape of the frequency tuning curve as a function of applied magnetic flux is governed by the participation ratio of the nonlinear Josephson inductance L_s in Eq. (1.10) to the geometrical resonator inductance, $\gamma_0 = L_s(F = 0)/Ll$, where L is the inductance per unit length of the resonator and l its length, see Fig. 2.4.

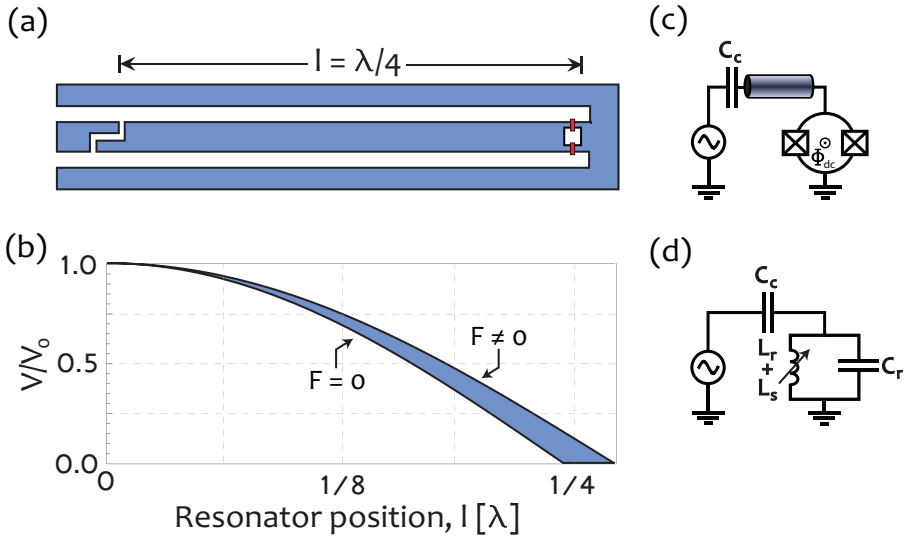

Figure 2.3: **(a)** CPW quarter-wavelength resonator, terminated to ground via a SQUID. **(b)** By changing the dc magnetic flux through the SQUID, the electrical length of the resonator is varied, yielding a modified fundamental frequency. **(c)** Circuit diagram of the SQUID, terminating the device. **(d)** Close to resonance, the system can be modelled by an LC-oscillator with nonlinear flux-tunable inductance.

[1]It turns out that both the effective inductance and capacitance tunes with applied magnetic flux [22].

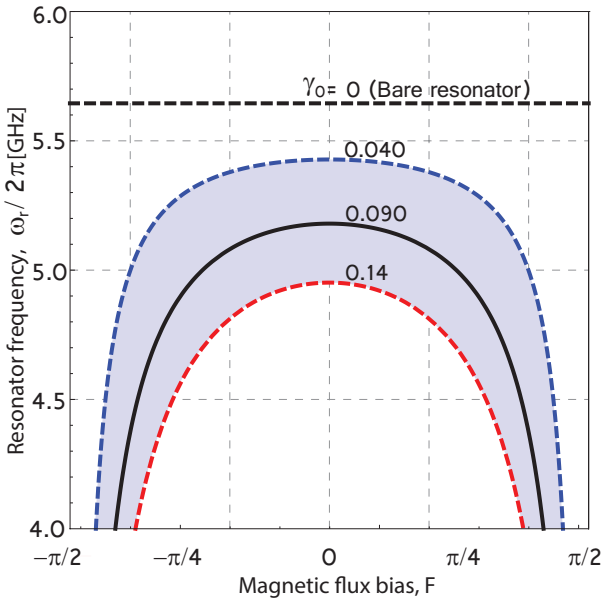

Figure 2.4: The shape of the frequency tuning curve is governed by the inductive participation ratio, γ_0. The black dashed line represents a non-tunable resonator ($\gamma_0 = 0$), with a bare resonator frequency, $\omega_{\lambda/4}/2\pi \approx 5.65\,\text{GHz}$, whereas the dashed blue, solid black, and dashed red show the tuning curve for $\gamma_0 = 4\,\%$, $9\,\%$, and $14\,\%$, respectively.

2.2 The flux-pumped parametric oscillator

The concept of parametric oscillations, first introduced by M. Faraday in 1831 [27], has been extensively studied and can be found in many systems ranging from varactor diodes in electrical circuits to swings in the playground. The word "parametric" means that one of the parameters found in the oscillators equations of motion, *e.g.* resonant frequency or damping, is modulated (or pumped) in time. The consequence of pumping the system parametrically is that oscillations build up under certain conditions, increasing the amplitude exponentially in time, until nonlinearities saturates the oscillations [28].

In contrast to the harmonic oscillator, parametric systems exhibit instabilities which open up possibilities to use these systems as sensitive probes. Although this is a very old field in physics, this phenomenon was first observed in superconducting circuits based on the nonlinear inductance of Josephson junctions by B. Yurke *et al.* in 1988 [29], from which our implementation originates.

In our case, the quarter wavelength tunable resonator can be operated as a parametric oscillator by applying an ac-flux with angular frequency $\omega_p \approx 2\omega_r$ to the device in addition to the static dc-flux, see Fig. 2.5 [24–26, 30]. The choice of quarter-wavelength resonator is then favorable, due to the absence of another resonant mode at the pumping frequency $2\omega_r$, preventing the pump from populating the resonator at the pump frequency. Before the resonator field starts to build up, however, the strength of the pump needs to compensate for the damping of the system, Γ. Throughout this thesis, we refer to this point as the *parametric instability threshold*, separating two operation regimes which will be discussed in the following sections.

2.2.1 Parametric amplification below the threshold

Before treating the parametric oscillations, some techniques and intuition can be obtained from first considering the simpler case of small pump amplitude, such that it does not surpass the parametric instability threshold. In this regime below the parametric threshold, we can operate the system as a *parametric amplifier*, in which small probe signals at the resonator frequency can be amplified [24, 25, 31–33].

In this section, we outline how the gain of the amplifier is calculated by formulating and solving the differential equation describing the dynamics of the system. Here, we consider the case of parametric pumping, in which the signal and the idler fall within the same resonator mode, $\omega_p \approx 2\omega_r$. For the special case of degenerate pumping when $\omega_p = 2\omega_s$, the signal and idler coincide and give rise to phase sensitive parameteric amplification where no additional noise is added to the signal. For the phase insensitive case, where $\omega_p \neq 2\omega_s$, at least half a quantum of noise is added to the amplified signal.

Formulation of the differential equation

The system can be treated using quantum network theory and circuit quantization [20, 34], by denoting the canonical flux of each node $\Phi_i = \int_{-\infty}^{t} V_i dt'$, with V_i being the node voltage with reference to ground, see Fig. 2.5. We then consider the scattering of the incoming field, $\Phi_{\text{in}}(x,t)$, where x is the position along the line (with the resonator located at $x = 0$) [19]. Since the dynamics experimentally is

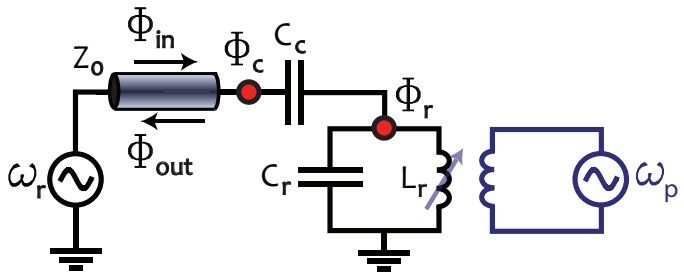

Figure 2.5: The circuit diagram for the flux-pumped parametric oscillator. The canonical flux nodes outside the coupling capacitor and inside the resonator are denoted Φ_{c} and Φ_{r}, respectively. The microwave pump (in blue) is inductively coupled to the SQUID of the resonator.

observed by probing the outgoing field $\Phi_{\mathrm{out}}(x,t)$, the aim is to relate this field with the incoming one. The solution takes the form of a one-dimensional wave equation due to the small dimensions of the coplanar waveguide center conductor and gaps

$$\Phi_{\mathrm{c}}(t) = \Phi_{\mathrm{in}}\left(\frac{x}{v_{\mathrm{ph}}} + t\right) + \Phi_{\mathrm{out}}\left(-\frac{x}{v_{\mathrm{ph}}} + t\right), \tag{2.9}$$

where the phase velocity $v_{\mathrm{ph}} = 1/\sqrt{LC}$ denotes the speed of light in the line. The boundary condition can be derived by taking the space and time derivatives of Eq. (2.9),

$$-\frac{1}{L}\frac{\partial \Phi_c}{\partial x}\bigg|_{x=0} = \frac{1}{Z_0}\left(\frac{\partial \Phi_c}{\partial t} - 2\frac{\partial \Phi_{\mathrm{in}}}{\partial t}\right)\bigg|_{x=0}. \tag{2.10}$$

Then, recalling that the current through an inductor and capacitor can be written $I_{\mathrm{L}} = \Delta\Phi/L$ and $I_{\mathrm{C}} = Cd^2(\Delta\Phi)/dt^2$, respectively, where $\Delta\Phi$ is the difference in flux across the element. For node c, Kirchoff's laws yields

$$C_c\left(\frac{d^2\Phi_c}{dt^2} - \frac{d^2\Phi_r}{dt^2}\right) = -\frac{1}{Z_0}\frac{d\Phi_c}{dt} + \frac{2}{Z_0}\frac{d\Phi_{\mathrm{in}}}{dt}, \tag{2.11}$$

whereas, considering node r yields

$$C_c\left(\frac{d^2\Phi_r}{dt^2} - \frac{d^2\Phi_c}{dt^2}\right) = -C_r\frac{d^2\Phi_r}{dt^2} - \frac{1}{L_r}\Phi_r. \tag{2.12}$$

Now, rearranging the terms and divide both sides with $C_c + C_r$ gives

$$\frac{d^2\Phi_r}{dt^2} + \frac{1}{L_r(C_c + C_\kappa)}\Phi_r = \frac{C_c}{C_c + C_r}\frac{d^2\Phi_c}{dt^2}. \tag{2.13}$$

Expressing the resonant frequency as $\omega_r = 1/\sqrt{L_r(C_c + C_r)}$, and the coupling parameter as $\kappa = C_c/(C_c + C_r)$, Eq. (2.13) can be written as

$$\frac{d^2\Phi_r}{dt^2} + \omega_r^2\Phi_r = \kappa\frac{d^2\Phi_c}{dt^2}. \tag{2.14}$$

We include the parametric pumping at angular frequency, ω_p, and strength, ϵ, to arrive at the final differential equation for the system below the threshold. Assuming that the coupling remains constant, the equation takes the form

$$\frac{d^2\Phi_r}{dt^2} + \left(\omega_r^2 + \epsilon\cos(\omega_p t + \phi)\right)\Phi_r = \kappa\frac{d^2\Phi_c}{dt^2}. \tag{2.15}$$

Solving the differential equation

Due to the non-linearity of Eq. (2.15), it cannot be solved using standard techniques from Fourier analysis. Instead, the principles of harmonic balance, also known as slow variables [35], can be used. Consider the following *ansatz* for the canonical flux, where we separate the two quadratures

$$\Phi_i = q_{i,1}\cos\left(\frac{\omega_p}{2}t\right) - q_{i,2}\sin\left(\frac{\omega_p}{2}t\right), \tag{2.16}$$

where $i \in \{c, r\}$ for the quadrature indices. Due to the complex nature of the output, the quadratures are better represented in the complex plane by reformulating the *ansatz* (2.16) as

$$\Phi_i = \frac{u_i}{2}\exp\left(i\frac{\omega_p}{2}t\right) + \frac{u_i^*}{2}\exp\left(-i\frac{\omega_p}{2}t\right), \tag{2.17}$$

where $u_i = q_{i,1} + iq_{i,2}$. Inserting the *ansatz* (2.17) into Eq. (2.15) gives two coupled differential equations

$$\begin{cases} -C_c\left(\frac{\omega_p}{2}\right)^2(u_c - u_r) = -\frac{i}{Z_0}\frac{\omega_p}{2}u_c + \frac{2}{Z_0}\frac{\omega_p}{2}u_{\text{in}}^0 \\ \left(\omega_r^2 - \left(\frac{\omega_p}{2}\right)^2\right)u_r + \frac{\epsilon}{2}u_r^*\exp(i\phi) = -\kappa\left(\frac{\omega_p}{2}\right)^2 u_c \end{cases}, \tag{2.18}$$

where u_{in}^0 denotes the complex quadrature at the input of the resonator. Now, let us recall the boundary condition in Eq. (2.10) and express it in terms of impedances

$$u_{\text{out}} = \frac{Z_0}{Z_L + Z_0}u_r + \frac{Z_L - Z_0}{Z_L + Z_0}u_{\text{in}}^0. \tag{2.19}$$

Approximate solution

To analytically solve this problem is hard. Therefore, we find an approximate solution by assuming that $Z_L \gg Z_0$ at resonance. We define

$$\kappa Q = \frac{|Z_L(\omega_r)|}{Z_0} = \frac{1}{Z_0 C_c \omega_r} \qquad Q = \frac{C_c + C_r}{Z_0 C_c^2 \omega_r}. \tag{2.20}$$

In the limit when $\kappa Q \gg 1$, we find the lowest order of the solution for the amplitude gain

$$g = \frac{q_{\text{out},1} + iq_{\text{out},2}}{\Phi_{\text{in}}^0} = 1 - 2\frac{1 + \epsilon''\sin(\Delta\theta) - i\left(\epsilon''\cos(\Delta\theta) - \delta'\right)}{1 + \delta'^2 - \epsilon''^2}, \tag{2.21}$$

where $\delta' = \left(\frac{\omega_p}{2} - \omega_r\right)/\Gamma = \delta/\Gamma$ and $\epsilon'' = \epsilon Q/(\omega_r\omega_p) = \epsilon/(2\Gamma\omega_p)$ are the normalized detuning and pump strength, respectively. In Fig. 2.6, the absolute value of the gain expression in Eq. (2.21) for the degenerate parametric amplifier ($\delta' = 0$) is plotted as

function of the phase angle between the signal and the pump for three different values of the normalized pump strength, ϵ''. The zero-gain level represents the amount of power needed to compensate for the depth of the reflected magnitude response of the resonator and is thus minimized when the resonator is highly overcoupled, recall Fig. 2.2.

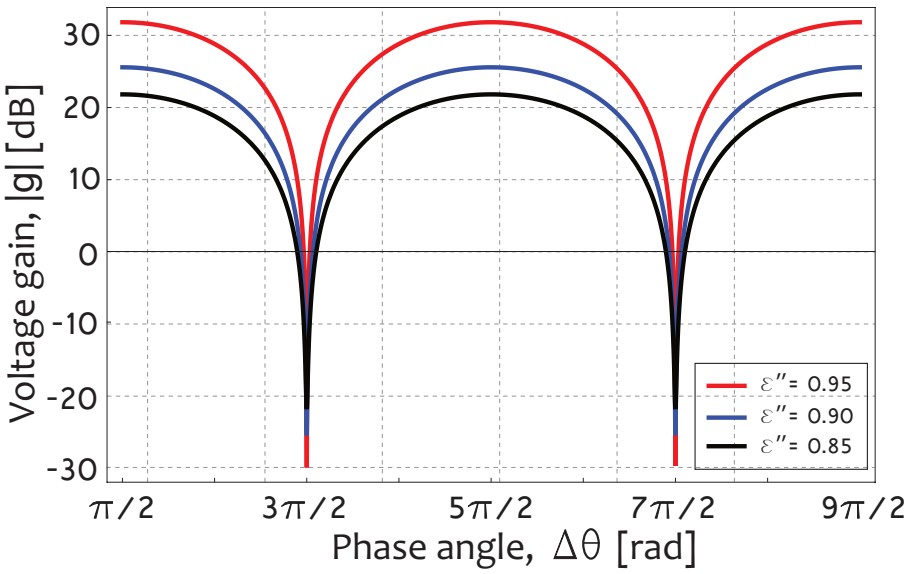

Figure 2.6: Voltage gain curves for the degenerate parametric amplifier as a function of the phase angle between the signal and the pump, $\Delta\theta$ for three different normalized pump strengths below the threshold. $\epsilon'' = 0.95$, 0.90, and 0.85 in red, blue, and green solid lines, respectively. The zero-gain line in black will depend on the magnitude dip of the resonator and can be interpreted as the output power with the parametric pump turned off.

2.2.2 Parametric oscillations above the threshold

The central phenomenon in this thesis takes place when the pump amplitude exceeds the damping ($\epsilon'' > 1$), where the system starts to build up a field inside the resonator, known as *parametric oscillations*. These occur only within a certain region in the space spanned by the pump-strength, ϵ'', and the pump-resonator detuning, $\delta' = (\omega_p/2 - \omega_r)/\Gamma$. In this section, the conditions needed to build up parametric oscillations are described.

To capture the dynamics of this regime, we need to add the lowest order (cubic) nonlinearity to the equations of motion, taking the form of a Duffing oscillator as described by Dykman [36]

$$\frac{\partial^2\varphi}{\partial t^2} + 2\Gamma\frac{\partial\varphi}{\partial t} + \left[\omega_r^2 + \epsilon\cos(\omega_p t)\right]\varphi - \alpha\varphi^3 = \xi(t), \tag{2.22}$$

where $\varphi = 2\pi\Phi_r/\Phi_0$, ϵ is the amplitude of the frequency modulation, $2\Gamma = \omega_r/Q$ is the resonance line width corresponding to the damping of the system, and $\alpha \propto (L_s/L_r)^3$ is the so-called Duffing term describing the dominant nonlinearity of the system. In our system, this term is negative having the mechanical analogue of a softening spring. Finally, $\xi(t)$ on the right hand side of Eq. (2.22) represents the mean-zero noise that induces activated switching between two meta-stable states of the system, further described later in this section.

Solution to the differential equation

Similar to the case of solving the equation of motion below the threshold, we need to make certain approximations to find analytical solutions to Eq. (2.22). Again, to solve this class of weakly nonlinear oscillators, we deploy the technique of slow variables [35] where the in-phase and quadrature amplitudes are allowed to vary slowly in time by introducing a slow-time scale, τ, yielding

$$\tau = \Gamma t, \qquad \frac{d}{dt} = \Gamma\frac{d}{d\tau}. \tag{2.23}$$

The method is then to let the "constants" of the *ansatz* be functions of this slow time scale

$$\begin{aligned}\varphi &= q_1(\tau)\cos\left(\frac{\omega_p}{2}t\right) - q_2(\tau)\sin\left(\frac{\omega_p}{2}t\right) = \\ &= \frac{u(\tau)}{2}\exp\left(i\frac{\omega_p}{2}t\right) + \frac{u^*(\tau)}{2}\exp\left(-i\frac{\omega_p}{2}t\right).\end{aligned} \tag{2.24}$$

Now, by assuming small damping ($\Gamma \ll \omega_p\epsilon''$) and neglecting second derivatives due to the slow variables, the first and second derivatives of Eq. (2.24) can be approximated as

$$\frac{d\varphi}{dt} \approx i\frac{\omega_p}{4}\left(u(\tau)\exp\left(i\frac{\omega_p}{2}t\right) - c.c.\right), \tag{2.25}$$

$$\frac{d^2\varphi}{dt^2} \approx -\left(\frac{\omega_p}{2}\right)^2 + i\Gamma\frac{\omega_p}{2}\left(\frac{du}{d\tau}\exp\left(i\frac{\omega_p}{2}t\right) - c.c.\right). \tag{2.26}$$

Moreover, the pump- and cubic nonlinearity terms are approximated by neglecting fast rotating terms

$$\varphi \cos(\omega_p t) \approx \frac{1}{4}\left(u(\tau)\exp\left(-i\frac{\omega_p}{2}t\right) + c.c.\right), \tag{2.27}$$

$$\varphi^3 \approx \frac{3}{8}\left(u|u|^2\exp\left(i\frac{\omega_p}{2}t\right) + c.c.\right). \tag{2.28}$$

Inserting the *ansatz* along with the approximated terms (2.27) and (2.28) into the Duffing equation (2.22), we can express the equations of motion for the system as two coupled differential equations for the in-phase, q_1, and quadrature, q_2, signals

$$\begin{cases} \frac{dq_1}{d\tau} = -q_1 + (\epsilon'' + \delta')q_2 + \alpha'(q_1^2+q_2^2)q_2 \equiv -q_1 + \frac{\partial g}{\partial q_2} \\ \frac{dq_2}{d\tau} = -q_2 + (\epsilon'' - \delta')q_1 - \alpha'(q_1^2+q_2^2)q_1 \equiv -q_2 + \frac{\partial g}{\partial q_1} \end{cases}, \tag{2.29}$$

where $\delta' = (\omega_p/2 - \omega_r)/\Gamma = \delta/\Gamma$ is the normalized angular frequency detuning between the pump and the resonator, $\epsilon'' = \epsilon/(2\Gamma\omega_p)$ is the normalized pump amplitude, and $\alpha' = 3\alpha/(4\Gamma\omega_p)$ is the normalized Duffing nonlinearity parameter. The function $g = g(q_1, q_2)$ on the right hand side of the two equations in (2.29) is the Hamiltonian of the system describing the meta-potential landscape of the system. This function will be the topic of the next section.

The meta-potential

An intuitive picture for the slow dynamics of the two coupled equations of motion (2.29) can be gained by studying the meta-potential in the frame rotating at the resonator frequency,

$$g(q_1, q_2) = \frac{\delta'}{2}(q_1^2+q_2^2) + \frac{\epsilon''}{2}(q_2^2-q_1^2) + \frac{\alpha'}{4}(q_1^2+q_2^2)^2, \tag{2.30}$$

where the dynamics mimics that of a fictitious particle moving in this meta-potential with two meta-stable states [37]. When no probe signal is sent to the resonator, the two states oscillate with the same amplitude, but are separated in phase by π-radians, see Fig. 2.7. From Eq. (2.30), we see that its shape is governed by the three normalized parameters δ', ϵ'', and α', see Fig. 2.7.

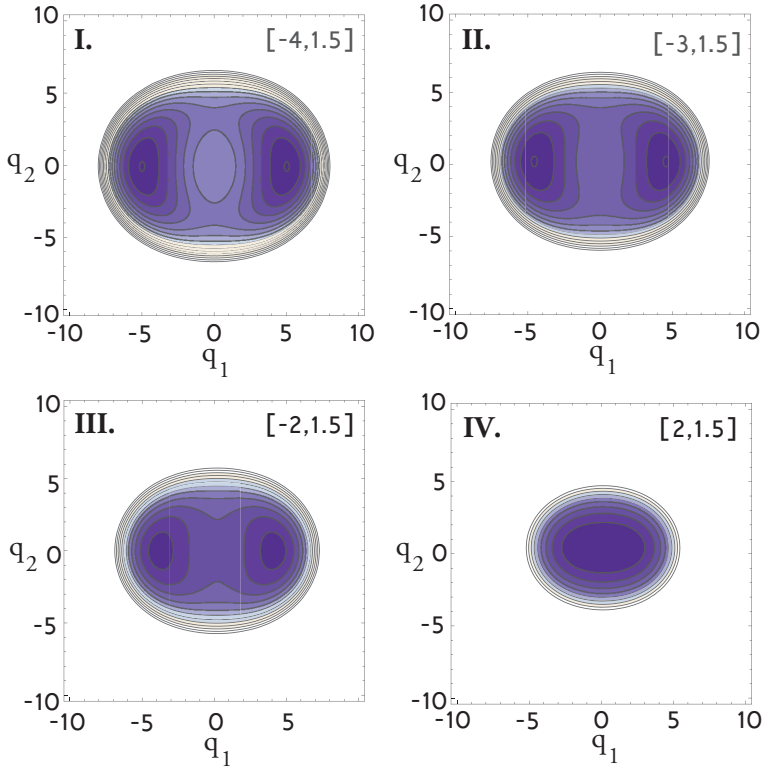

Figure 2.7: Contour plot of the in-phase (q_1) and quadrature (q_2) components of the metapotential in Eq. (2.30) for four different operation points in the plane spanned by the normalized pump-resonator detuning δ' and pump strength ϵ''. The operation points are marked in the upper right corner of each panel and in the plane later in Fig. 2.8.

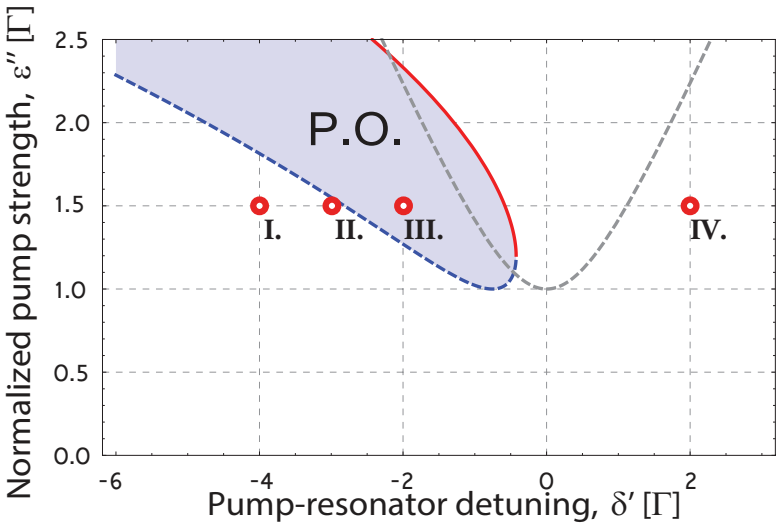

Figure 2.8: Region in which parametric oscillations build up in the resonator in the parameter plane spanned by the effective pump strength and pump-resonator detuning, both normalized to the resonator line width, Γ. The dashed blue line and the solid red line are the solutions to Eq. (2.43) when higher order terms of the pump mixing product give rise to a pump-induced frequency shift. The dashed gray line is the solution to Eq. (2.35), in absence of higher order pump terms. The four marked points **I-IV** correspond to the four panels in Fig. 2.7, where the shape of the metapotential is calculated from Eq. (2.30).

2.2.3 Region of parametric oscillations

In the previous section, we saw that parametric oscillations only occur when the pump amplitude is above the threshold ($\epsilon'' > 1$), recall Figs 2.7 and 2.8. In addition, the pump frequency needs to be close to degeneracy ($\omega_p \approx 2\omega_r$). In this section we will systematically derive the stability conditions for the parametric oscillations to map out the *parametric instability region* in the plane spanned by δ' and ϵ''.

Steady state solutions

The stability conditions (or bifurcation points) of the system can be derived from the equations of motion (2.29), by finding their steady state response

$$\begin{cases} 0 = q_1 - (\epsilon'' + \delta' + \alpha' (q_1^2 + q_2^2)) q_2 \\ 0 = q_2 - (\epsilon'' - \delta' - \alpha' (q_1^2 + q_2^2)) q_1 \end{cases} . \tag{2.31}$$

The slow variables, q_1 and q_2 are first converted to magnitude, q, and phase, θ, for the oscillations using the following substitution

$$\left[q_1 = \sqrt{\alpha'} q \cos(\theta), \;\; q_2 = \sqrt{\alpha'} q \sin(\theta) \right], \tag{2.32}$$

The trivial solution $q = 0$ is omitted by dividing both equations in (2.31) with $\sqrt{\alpha'} q$

$$\begin{cases} 0 = \cos(\theta) - (\epsilon'' + \delta' + \alpha' q^2) \sin(\theta) \\ 0 = \sin(\theta) - (\epsilon'' - \delta' - \alpha' q^2) \cos(\theta) \end{cases} . \tag{2.33}$$

If we solve for zero amplitude $q = 0$, we find the following solutions

$$q = \sqrt{\pm \frac{1}{\alpha'} \left(\sqrt{\epsilon''^2 - 1} - \delta' \right)}. \tag{2.34}$$

By instead putting the amplitude to zero and solving for the normalized drive strength ϵ'', the symmetric bifurcation curve in Fig. 2.8 is obtained

$$\epsilon'' = \sqrt{\delta'^2 + 1} \tag{2.35}$$

Higher order terms

The region in Eq. (2.35) yields a completely symmetric region which, however, does not agree well with experiments due to the fact that our frequency modulation is affected by the cosine nonlinearity of Eq. (2.8), see Fig. 2.4. Therefore, we need to extend the model to take into account also higher order terms of the mixing product of the pumped flux in the SQUID, see Appended paper I. This *pump-induced nonlinearity* manifests itself as a frequency shift of the region increasing with pump amplitude, which we quantify by introducing a dimensionless parameter β, defined as

$$\frac{\omega_r(\epsilon) - \omega_r(0)}{\Gamma} = -\beta \epsilon''^2, \tag{2.36}$$

which gives an extended Duffing equation

$$\frac{\partial^2\varphi}{\partial t^2} + 2\Gamma\frac{\partial\varphi}{\partial t} + \left[\omega_r^2 + \epsilon\cos(\omega_p t) - \frac{\beta\epsilon^2}{4\Gamma\omega_p}(1-\cos(2\omega_p t))\right]\varphi \\ -\alpha\left[1 - \frac{3\lambda}{4\Gamma\omega_p}\epsilon\cos(\omega_p t)\right]\varphi^3 = 0, \tag{2.37}$$

where we also have introduced λ for representing the correction to the Duffing nonlinearity due to the fact that α is modulated by the pump. Again implementing the method of slow variables, we can write down the two coupled differential equations for the equations of motion

$$\begin{cases} \frac{dq_1}{d\tau} + q_1 - (\delta' + \epsilon'' + \beta\epsilon''^2 + \alpha'(q_1^2 + (1+\lambda\epsilon'')q_2^2))q_2 = 0 \\ \frac{dq_2}{d\tau} + q_2 + (\delta' - \epsilon'' + \beta\epsilon''^2 + \alpha'(q_2^2 + (1-\lambda\epsilon'')q_1^2))q_1 = 0 \end{cases} \tag{2.38}$$

After a while, the system reaches steady state and we can reduce these equations to

$$\begin{cases} q_1 - (\delta' + \epsilon'' + \beta\epsilon''^2 + \alpha'(q_1^2 + (1+\lambda\epsilon'')q_2^2))q_2 = 0 \\ q_2 + (\delta' - \epsilon'' + \beta\epsilon''^2 + \alpha'(q_2^2 + (1-\lambda\epsilon'')q_1^2))q_1 = 0 \end{cases} \tag{2.39}$$

Next, let us make the same variable substitution as in Eq. (2.32), and omitting the trivial solution and dropping the next order term of the Duffing nonlinearity ($\lambda = 0$)[2], yielding

$$\begin{cases} -(\alpha' q^2 + \epsilon'' + \beta\epsilon''^2 + \delta')\sin(\theta) + \cos(\theta) = 0 \\ (\alpha' q^2 - \epsilon'' + \beta\epsilon''^2 + \delta')\cos(\theta) + \sin(\theta) = 0 \end{cases}, \tag{2.40}$$

which can be written as

$$\begin{cases} \cot(\theta) - \alpha' q^2 - \epsilon'' - \beta\epsilon''^2 - \delta' = 0 \\ \tan(\theta) + \alpha' q^2 - \epsilon'' + \beta\epsilon''^2 + \delta' = 0 \end{cases}. \tag{2.41}$$

From these two equations we can derive the amplitudes and phases corresponding to the stable and unstable solutions

$$q = \sqrt{\pm\frac{1}{\alpha'}\left(\sqrt{\epsilon''^2 - 1} - \beta\epsilon''^2 - \delta'\right)}. \tag{2.42}$$

Similar to the previous case in Eq. (2.35), the amplitude is put to zero and we solve Eq. (2.42) for the normalized drive strength ϵ''. This gives the bifurcation points in Fig. 2.8 defining the parametric region, see Appended paper I,

$$\epsilon'' = \frac{\sqrt{1 - 2\beta\delta' \pm \sqrt{1 - 4\beta(\beta + \delta')}}}{\sqrt{2}\beta}. \tag{2.43}$$

The phase of the parametric oscillations can also be calculated from Eq. (2.41) by instead eliminating the amplitudes, yielding

$$\theta = \arctan\left(\epsilon'' \pm \sqrt{\epsilon''^2 - 1}\right) + n\pi, \qquad n \in \{0, 1\}, \tag{2.44}$$

where $n = 0, 1$ give the two π-shifted states in Fig. 2.7.

[2]We justify this approximation with the argument that the Duffing nonlinearity is not dominant over the pump-induced frequency shift.

2.2.4 Resonator field amplitude formalism

In the previous sections 2.2.1 and 2.2.2, the differential equations representing the equations of motion of the system were derived using quantum network formalism by introducing canonical flux in the resonator. An alternative method, which can be more intuitive when considering a smaller photon number, is to consider the field amplitude, A, inside the resonator, as well as an incoming, B, and outgoing, C, flow of photons [21], see Fig. 2.9. This is the method utilized throughout Appended papers I and II, and will here get introduced.

Close to resonance, $\delta \equiv \omega_p/2 - \omega_r \ll \omega_r$, the field amplitude inside the resonator can be treated as a slow variable compared to all other timescales in the system, yielding a simplified Langevin equation for the system dynamics [21],

$$i\dot{A} + \delta A + \epsilon A^* + \alpha |A|^2 A + i\Gamma A = \sqrt{2\Gamma_0} B(t). \tag{2.45}$$

Here, A is the intra-resonator field amplitude, normalized such that $|A|^2$ is the number of photons in the resonator, whereas $B(t)$ is the probe field amplitude such that $|B|^2$ has units of photons per second. $\Gamma = \Gamma_0 + \Gamma_R$ is the total damping rate of the system, being the sum of the external, Γ_0, and internal, Γ_R, damping rates. ϵ and α denote the effective pump strength and Duffing parameter, respectively. The full dc-flux dependence of these coefficients can be expressed in terms of resonator parameters as

$$\epsilon \approx \frac{\delta f \omega_{\lambda/4} \gamma_0}{2} \frac{\sin(F)}{\cos^2(F)}, \tag{2.46}$$

$$\alpha \approx \frac{\pi^2 \omega_{\lambda/4} Z_0}{R_K} \left(\frac{\gamma_0}{\cos(F)} \right)^3 = \alpha_0 \left(\frac{\gamma_0}{\cos(F)} \right)^3, \tag{2.47}$$

where $\delta f = \pi \Phi_{ac}/\Phi_0$ is the normalized ac-flux amplitude, $Z_0 = 50\ \Omega$ is the characteristic impedance of the transmission line, $R_K = h/e^2$ is the quantum resistance, and $\alpha_0 = \pi^2 \omega_{\lambda/4} Z_0 / R_K$.

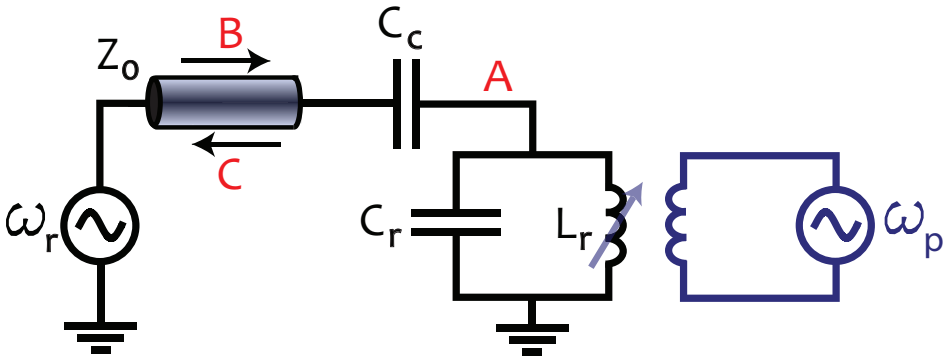

Figure 2.9: In the field amplitude formalism used by Wustmann and Shumeiko [21], the number of photons in the resonator is denoted A, whereas the incoming and outgoing flow are denoted B and C, respectively.

Transient response of the system

In the previous sections as well as in Appended paper I, we studied the steady state response of the JPO. However, in the JPO readout scheme presented in Appended paper II, the transient time response of the device is of equal importance as the steady state saturation level of the intra-resonator field. The ring-up time for the resonator is the dominant time scale for the readout time. We can get a feeling for the ring-up time as well as the steady state level of the resonator by numerically solving the Duffing Eq. (2.45), now letting both the amplitude A and the phase θ evolve over time.

Consider the case for no input field, $B(t) = 0$ and make the *ansatz*: $A = |A|e^{i\theta}$, we get the following

$$i\partial_t \left[Ae^{i\theta}\right] + \delta Ae^{i\theta} + \epsilon Ae^{-i\theta} + \alpha A^3 e^{i\theta} + i\Gamma Ae^{i\theta} = 0. \tag{2.48}$$

Dividing all terms with $e^{i\theta}$ and substituting the time derivative, $\partial_t[Ae^{i\theta}] = e^{i\theta}\partial_t A + Aie^{i\theta}\partial_t\theta$, yields

$$i\partial_t A - A\partial_t\theta + \delta A + \epsilon Ae^{-i2\theta} + \alpha A^3 + i\Gamma A = 0. \tag{2.49}$$

After dividing with A, we arrive at the following equation and its complex conjugate

$$\begin{cases} \frac{i\partial_t A}{A} - \partial_t\theta + \delta + \epsilon e^{-i2\theta} + \alpha A^2 + i\Gamma = 0 \\ -\frac{i\partial_t A}{A} - \partial_t\theta + \delta + \epsilon e^{i2\theta} + \alpha A^2 - i\Gamma = 0 \end{cases}, \tag{2.50}$$

which can be simplified to the following two relations

$$\begin{cases} \delta + \alpha A^2 + \epsilon\cos(2\theta - \partial_t\theta) = 0 \\ A(\Gamma - \epsilon\sin(2\theta)) + \partial_t A = 0 \end{cases}. \tag{2.51}$$

The numerical solution to the two coupled Eqs. (2.51) are plotted in Fig. 2.10. The dashed lines in Fig. 2.10 shows the same solutions, but with an applied low-pass filter with a cut-off frequency corresponding to a 50 ns sampling time.

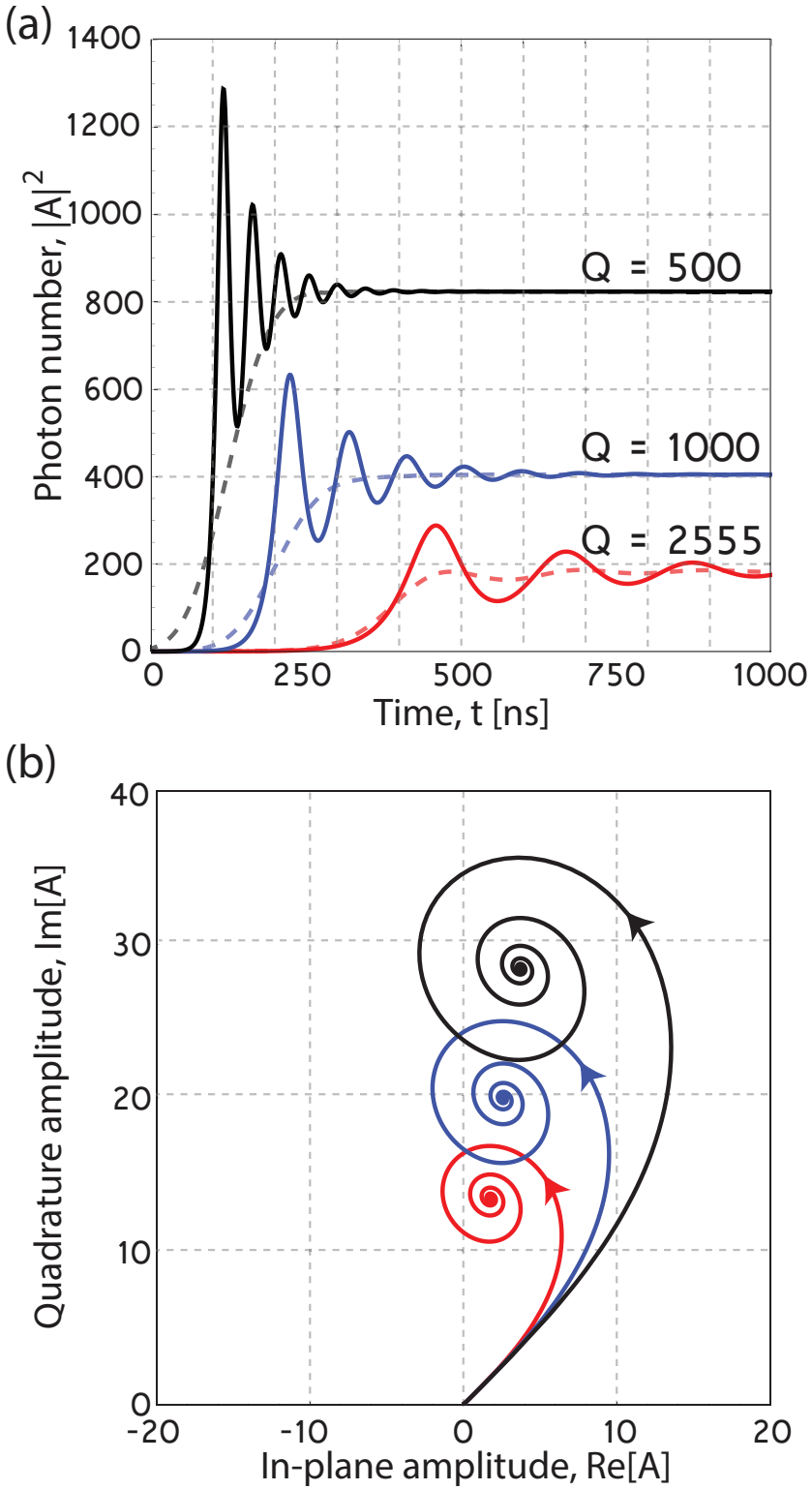

Figure 2.10: **(a)** Time response for the JPO for three different external quality factors, all with the same parameters as for the device presented in Appended paper II. **(b)** Polar representation of the transient field amplitude response plotted in (a). The arrows represent the direction of time, such that the center of the spirals correspond to steady state.

2.3 The "Pumpistor" model

An alternative and more applied way to think about the parametric phenomena in the flux-pumped parametric resonator was developed by K. M. Sundqvist *et al.*, see Appended paper III. In this model, the SQUID is described as the previously introduced Josephson inductance, see section 1.2.2, in parallel with another element which arises due to the flux pumping. This impedance was named the "pumpistor" and it depends on the phase angle between the probe signal and the pump. In particular, this classical treatment explains the phase response of the degenerate parametric amplifier and can be used as a practical tool when analyzing more complicated parametrically driven circuits, where our previously introduced formalisms get fairly complicated. In this section, we give a brief introduction to the theoretical framework of the model. For a more elaborate description, the reader is referred to the Appended paper III, as well as [38].

2.3.1 Expansion of the mixing product

The fundamental concept behind the pumpistor model is the frequency mixing product of the current flowing through the Josephson junctions, *i.e.* the flux pumped critical current of the SQUID (flux term) and the phase across the two parallel Josephson junctions (phase term), recall Eq. (1.7)

$$I = \underbrace{I_c \left|\cos\left(\pi\Phi_{\mathrm{p}}(t)/\Phi_0\right)\right|}_{\text{"flux"}} \times \underbrace{\sin(\varphi(t))}_{\text{"phase"}}, \tag{2.52}$$

where the flux of the pump can be written in terms of the dc-flux bias and a small ac-contribution from the pump at angular frequency ω_p with phase θ_p,

$$\Phi_{\mathrm{p}}(t) = \Phi_{\mathrm{dc}} + \Phi_{\mathrm{ac}}\cos(\omega_p t + \theta_p). \tag{2.53}$$

The two terms of Eq. (2.52) are then series expanded separately before they are multiplied together to find an approximation of the circuit impedance. By substituting Eq. (2.53) into the flux term of Eq. (2.52), we series expand around the dc-flux point, Φ_{dc}, yielding

$$I_c\cos\left(\pi\Phi_{\mathrm{p}}(t)/\Phi_0\right) \approx I_c\cos(F) - I_c\sin(F)\delta f\cos(\omega_p t + \theta_p), \tag{2.54}$$

with $F = \pi\Phi_{\mathrm{dc}}/\Phi_0$ and $\delta f = \pi\Phi_{\mathrm{ac}}/\Phi_0$ denoting the normalized dc and ac flux quantities, respectively. Moreover, assuming that the Josephson phase takes the form $\varphi(t) = \varphi_s\cos(\omega_s t + \theta_s)$, this term is expanded using a Fourier-Bessel series

$$\sin(\varphi(t)) = \sum_{n=-\infty}^{\infty} J_n(\varphi_s)\sin\left[n\left(\omega_s t + \theta_s + \frac{\pi}{2}\right)\right], \tag{2.55}$$

where J_n is the n$^{\mathrm{th}}$-order Bessel function of the first kind. The product is calculated, retaining only terms at the signal frequency and neglecting other mixing products. We then define an electrical input impedance at the signal frequency as

$$Z_{\mathrm{SQ}} = i\omega_s L_{\mathrm{SQ}}, \tag{2.56}$$

where the SQUID inductance can be expressed as the Josephson inductance in parallel with the pumpistor inductance[3] $L_{\mathrm{SQ}}^{-1} = L_{\mathrm{J}}^{-1} + L_{\mathrm{P}}^{-1}$, given as

$$L_{\mathrm{J}} = \frac{L_{\mathrm{J0}}}{\cos(F)} \left[\frac{\varphi_s}{2J_1(\varphi_s)} \right] \underset{\varphi_s \ll 1}{\approx} \frac{L_{\mathrm{J0}}}{\cos(F)}, \tag{2.57}$$

$$L_{\mathrm{P}} = \frac{-2\mathrm{e}^{i\Delta\theta}}{\delta f} \frac{L_{\mathrm{J0}}}{\sin(F)} \left[\frac{\varphi_s}{2J_1(\varphi_s) - 2\mathrm{e}^{i2\Delta\theta} J_3(\varphi_s)} \right] \underset{\varphi_s \ll 1}{\approx} \frac{-2\mathrm{e}^{i\Delta\theta}}{\delta f} \frac{L_{\mathrm{J0}}}{\sin(F)}, \tag{2.58}$$

with $L_{\mathrm{J0}} = \hbar/(2eI_c)$ and $\Delta\theta = 2\theta_s - \theta_p$. Thus, the SQUID can be represented as the equivalent circuit in Fig. 2.11(a), with the Josephson inductance in parallel with the pumpistor as an alternative formalism to the nonlinear differential equations presented in section 2.2. Next, we will investigate the phase dependence of the pumpistor and how to interpret it in terms of gain of a parametric amplifier.

2.3.2 Phase angle and negative resistance

An important property of the inductance of the pumpistor in Eq. (2.58) is that it is dependent on the phase angle $\Delta\theta$ between the signal and pump, which makes it responsible for the phase sensitivity of the degenerate parametric amplifier when $\omega_p = 2\omega_r$. When studying the behavior of the pumpistor, we note that the phase angle puts the device in four different regimes, illustrated in Fig. 2.11(b). When $\Delta\theta = 0$ or π, the pumpistor acts as a negative or positive inductance contribution to the Josephson inductance. However, at $\Delta\theta = \pi/2$, it acts as a resistor which leads to additional attenuation or de-amplification in the device. Finally, when the pumpistor reaches $\Delta\theta = -\pi/2$, it acts like a negative resistor, which provides gain by injecting power from the pump.

Another way to formulate the negative resistance is in terms of a negative internal quality factor, $Q_i < 0$. For the implementation of a degenerate parametric amplifier, this imposes some guidelines of operation regime for the amplifier. Maximum squeezing (and thus amplification), occurs when the system is close to (but below) its parametric instability threshold. In terms of quality factors, this gives the condition that $(-Q_e < Q_i < 0)$. Using the linearized impedance of the SQUID, also the gain of the amplifier can be calculated and related to the phase angle [22].

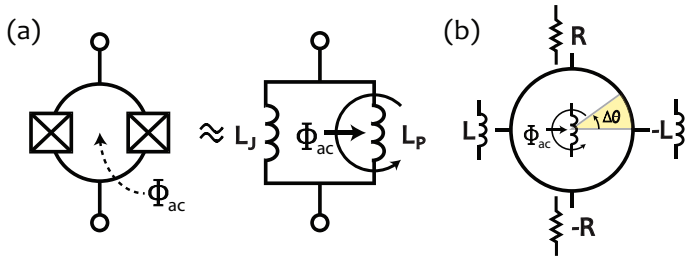

Figure 2.11: (a) The equivalent circuit of the SQUID as a Josephson inductance in parallel with the pumpistor. **(b)** The impedance of the pumpistor is governed by the phase angle $\Delta\theta = 2\theta_s - \theta_p$. When $\Delta\theta = -\pi/2$, it acts like a negative resistor where the pump injects power into the resonator, providing gain.

[3]The pumpistor is denoted as an inductor because its impedance is proportional to $i\omega_s$.

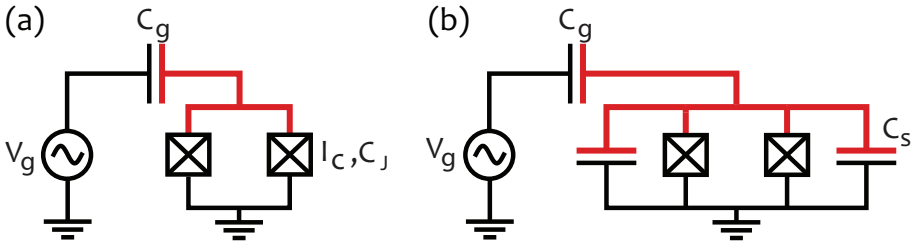

Figure 2.12: **(a)** The circuit diagram of the Cooper Pair Box. The island (in red) is biased with a gate voltage V_g through a gate capacitance C_g and separated from the reservoir by two parallel Josephson junctions of total of critical current, I_c, and junction capacitance, C_J. **(b)** The corresponding circuit diagram for the transmon qubit, in which two shunt capacitors, C_s have been introduced to reduce the charging energy, E_{C}.

2.4 The transmon superconducting qubit

In this section, we introduce the fundamental properties of the transmon superconducting qubit, which throughout the next section is coupled to the Josephson parametric oscillator, demonstrating a new single-shot readout scheme. For further details on the transmon qubit, the reader is referred to the orignal work developed by J. Koch *et al.* [39].

2.4.1 The Cooper-pair box

There are several flavors of superconducting qubits, including charge, phase, and flux qubits (and combinations thereof). These names refer to the respective quantum mechanical degree of freedom utilized to control the states of the qubit at hand. One of the most commonly used is the transmon qubit [39], derived from the Cooper-pair box (CPB) charge qubit [40–43]. To understand the physics of the transmon, it is therefore pedagogic to start out from the CPB.

The CPB consists of a small aluminum island, connected to a superconducting reservoir through a Josephson junction on one side and biased by a gate capacitance C_g and a gate voltage V_g on the other side, see Fig. 2.12(a). When the junction is in its superconducting state, Cooper pairs can tunnel in to and from the island. The potential of the island can then be controlled through the gate voltage.

The system is characterized by two energies; first, the *Josephson energy*, E_J is the coupling energy resulting from coherent Cooper-pair tunneling across the junctions,

$$E_J = \frac{\Phi_0 I_c}{2\pi} = \frac{R_Q \Delta}{2R_n e}, \tag{2.59}$$

where $R_{\mathrm{Q}} = \frac{h}{4e^2}$ and R_n are the quantum and normal state resistances, respectively. 2Δ is the superconducting energy gap related to the critical temperature of the material[4]. The second characteristic energy of the system is the *charging energy*, *i.e.* the (generalized) kinetic energy needed to transfer one electron across the capacitor,

[4]The critical temperature for bulk aluminum is $T_{\mathrm{c}} = 1.176\,\mathrm{K}$ [44]. However, for a thin film the critical temperature is slightly higher than for bulk material $\mathrm{T}_c \approx 1.4\mathrm{K}$. According to BCS theory [45], the superconducting gap is given as, $\Delta = 1.76 k_{\mathrm{B}} T_{\mathrm{c}}$, with k_{B} denoting the Boltzmanns constant.

$$E_{\mathrm{C}} = \frac{e^2}{2C_\Sigma}, \tag{2.60}$$

where $C_\Sigma = C_{\mathrm{g}} + C_{\mathrm{J}}$ represents the total capacitance between the island and its circuit environment. In addition, the CPB is characterized by the reduced gate charge, $n_g = C_g V_g / 2e$, governed by the applied gate voltage.

In most practical implementations of qubits, it is convenient to be able to tune its transition frequency. This is obtained in the same way as for the tunable resonator in Sec. 2.1.2, by adding another Josephson junction is in parallel with the first one, forming a dc-SQUID with flux-tunable Josephson energy, $E_{\mathrm{J}} \rightarrow E_{\mathrm{J}}(\Phi_{\mathrm{dc}})$. The effective Josephson energy is then given as

$$E_{\mathrm{J}}(\Phi_{\mathrm{dc}}) = E_{\mathrm{J}}^{\max} \left|\cos\left(\pi \Phi_{\mathrm{dc}} / \Phi_0\right)\right|, \tag{2.61}$$

where $\Phi_0 = h/2e$ is the flux quantum. For further information about the SQUID the reader is referred to section 1.2 and textbooks such as [8]. The Hamiltonian of the CPB can now be written in terms of these two energies in the charge basis,

$$\hat{H}_{\mathrm{CPB}} = 4E_{\mathrm{C}} \sum_{n=-\infty}^{\infty} (n - n_g)^2 |n\rangle\langle n| - \frac{E_{\mathrm{J}}}{2} \sum_{n=-\infty}^{\infty} \left[|n+1\rangle\langle n| + |n\rangle\langle n+1|\right]. \tag{2.62}$$

By doing the transformation $n \rightarrow -i\frac{d}{d\phi}$ the Hamiltonian in Eq. (2.62) takes the form of a quantum rotor in phase space

$$\hat{H}_{\mathrm{CPB}} = 4E_{\mathrm{C}} \left(-i\frac{d}{d\phi} - n_g\right)^2 - E_{\mathrm{J}} \cos\phi. \tag{2.63}$$

The exact solutions to the Hamiltonian in Eq. (2.63) are obtained using Mathieu functions [39], plotted for the three lowest energy levels in Fig. 2.13. In order to operate the system as a qubit, it is essential that it can be considered a two-level system, *i.e.* the two lowest eigenenergies must be well-separated from any higher energy levels of the system. In Fig. 2.13(a) the charge dispersion relations for the three lowest eigenenergies are plotted as a function of the reduced gate charge n_g and $E_{\mathrm{J}}/E_{\mathrm{C}}$. The bands form a periodic structure where the energy required for transitions between the ground state $|0\rangle$ and the first excited state $|1\rangle$ is smallest when the gate charge $n_g = m + \frac{1}{2}$, for integer numbers of m.

The CPB is thus mainly characterized by the energy ratio $E_{\mathrm{J}}/E_{\mathrm{C}}$. The two limiting regimes where $E_{\mathrm{J}}/E_{\mathrm{C}} \ll 1$ and $E_{\mathrm{J}}/E_{\mathrm{C}} \gg 1$ are referred to the *charge-* and *transmon* limits, respectively, shown in Fig. 2.13 (b) and (c). However, even though the goal of obtaining an effective two-level system is fulfilled, the CPB suffers from one major drawback in its sensitivity to small changes of the gate charge. Due to the environment, the qubit will be subject to fluctuations of the gate charge, known as charge noise. This means that the level spacing between the two levels will fluctuate, which causes short quantum coherence times. In 2002, D. Vion *et al.* [43] demonstrated that these half-integer values of the reduced gate charge (referred to as *sweet spots*) serve as optimal working points for operating the qubit.

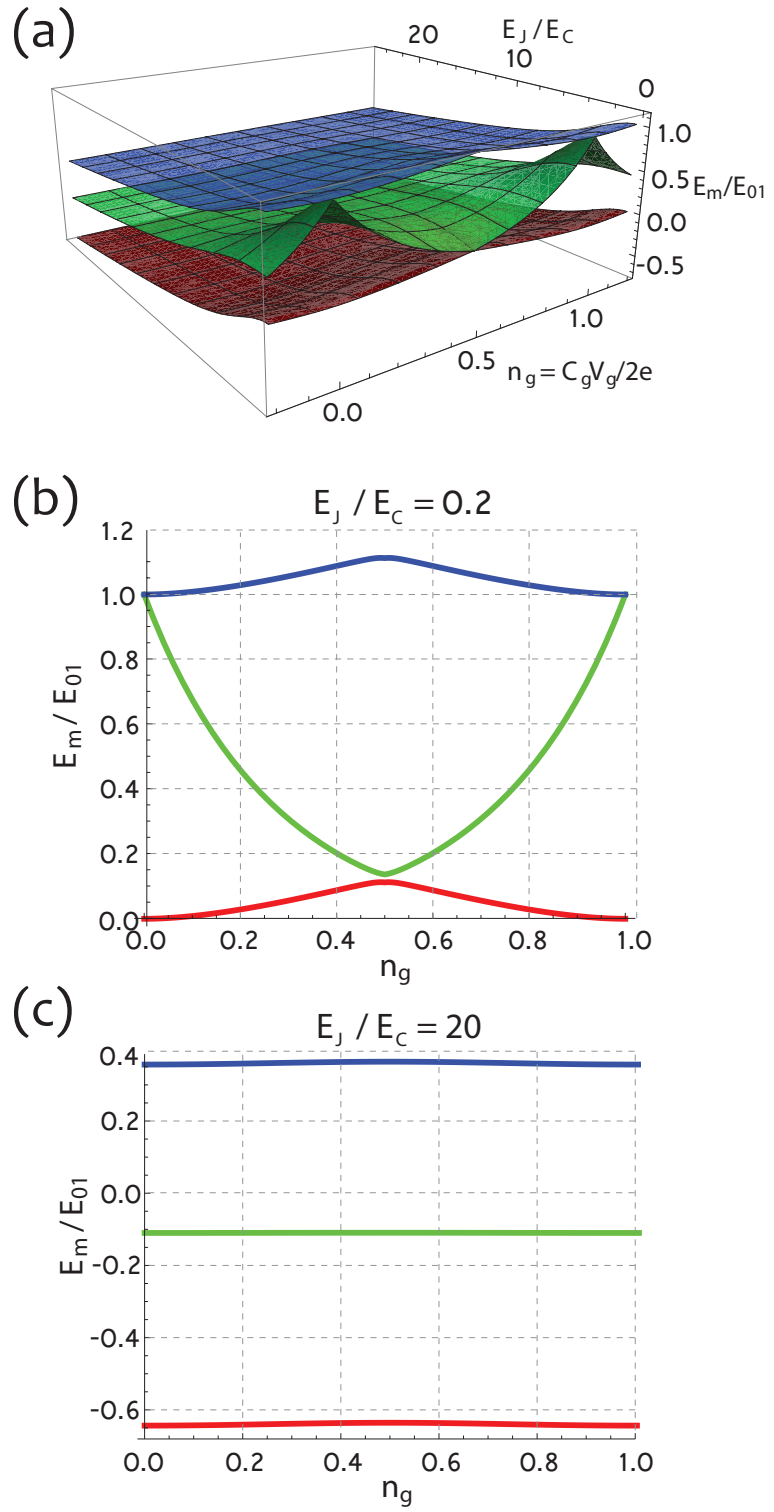

Figure 2.13: **(a)** Calculated energy band diagram for the three lowest energy levels as a function of reduced gate charge and ratio of E_J/E_C. **(b)** The charge limit diagram when $E_J/E_C = 0.2$ for the CPB. **(c)** The transmon regime, plotted for the case when $E_J/E_C = 20$.

2.4.2 The transmon regime

To overcome the sensitivity to charge noise of the CPB, the transmon qubit was proposed by J. Koch *et al.* [39] and is today one of the most popular superconducting qubit designs. As compared with its ancestor, the charging energy of the transmon is reduced. This is obtained by increasing the sizes of the two islands, see Fig. 2.12(b), thus introducing a dominant capacitance in parallel with the two Josephson junctions, recall the expression in Eq. (2.60). This has the consequence that $E_{\mathrm{J}}/E_{\mathrm{C}}$ is larger and the qubit is entering a new regime, known as the *transmon regime*. The frequency needed to drive transitions between the transmon's ground state $|0\rangle$ and first excited state $|1\rangle$, can be well approximated as,

$$\hbar\omega_a \approx \sqrt{8E_{\mathrm{J}}E_{\mathrm{C}}} - E_{\mathrm{C}}. \tag{2.64}$$

Two essential quantities need to be introduced in the energy band diagram in Fig. 2.13(a), namely the charge dispersion and the relative anharmonicity. The charge dispersion is defined as $\epsilon_m = E_m(n_g = \frac{1}{2}) - E_m(n_g = 0)$, *i.e.* the peak-to-peak value of the variation of eigenenergy of the m^{th} level. The smaller the charge dispersion gets, the less the qubit frequency will change in response to gate charge fluctuations. Thus, the charge dispersion is a measure of the qubit's sensitivity to charge noise.

The relative anharmonicity is defined as $\alpha_r = (E_{12} - E_{01})/E_{01}$, where E_{01} and E_{12} are the two lowest energy transitions of the system. Too small anharmonicity leads to the risk of driving unwanted higher transitions if too strong (or spectrally wide) pulses are used. Thus, the transmon no longer act as a qubit but rather a harmonic oscillator.

Both the charge dispersion and the anharmonicity has a common dependence in the ratio of the Josephson and the charging energies $E_{\mathrm{J}}/E_{\mathrm{C}}$. As Koch *et al.* derived, the charge dispersion decreases exponentially when $E_{\mathrm{J}}/E_{\mathrm{C}}$ is increased and the energy levels become almost flat when $E_{\mathrm{J}}/E_{\mathrm{C}} \gtrsim 20$. However, the prize to pay for the reduced charge dispersion is that the anharmonicity of the energy levels also decreases. Fortunately, the latter has only a weak power dependence on $E_{\mathrm{J}}/E_{\mathrm{C}}$. Thus, it is possible to enter into a regime where the transmon is virtually insensitive to charge noise, maintaining a sufficiently large anharmonicity for the system to act as an effective two-level system. This range of $E_{\mathrm{J}}/E_{\mathrm{C}} \gtrsim 20$ for which the transmon has sweet spots everywhere is known as the transmon regime, see Fig. 2.13(c).

2.4.3 Dispersive readout of qubits

After having established the key parameters of the transmon qubit, it is time to discuss how the qubit is utilized to carry out quantum computational tasks. In circuit QED, the qubit is often placed inside a superconducting resonator, both to protect the qubit from classical and quantum fluctuations in the environment and to read out the state of the qubit by probing the resonator. This method is commonly used and is referred to as dispersive readout.

The interaction between the quantized field inside the resonator with frequency, ω_r, and the two-level artificial atom with transition frequency, ω_a, can be described by the Jaynes-Cummings model [46,47]. In this model, the resonator is described by the Hamiltonian of a harmonic oscillator in terms of the creation and annihilation

operators, $\hat{a}^\dagger$ and $\hat{a}$, respectively. If we only allow the qubit (or atom) to be in two states, we can use the Pauli z-matrix notation for a spin-1/2 system, $\hat{\sigma}_z = \hat{\sigma}_{00} - \hat{\sigma}_{11} = |0\rangle\langle 0| - |1\rangle\langle 1|$. The Hamiltonian of the coupled system is then given as,

$$\hat{H} = \underbrace{\hbar\omega_r \left(\hat{a}^\dagger \hat{a} + \frac{1}{2}\right)}_{\text{resonator}} + \underbrace{\frac{\hbar\omega_a}{2}\hat{\sigma}_z}_{\text{qubit}} + \underbrace{\hbar g \left(\hat{\sigma}_+ + \hat{\sigma}_-\right)\left(\hat{a} + \hat{a}^\dagger\right)}_{\text{interaction}}, \tag{2.65}$$

where $\hat{\sigma}_+ = \hat{\sigma}_{01} = |0\rangle\langle 1|$ and $\hat{\sigma}_- = \hat{\sigma}_{10} = |1\rangle\langle 0|$ describes the processes of exciting and de-exciting the atom, respectively. The last term of the Hamiltonian in Eq. (2.65) denotes the interaction between the atom and the resonator and consists of four terms. Two of these, $\hat{\sigma}_- \hat{a}^\dagger$ and $\hat{\sigma}_+ \hat{a}$, share the property of conserving energy since the excitation is moved between the two systems. The two other terms, *i.e.* $\sigma_+ \hat{a}^\dagger$ and $\sigma_- \hat{a}$ can be dropped when the coupling rate is much smaller than the two transition frequencies, $g \ll \omega_a, \omega_r$, which is normally the case. This operation is known as the rotating wave approximation and yields the common form of the Jaynes-Cummings Hamiltonian, representing an important tool when analyzing system dynamics in many quantum optics experiments

$$\hat{H}_{\text{JC}} = \hbar\omega_r \left(\hat{a}^\dagger \hat{a} + \frac{1}{2}\right) + \frac{\hbar\omega_a}{2}\hat{\sigma}_z + \hbar g \left(\hat{\sigma}_+ \hat{a} + \hat{\sigma}_- \hat{a}^\dagger\right). \tag{2.66}$$

Within the framework of the Jaynes-Cummings model, there are two very distinct regimes which we will describe next.

The resonant regime of vacuum Rabi oscillations

When the resonator and atom are close to resonant with each other ($\omega_r \approx \omega_a$), the photon number state of the resonator, $\hat{n} = \hat{a}^\dagger \hat{a}$, and the two states $|0\rangle$ and $|1\rangle$ of the qubit are no longer eigenstates of the Hamiltonian in Eq.(2.66). Instead, the system takes eigenstates on the form of entangled states between the resonator and qubit states

$$|n, \pm\rangle = \frac{|0\rangle\,|n\rangle \pm |1\rangle\,|n-1\rangle}{\sqrt{2}}, \tag{2.67}$$

where the splitting between the symmetric and anti-symmetric superposition states are split by $\sqrt{n} 2g\hbar$. At the point when the two systems are exactly on resonance, $\omega_r = \omega_a$, energy will get coherently swapped between the two systems at a rate $\Omega_R = \sqrt{n} g/\pi$, known as the vacuum Rabi frequency. By measuring the size of the avoided level crossing, the coupling rate g can thus be directly extracted experimentally.

The dispersive regime of cavity pull and ac-Stark shift

The next important regime is when the atom and resonator are far detuned from each other (as compared to the qubit-resonator coupling g_{01}), such that $\Delta = |\omega_a - \omega_r| \gg g_{01}$, no atomic transitions can exchange photons between the systems. However, fortunately for quantum information technology, there is still a dispersive coupling present, which gives rise to small frequency shifts. In this so-called *dispersive regime*, the Hamiltonian can no longer be solved analytically. Instead, by using second order time dependent perturbation theory in terms of g_{01}/Δ, it can be approximated by

$$\hat{H}_{\text{DISP}} = \hbar\tilde{\omega}_r \left(\hat{a}^\dagger \hat{a} + \frac{1}{2}\right) + \frac{\hbar\omega_a}{2}\hat{\sigma}_z, \tag{2.68}$$

where the resonator frequency has picked up a term which is dependent on the state of the atom, $\tilde{\omega}_r = \omega_r \pm \chi\hat{\sigma}_z$, with the dispersive shift given as[5]

$$\chi = \chi_{01} + \frac{\chi_{12}}{2} = \frac{g_{01}^2}{\Delta}\left(\frac{E_C}{\Delta - E_C}\right). \tag{2.69}$$

This shift allows us to perform *dispersive read-out* by reading out the resonator response at a frequency chosen to maximize the contrast between the two states, thus projecting the qubit state onto $|0\rangle$ or $|1\rangle$.

Another way to analyze the dispersive Hamiltonian in Eq. (2.68) is obtained by re-arranging the terms, moving the shift to the atomic transition frequency, such that

$$\hat{H}_{\text{DISP}} = \hbar\omega_r \left(\hat{a}^\dagger \hat{a} + \frac{1}{2}\right) + \frac{\hbar}{2}\left(\omega_a + \frac{2g_{01}^2}{\Delta}\hat{a}^\dagger\hat{a} + \frac{g_{01}^2}{\Delta}\right)\hat{\sigma}_z. \tag{2.70}$$

Now, instead of letting the qubit pull the resonator, we see that the photon number in the resonator, $\hat{n}$ give rise to a shift of the qubit transition frequency by an amount of $2g_{01}^2/\Delta$ per photon, known as the *ac-Stark shift* [48]. In addition, it is shifted by a constant frequency of g_{01}^2/Δ. This shift originates from the zero-point energy of the resonator and is known as the *Lamb shift* [49].

2.4.4 Qubit coherence measurements

A major challenge when it comes to designing a successful quantum information architecture is to find a balance between two contradictory aspects; First, the system needs to be well enough isolated not to suffer from both classical and quantum interactions with its environment, causing energy relaxation. Second, we need to be able to control the qubits of the processor, thus interacting with them, in order to manipulate and gain access to the quantum information. In this section, the experimental techniques employed when extracting the quantum coherence properties are presented.

We characterize this coherence in terms of an energy relaxation time, T_1 and a dephasing time, T_2. After identifying the qubit frequency using spectroscopy, we first perform a measurement of Rabi oscillations where an excitation pulse of increasing duration is applied at the qubit frequency, followed by a readout pulse on the resonator. From the Rabi oscillations, we can extract the pulse length (for a given pulse amplitude) required to excite the qubit from its ground state $|0\rangle$ to its first excited state $|1\rangle$, see Fig. 2.14(a). Such a pulse is called a π-pulse.

Next, we can use our calibrated π-pulse duration to perform a Ramsey measurement in which the delay between two $\pi/2$-pulses (half as long as the π-pulse) is gradually increased followed by the readout pulse, see Fig. 2.14(b). After the first $\pi/2$-pulse, the qubit ends up in a superposition state between $|0\rangle$ and $|1\rangle$. Well there, phase noise acting on the qubit will smear out the state on a time scale given

[5]Due to the limited anharmonicity of the transmon qubit, a correction to the dispersive shift is needed to explain the experimentally observed frequency shift.

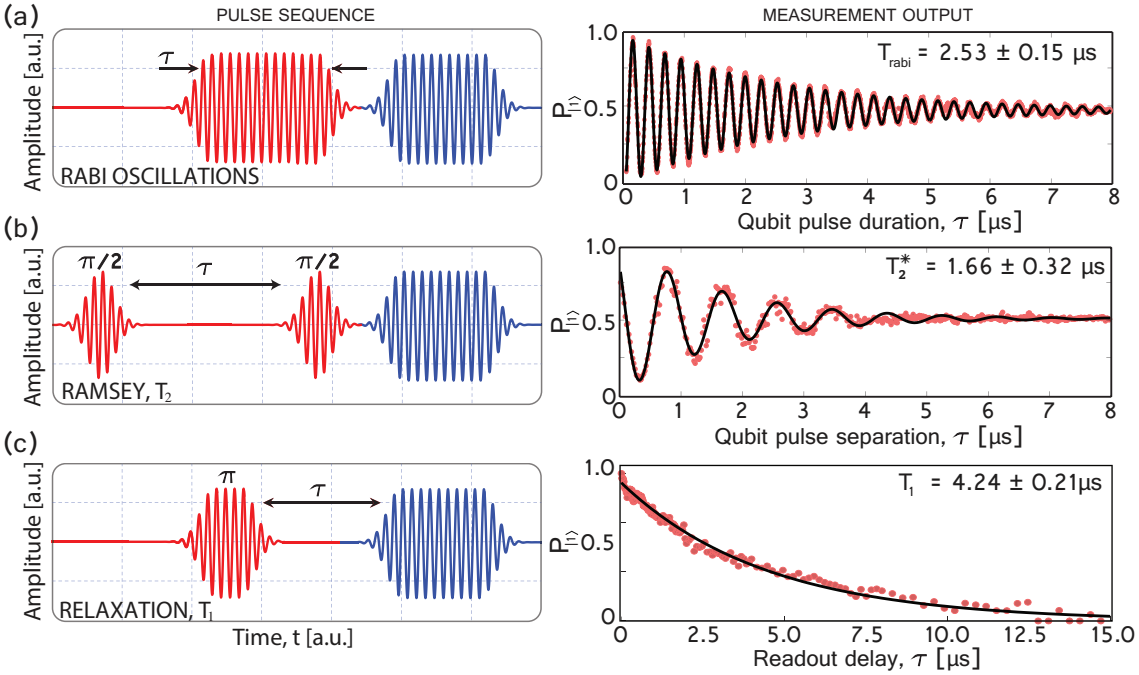

Figure 2.14: The pulse schemes and measurement output from the qubit coherence measurements, expressed in probability to find the qubit in its excited state, $P_{|1\rangle}$. **(a)** A Rabi oscillation measurement, where a gradually increased qubit excitation pulse is applied, followed by a readout pulse. **(b)** Ramsey free-induction decay measurement of T_2^*, where two $\pi/2$-pulses are applied, separated by a swept separation time. **(c)** Qubit relaxation measurement of T_1, where the delay between the π-pulse and the readout pulse is swept. The qubit drive pulses at ω_q are indicated with red, whereas the resonator drive at ω_r pulses used to readout the state of the qubit are indicated with blue.

by the dephasing time, T_2. This means that if we project back the state onto the $\hat{z}$-axis using a second $\pi/2$-pulse after which the state is read out, the dephasing time can be revealed from the envelope of these so-called Ramsey fringes.

Finally, we can extract the relaxation time, T_1 of the qubit by applying a π-pulse and gradually increase the delay between the qubit exciation and readout pulses, see Fig. 2.14(c). To reliably characterize the system, the above mentioned pulse schemes are repeated and the measurement outputs are averaged.

2.5 The Josephson parametric oscillator qubit readout

The main result of this thesis is the proposal and demonstration of a single-shot qubit readout scheme, where information about the qubit state is encoded into two different states of a parametric oscillator to which the qubit is coupled. In this section, the reader is first introduced to some previously developed readout schemes, all based on parametrically driven systems. After that, the main working principle behind our device is outlined, which from now on is referred to as the "Josephson parametric oscillator" (JPO).

2.5.1 The family-tree of parametric readout schemes

To overcome poor signal-to-noise ratios haunting traditional dispersive readout of superconducting qubits connected to linear resonators[6], several non-linear, parametric circuits have been developed. Dispite some differences in how these are designed and operated, most of them are based on the nearly dissipationless nonlinearity of Josephson junctions [50–59].

By introducing a small Josephson inductance into the superconducting resonator, the equation of motion for the resonator field amplitude, A, takes the form of a parametrically pumped Duffing oscillator, recalling the simplified Langevin equation (2.45), in a frame rotating at the resonator frequency

$$i\dot{A} + \delta A + \epsilon A^* + \alpha |A|^2 A + i\Gamma A = \sqrt{2\Gamma_0} B(t). \tag{2.71}$$

In Eq. (2.71), as we recall from section 2.2.4, the field amplitude, A, is normalized such that $|A|^2$ corresponds to the equivalent number of photons in the resonator. The detuning between the parametric pump and the resonant frequency is given by $\delta = \omega_p/2 - \omega_r$, whereas the strength of the pump is denoted, ϵ. The Duffing parameter and damping parameters are denoted, α and Γ,Γ_0, respectively. Finally, the probe signal, $B(t)$, on the right hand side of Eq. (2.71) denotes the photon flow entering the system via the coupling port.

There are two main ways to utilize this system as a quantum-limited amplifier, depending on which term of Eq. (2.71) that we choose to address: the first way is to apply a resonant current drive of the Josephson junctions, $B \neq 0$, which is the case for all current driven devices, whereas the second way is to parametrically pump the resonant frequency, ω_0, (or damping) of the system at a rate close to twice the resonant frequency, $\omega_p \approx 2\omega_r$. In the latter case, another degree of freedom is obtained and parametric oscillations (PO) build up the field inside the resonator if the pump exceeds the total damping rate of the system, $\epsilon > \Gamma$, even in the absence of an input signal at the resonator frequency.

In Fig. 2.15, some of these devices are placed into a diagram, and listed in Table 2.1, which puts the results presented in this thesis into the context of previously developed schemes. The division is made with regards to whether the nonlinearity is exploited through current, $B \neq 0$, and/or flux-pumping, $\epsilon \neq 0$. On top of the type of applied drive, we also further separate the schemes into two categories from the viewpoint of implementation: in one category, the parametric amplifier

[6]The reason to why it is not possible to just increase the probe signal is due to the fact that the dispersive approximation is no longer valid for a large intra-cavity photon number, exceeding the critical photon number, $n_c = (\Delta/2g_{01})^2$. [3]

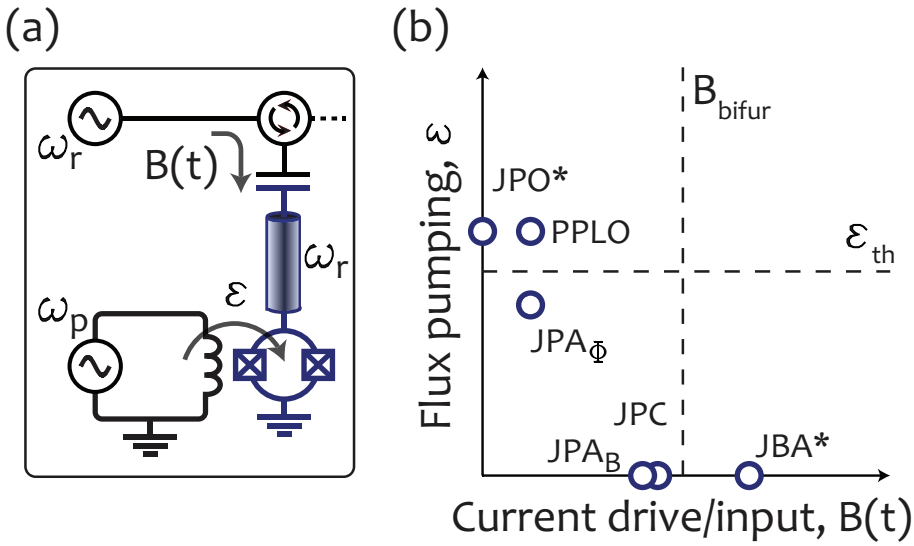

Figure 2.15: Overview of different parametric readout schemes. **(a)** Schematic illustration of two different ways to drive the system: either a tone is applied through the coupling capacitor, $B(t) \neq 0$, or by parametrically modulating the resonant frequency via the pump line. **(b)** Overview of different amplification schemes, divided into flux pumping and current drive/input. Here, the JPO belongs to the Josephson junctions, $B \neq 0$, or by pumping the flux of a SQUID loop, $\epsilon \neq 0$. Moreover, the devices in which the qubit is directly integrated with the amplifier are denoted with an asterisk *.

is a separate device from the resonator to which the qubit is coupled acting as a pre-amplifier to the cryogenic HEMT amplifier[7]. In the second category, to which we also attribute the JPO presented in Appended paper II, the qubit is directly intergrated with the amplifier, then acting as a detector rather than an amplifier. To this category belongs also the current-pumped, hysteretic Josephson bifurcation amplifier (JBA) [54, 55, 60, 61]. In Fig. 2.15, these two devices are marked with an asterisk. Even though our readout scheme is new, there are some similarities between our system and previous work which will now be more elaborated.

In 2014, a flux-pumped, parametric phase-locked oscillator (PPLO) was used as a following amplifier, also enabling sensitive qubit readout [53]. In our work, the qubit was directly coupled to the JPO, which simplifies the experimental setup by reducing the number of microwave components needed. Also, with a pumping amplitude below the parametric instability threshold, the flux-pumped JPA has been used to read out one qubit [52], as well as multiple qubits coupled to the same bus resonator [51].

As mentioned above, we can distinguish between two ways of operating the device: instead of pumping the flux at $\omega_p \approx 2\omega_r$, we can apply an alternating pump current ($\epsilon = 0$, $B(t) \neq 0$), now at a frequency close to resonance, $\omega_p \approx \omega_r$, and thereby directly modulate the phase difference, ϕ. Both methods can provide linear parametric gain upon reflection of a detuned signal ($\omega_s \neq \omega_p/2$ and $\omega_s \neq \omega_p$, respectively). The flux-pumped JPA has a very wide frequency separation between pump tone and signal, because $\omega_s \approx \omega_r \approx \omega_p/2$, which is a practical advantage since it makes the resonator's entire instantaneous bandwidth available for amplification

[7]In this case, the parametric amplifier acts as a pre-amplifier to the cryogenic HEMT amplifier, thus reducing the noise temperature of the combined amplifier chain.

with no need to suppress or filter out the pump tone. Moreover, the $\lambda/4$ resonator has no mode in the vicinity of ω_p that the pump might otherwise populate.

We emphasize that there are indeed two different physical mechanisms in play, since flux and current pumping address orthogonal variables in the sense that $\Phi = (\varphi_1 - \varphi_2)\Phi_0/2\pi$ and $\phi = (\varphi_1 + \varphi_2)/2$, where φ_1 and φ_2 denote the gauge-invariant phase differences across the two parallel JJs. This distinction is also evident in Eq. (2.71). The parametric flux-pumping term, ϵA^*, modulates the resonant frequency; it couples the resonator field amplitude and its complex conjugate, which can provide quadrature squeezing of an input signal and enables phase-sensitive parametric amplification; and for stronger modulation there is a parametric instability threshold into the JPO regime – see Fig. 2.16(b).

Current pumping by an input $B(t)$, on the other hand, corresponds to an external force which directly contributes to the intra-resonator field A and drives its nonlinear term $\alpha|A|^2$. For zero detuning, $\omega_s = \omega_p$, this is the driven Duffing oscillator which has no gain (it offers no phase-sensitive amplification); for stronger driving there occurs a dynamical bifurcation but no internal instability or parametric oscillations.

Current-pumping with a moderate amplitude is used for linear amplification with the JPA [29, 62], which enabled, *e.g.*, the observation of quantum jumps in a qubit [50]. Current modulation is also used in the latching detection scheme of the Josephson bifurcation amplifier (JBA) [54, 55, 60, 61, 63]. There, a higher-amplitude input strongly drives the Duffing nonlinearity near its bifurcation point; the two qubit states can then be mapped onto two different resonator output field amplitudes. The JBA was used for quantum non-demolition measurement of a qubit, and in a lumped-element resonator [56], in which a qubit-state sensitive autoresonance was observed in response to a frequency-chirped current drive. Yet another method is to couple the qubit to a linear resonator, which inherits a cross-Kerr nonlinearity from the qubit; current pumping of the resonator can then yield a strong output signal that depends on the qubit state [57, 58].

Device	ϵ	B_s	B_p	# modes	Ref.
JPO*	$> \epsilon_{\rm th}$	0	0	1	Paper II
JPA_Φ	$\lesssim \epsilon_{\rm th}$	$\neq 0$	0	1	[52]
JPA_Φ	$\lesssim \epsilon_{\rm th}$	$\neq 0$	0	multimode	Paper IV
PPLO	$> \epsilon_{\rm th}$	$\neq 0$	$\neq 0$	1	[53]
JPA_B	0	$\neq 0$	$\neq 0$	1	[50]
JBA*	0	0	$\neq 0$	1	[55]
JPC	0	$\neq 0$	$\neq 0$	2	[59]

Table 2.1: Overview of different modes of operation for the various Josephson amplification and detection schemes. The variables refer to Eq. (2.71), where ϵ denotes the flux-pumping amplitude (at $\omega_p \approx 2\omega_r$), and B_s and B_p denote alternating-current signal and pump amplitudes, respectively (at $\omega_p \approx \omega_r$). The two readout methods marked with an asterisk (*) have the qubit directly integrated with the detector, whereas the other devices are used as following amplifiers.

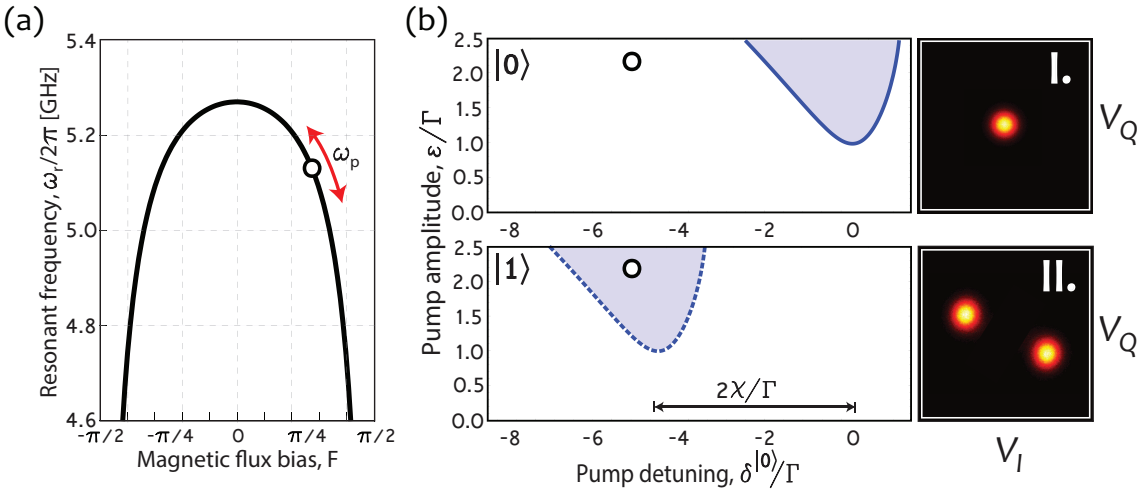

Figure 2.16: Operation of the Josephson parametric oscillator readout. **(a)** Resonant frequency as a function of applied magnetic flux, F. The black circle indicates a static bias point, $\omega_r(F)$, around which the resonant frequency is parametrically modulated at a frequency, $\omega_p \approx 2\omega_r$. **(b)** Parametric oscillation regions for the qubit ground state $|0\rangle$ (solid blue line) and excited state $|1\rangle$ (dashed blue line), respectively. These blue lines represent the bifurcation boundaries, where the number of steady-state solutions to Eq. (2.45) changes. The two panels on the right are measured [I,Q]-quadrature voltage histograms of the device output, revealing two different oscillator states: **I.** Outside of the region of parametric oscillations, the resonator is "quiet" ($|A|^2 = 0$). **II.** Within the region, the resonator has two oscillating states ($|A|^2 > 0$), with a phase difference of π radians.

2.5.2 Operation of the Josephson parametric oscillator readout

The JPO readout relies on two phenomena, both which have been treated previously within this thesis: first, the fact that the parametric oscillations only populate the resonator within a certain region in the plane spanned by the pump frequency and amplitude (recall section 2.2.3), and second, that the qubit exerts a state-dependent frequency shift on the resonator, given that the system operates within the dispersive regime, see section 2.4.3.

In Fig. 2.16, the operation principle of the JPO is illustrated. First, the system is tuned down in frequency such that the parametric pumping of flux has the desired effect of modulating the resonant frequency of the resonator around a static dc-flux bias point, see Fig. 2.16(a). At this flux bias point, the parametric oscillation regions are plotted for the two cases when the qubit is either in its ground state $|0\rangle$ or in its excited state $|1\rangle$, see Fig. 2.16(b). The two panels on the right hand side indicate the quadrature histograms corresponding to the two different states of the qubit, when the pump condition is chosen at the marked circles. From this schematic figure, it is clear that if the dispersive shift is sufficiently large to completely separate the two parametric oscillation regions, it is also possible to distinguish between the two qubit states by probing the response of the parametric oscillator.

Chapter 3

3 Experiments

This chapter is dedicated to take the reader through the essential experimental steps. First, we take a look at the modeling techniques used to design the device. The next step is to fabricate the designed device in the clean room laboratory. Here, the most important fabrication techniques are briefly introduced. For the detailed clean room recipes, the reader is referred to Appendix A.

Towards the end of this chapter, we take a closer look at the microscopy techniques used throughout Appended papers **V** and **VI**. Finally, once the device has been fabricated, it is cooled down to cryogenic temperatures in a dilution refridgerator, where we characterize it by probing it with microwave photons. This is described at the end of this chapter.

3.1 Device modeling

In this section, the device modeling techniques used for the parametric devices are presented. First, we consider the bare resonator design (in absence of the SQUID termination). Then, the contribution from the additional Josephson inductance of the SQUID is taken into account. Finally, to fully be able to predict the parameters of the system, also the transmon qubit is added to the model.

3.1.1 Bare resonator design

The starting point when designing a quarter-wavelength resonator is to match its characteristic impedance to the outside world, such that $Z_c = Z_0 = 50\,\Omega$. As we recall from section 1.3, the characteristic impedance of a transmission line is governed by its inductance and capacitance per unit length, through the relation, $Z_c = \sqrt{L/C}$. Thus, to obtain our desired impedance, we need to simulate L and C for a given dielectric environment of the coplanar waveguide geometry. Instead of using more advanced electromagnetic field analysis, we can get close enough by using analytical expressions employing conformal mapping techniques [64] in a Mathematica script based on the tailored equations resembling the cross-sectional geometry of our device, visualized in Fig. 3.1(a). For details on these conformal mapping expressions, the reader is referred to Appendix C.

Paper	w	g	h_1	h_2	h_3	h_4	ϵ_1	ϵ_2
I. (SiO_2)	10.00	5.500	380.0	0.400	380.4	500.0	11.68	3.900
II. (Al_2O_3)	15.00	6	300.0	-	300.0	500.0	11.3[1]	-

Table 3.1: Input dimension parameters for the conformal mapping script, all length dimensions are given in units of μm.

Paper	ϵ_{eff}	v_{ph} $[c]$	C [pFm^{-1}]	L [μHm^{-1}]	l [μm]	$\omega_{\lambda/4}/2\pi$ [GHz]
I. (SiO_2)	6.34	0.397	165	0.426	4960	5.65
II. (Al_2O_3)	6.15	0.403	177	0.385	5447	5.55

Table 3.2: Output parameters from the conformal mapping script, presented in Appendix C.

The implemented model can be used for both single and bilayer substrates. In this thesis, we have used both oxidized silicon (Paper I) and sapphire wafers (Paper II), with relative dielectric constants and geometries presented in Table 3.1. The generated output parameters, illustrated in Fig. 3.1(b), are in turn presented in Table 3.2.
After having established the cross-sectional design, the acquired knowledge about the effective dielectric constant can be used to calculate the fundamental frequency mode of the resonator using Eq. (2.1) for a certain physical length, l,

$$f_{\lambda/4} = \frac{c}{4l\sqrt{\epsilon_{\text{eff}}}}. \tag{3.1}$$

3.1.2 Coupling capacitor

Next we turn our attention to the design of the coupling capacitor, C_c, defining the rate at which photons are exchanged with the input/output probe line, referred to as the external coupling (or damping) rate, $\Gamma_0 = \omega_r/2Q_e$. This coupling is very important when it comes to resonators used to readout the state of a qubit in circuit QED, since it sets the time scale after which information can be extracted from the system, $\tau = 1/\Gamma_0$. However, if this coupling is too strong, the qubit will suffer from an enhanced relaxation rate, known as the Purcell effect.

Often, it is convenient to design the coupling capacitor having in mind the external quality factor, which can be related to the coupling capacitor using the lumped element representation of the resonator connected to a load impedance, Z_0, as

$$\begin{aligned} Q_{\text{e}} &= \frac{(1+(\omega_{\lambda/4}C_cZ_0)^2)(Cl/2+C_c)}{\omega_{\lambda/4}C_c^2Z_0} \approx \\ &\approx \frac{Cl/2+C_c}{\omega_{\lambda/4}C_c^2Z_0} = \frac{\sqrt{L_r/C_c}}{Z_0}\left(1+\frac{Cl/2}{C_c}\right)^{3/2}, \end{aligned} \tag{3.2}$$

where the bare angular frequency of the resonator is given as

$$\omega_{\lambda/4} = 1/\sqrt{L_r(Cl/2+C_c)}. \tag{3.3}$$

Eq. (3.2) thus allows us to calculate the coupling capacitance needed to obtain a certain external quality factor. For instance, if we aim for an external quality factor

of $Q_e = 5000$, this corresponds to a coupling capacitance of $C_c = 4.9$ fF for a bare resonator frequency $\omega_{\lambda/4}/2\pi = 5.5\,\mathrm{GHz}$.

The next, and perhaps more challenging question to address is what physical design of a capacitor will result in the desired capacitance for our dielectric environment at hand. We calculate the capacitance of the interdigital finger capacitor using an electromagnetic simulator in MicroWave Office. A micrograph of a coupling capacitor and the four-port simulation setup are illustrated in Fig. 3.1(b), with resulting output parameters.

3.1.3 Non-linear SQUID inductance

The SQUID termination of the CPW provides the flux-dependent inductance that makes the resonator parametrically frequency-tunable [65]. We denote the participation ratio of the Josephson inductance to the total inductance of the CPW as $\gamma_0 = L_s(\Phi_{\mathrm{dc}} = 0)/Ll$, where the zero-flux Josephson inductance of the SQUID is given as

$$L_s(\Phi_{\mathrm{dc}} = 0) = \frac{\Phi_0}{2\pi I_c}. \tag{3.4}$$

We estimate the geometric inductance per unit length, L, using the model described in Fig. 1.3(b). We then design the resonator and SQUID, aiming for a typical target value of $\gamma_0 = 5\,\%$.

An experimentally reliable estimate of the Josephson inductance can be obtained by measuring the normal state resistance of identically fabricated test structures, placed within four-point measurement sites on-chip, see Fig. 3.1(c). From the measured normal state resistance, R_n, the Josephson inductance can be calculated from the simple relation,

$$L_{s,0} = \frac{\Phi_0 R_n e}{\pi^2 \Delta(0)}, \tag{3.5}$$

where $\Delta(0) \approx 0.2$ meV denotes the superconducting gap of Al at zero temperature.

As we will discuss in the next section, the Josephson junctions are fabricated by oxidizing the Al during the two-angle evaporation sequence. It is intuitive that a longer oxidation time, t_{ox}, and higher pressure, P_{ox}, will render a thicker insulating barrier between the two superconducting Al electrodes. Therefore, the tuning of Josephson inductance can, apart from the lithographical geometry of the junctions, also be done during the clean room processing by tuning the evaporation angle and the oxidation parameters.

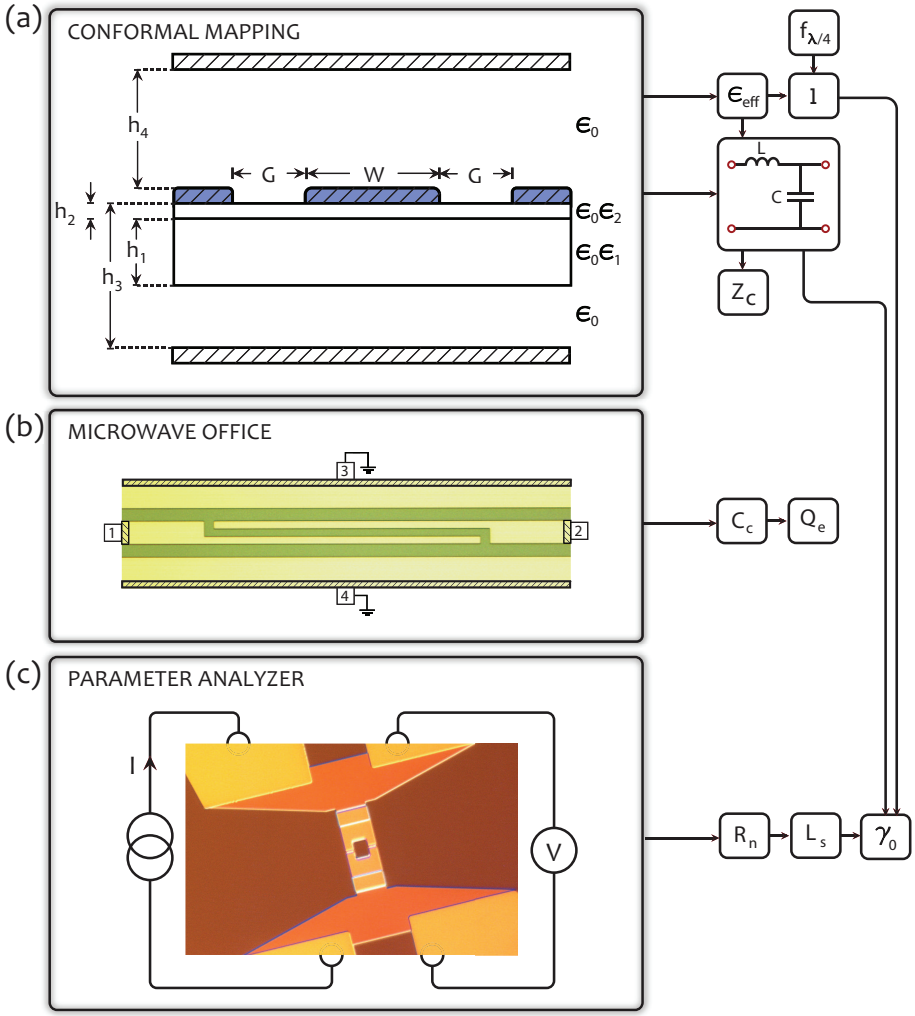

Figure 3.1: Overview of the modeling and design processes. **(a)** Cross section dimensions of the coplanar waveguide geometry. The thicknesses of each layer are denoted h_1-h_4 to the left. The superconducting metal (in dashed blue), is placed on top of a bilayer substrate with dielectric constants ε_1 and ε_2, and is surrounded by top and bottom enclosures separated by vacuum from the device. The output parameters are the inductance and capacitance per unit length as well as the effective dielectric constant from which the characteristic impedance can be calculated. **(b)** Micrograph illustrating how the capacitance of the interdigital finger capacitor is extracted using a four-port electromagnetic simulation in MicroWave Office. The output parameter of the simulation is the coupling capacitance, which via Eq. (3.2) gives us the external quality factor. **(c)** Micrograph of one of the four-point resistance test structure sites on the samples. A current is injected between the left most pads, whereas the voltage across the junction is measured on the other side. The output parameter is the normal state resistance, leading to the Josephson inductance through Eq. (3.5). Finally, the participation ratio, γ_0 can be calculated from the ratio between the SQUID and the geometrical inductances.

3.1.4 Modeling the transmon qubit

When using the Josephson parametric oscillator as a qubit readout, also the presence of the qubit coupled to the resonator will influence its properties due to the dispersive coupling. To take this into account, it is essential to be able to predict the two aforementioned energies of the transmon qubit, namely the Josephson and charging energies, see section 2.4, yielding its fundamental transition frequency,

$$\omega_a/2\pi \approx \sqrt{8E_J E_c} - E_c. \tag{3.6}$$

Here, the Josephson energy, $E_J = \Phi_0 I_c/2\pi = \Phi_0\Delta/4R_n e$, can be predicted from fabrication by measuring its normal state resistance, R_n. The charging energy, $E_c = e^2/(2C_\Sigma)$, however, has to be well modeled prior to fabrication since it is governed by the total capacitance of the transmon which can be expressed as,

$$C_\Sigma = C_s + C_g, \tag{3.7}$$

where $C_s = C_{23} + C_J$ is the shunt capacitance between the two islands and C_g is the gate capacitance, governed by the capacitive network around the transmon, see Fig. 3.2. However, by neglecting the smallest contributions the gate capacitance can be approximated as

$$C_g = \frac{(C_{34} + C_{13})(C_{24} + C_{12})}{C_{34} + C_{13} + C_{24} + C_{12}} \approx \frac{C_{34}C_{12}}{C_{34} + C_{12}}. \tag{3.8}$$

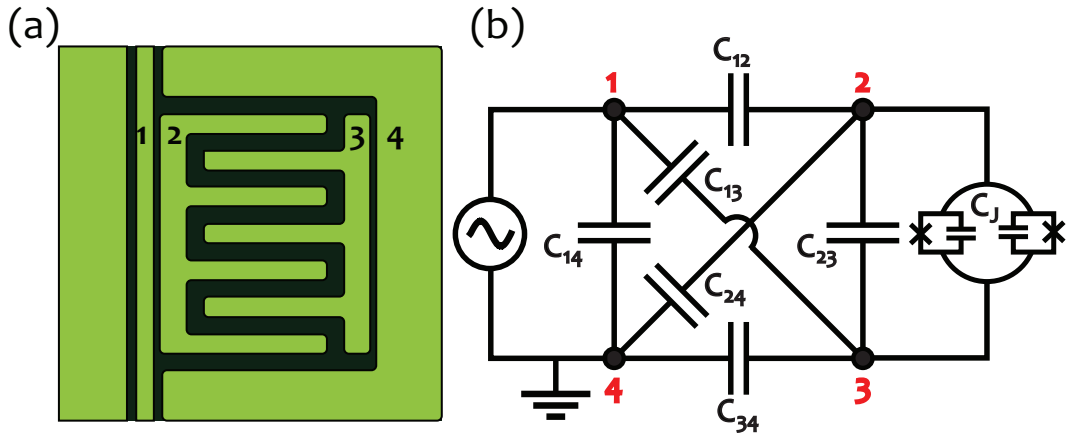

Figure 3.2: **(a)** Illustration of the capacitor network of the transmon. **(b)** Corresponding circuit model, taking into account all capacitances present in the circuit.

3.2 Nanofabrication

All of the devices presented throughout this thesis were fabricated in the MC2 Nanofabrication Laboratory at Chalmers University of Technology. In this section, the main fabrication techniques are introduced. For the detailed recipes, the reader is referred to Appendix A. In addition, this section is provides some details on the observed microstructure of the fabricated Josephson junctions, presented in Appended papers V and VI.

3.2.1 Pre-annealing and sputtering

Prior to the device patterning, the 2" c-plane sapphire wafer is pre-annealed $10\,h$ at $1100°C$ in a tube furnace with an atmosphere of O_2:N_2, 1:4. The annealing is done to reduce the surface roughness of the surface by flattening the terrasses present on the wafer surface [66–68]. After the annealing, a 80 nm-thick Nb film is deposited using dc-magnetron sputtering. These two steps are illustrated in Fig. 3.3(a)-(b).

3.2.2 Photolithography

Due to the large variations in feature dimensions and resolution requirements, processing time can be saved by first using photolithography to define the large features, which in our case are the contact pads, ground planes, and the alignment marks for the electron beam lithography. The main steps in this process are summarized and described in Fig. 3.3(c)-(g). After cleaning the wafer, it is coated with a bi-layered resist system consisting of a lift-off resist (LOR3B) and a positive photoresist (S1813)[2], see Fig. 3.3(c).

Using a mask aligner, operated in low-vacuum mode, the coated wafer is then exposed to UV-light through a soda-lime photomask with a patterned Cr film, see Fig. 3.3(d). To develop the exposed pattern, the wafer is immersed into a water-based solvent (MF319), which dissolves the exposed resist, while leaving the parts covered by the Cr on the photomask. The two resists have different properties: while the top resist acquires sharp edges with high resolution, the bottom resist develops isotropically forming an undercut, see Fig. 3.3(e). After the development, organic residues from the resists are etched away in oxygen plasma before the wafer is placed in an electron-beam evaporator with high vacuum. For contact pads, a tri-layer metal stack is evaporated. First, 3 nm thin layer of Ti is deposited as a sticking layer to improve the SiO_2/Au adhesion. Then, 80 nm of Au is evaporated as contact material, followed by 10 nm of Pd acting as a stopping layer to prevent diffusion between the Au and Al, see Fig. 3.3(f). Finally, the excess metal is lifted-off using S1165 Remover, dissolving all remaining resist, see Fig. 3.3(g).

3.2.3 Reactive ion etching

To define the relatively large features of the design, such as the superconducting resonators, coupling capacitors, and pump lines, we use electron beam lithography (discussed below) followed by reactive ion etching. Specifically, we are using an Oxford Plasmalab 100, with an inductively coupled plasma generated with a magnetic

[2]Positive resist refers to the polymer property that the parts exposed by UV-light can be dissolved in solvent during the development.

field, using an RF generator. Another RF generator is applied to the silicon or sapphire substrate, which yield a more directional electric field in order to obtain an anisotropic etch profile. In our process, described in Fig. 3.3(h)-(k), NF_3 gas is used for the etching of the Nb layer.

To find the correct time after which the etching should stop, the machine is equipped with a laser interferometer. By pointing the laser beam at an area that will be completely etched, the interferometer can sense when the laser is pointing at another material with different lattice constant. For a sapphire substrate this is not very critical, since the etching rate in sapphire is orders of magnitude slower than in Nb.

Finally, to be able to remove the resist, oxygen plasma is used to etch through the hard surface of the resist which results after this etching process.

3.2.4 Electron-beam lithography

Due to the limited resolution of photolithography, as well as the need for design flexibility, some features where patterned using electron beam lithography (e-beam lithography). The idea of this fabrication technique is (as the name suggests) to scan a focused beam of electrons into an e-beam resist, locally changing its solubility. As oppose to photolithography, the pattern can therefore be directly transferred onto the wafer, without the need of a photomask. After the exposure, the resist can be selectively developed by immersing the exposed wafer into a solvent yielding a resolution set by the type or resist, the spotsize of the beam used during the exposure, and the choice of developer. There are, however, certain difficulties associated with e-beam lithography that we need to take into consideration. Two such obstacles are proximity and charging errors, which we will discuss in more depth below.

Proximity errors and correction

One of the most common issues when exposing narrow features is the proximity effect, whereby the electrons from adjacent regions scatter into areas within its proximity, hence giving rise to unwanted exposured regions. This results in an effective exposed region which is larger than the intended pattern and induces a bound on the resolution and contrast of the e-beam exposure. Fortunately, the proximity effect due to scattered electrons can be compensated for by solving the inverse problem and calculating the exposure function E(x,y), yielding a dose distribution as close as possible to the intended dose. The proximity correction was done using the software BEAMER^{TM}, where the nominal dose was divided into 127 doses, and positioned throughout the pattern with respect to the adjacent exposure. To illustrate how the pattern is corrected, let us consider the pattern for a transmon qubit, see Fig. 3.4(a). From the given design, the software calculates a mesh grid with assigned doses based on a dose profile modeled from the substrate we that is used. Finally, the adjusted doses are assigned to the different fields based on the acceleration voltage (100 keV) and a beam current (2 nA), see Fig. 3.4(c).

Charging errors

The next important issue arises from the negative charge of the electrons. It is important that the exposed wafer is properly grounded so that the charges do not

stay inside the wafer thus giving rise to charging errors. This is not an issue for conducting substrates like Si. However, for insulating substrates such as sapphire, electrons can get repelled from a region where charges have built up if these cannot be removed. This can manifest itself in slightly different ways, depending on the degree of the problem. Usually, it results in a small offset and/or somewhat scattered pattern. For smaller acceleration voltages (less than 50 keV), the charging effect can be accounted for by using a thin conducting layer on top of the resist (either a metal like Al or a conductive resist such as E-spacer). However, this layer plays a limited role if the acceleration voltage is higher, since the charge then reaches much deeper and will not return back to the surface. To prohibit charging errors, it is important to think about ground paths while designing the pattern, keeping as large part of the design grounded.

3.2.5 Two-angle evaporation

After defining the smallest features by electron beam lithography, the Josephson junctions are created using two-angle evaporation (shadow evaporation) of aluminum [69] in an electron-beam evaporator from Plassys. A sequential description of this process is shown in Fig. 3.3(o)-(r). First, a bottom layer of Al is evaporated under an angle η of the stage on which the sample is mounted, see Fig. 3.3(o). Typically, this layer is between 20 and 50 nm-thick. After finishing the first Al layer, the acceleration voltage of the gun is ramped down, and the load lock is filled with pure O_2-gas at a regulated pressure, P_{ox}. This results in the formation of a thin insulating barrier of amorphous AlO_x, see Fig. 3.3(p). The oxygen is pumped out after a desired oxidation time t_{ox} has elapsed. To define the top electrode, a second layer of Al is evaporated from the opposite angle, $-\eta$ as compared with the bottom layer, see Fig. 3.3(q). When choosing the thickness of the top electrode, it is essential to keep in mind which thicknesses the evaporated film need to be able to overlap with a decent step coverage to ensure a continous film. This layer needs to be thicker than the first layer. In addition, since we also need the Al to overlap onto the Nb on both sides, the total Al thickness needs to exceed that of the sputtered Nb layer. Finally, the resist is lifted off, and we are left with the Josephson junctions, see Fig. 3.3(r). In addition to the design dimensions of the two tunnel junctions, its critical current can be tuned using the two oxidation parameters, t_{ox} and P_{ox}. In the next sections, we take a closer look at what impact our choice of junction parameters have on the microstructure of the Josephson junctions.

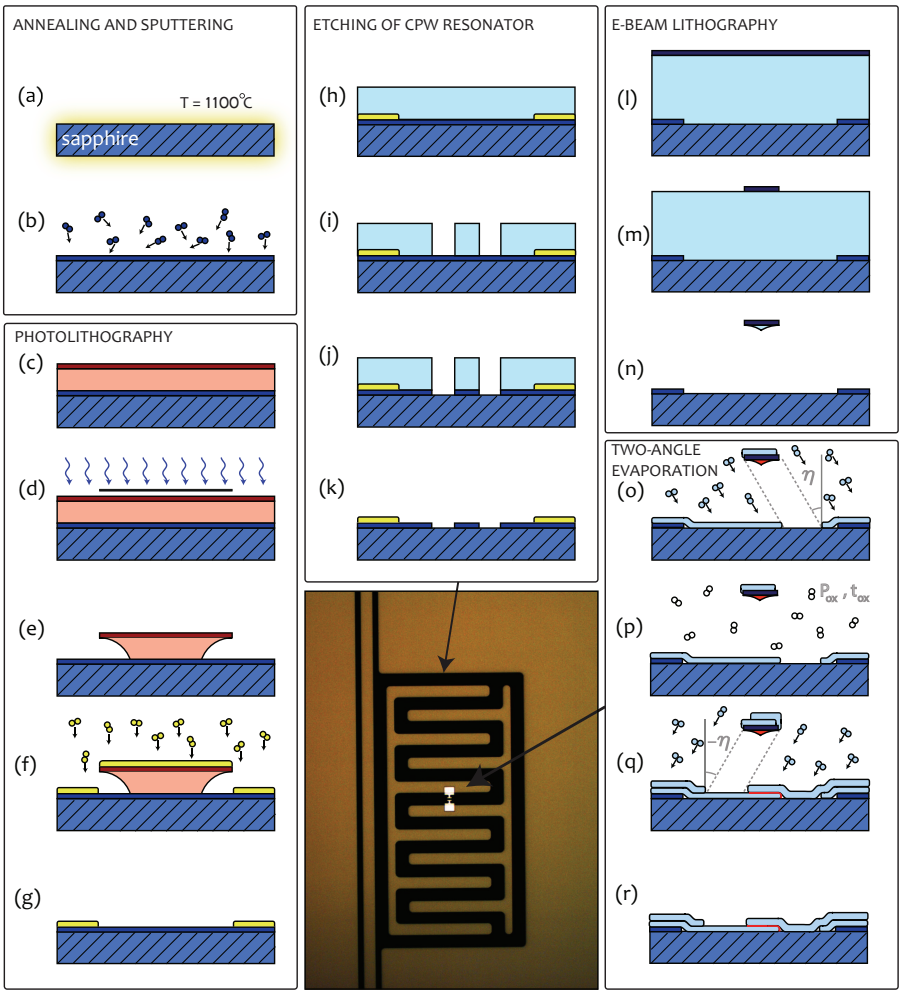

Figure 3.3: The main steps of the fabrication processes. **(a)-(b)** show the pre-annealing and sputtering of the sapphire wafer. **(c)-(g)** describes the photolithography process used to define and deposit the contact metals for bond pads, alignment crosses, and ground planes. In **(h)-(k)**, the etching process used to define the gaps in the Nb film *e.g.* the gaps of the CPW and the transmon islands. **(l)-(n)** show the e-beam lithography process used to define the Josephson junctions. Finally, **(o)-(r)** illustrate the two-angle evaporation technique used to fabricate the Josephson junctions. **Inset:** Transmon qubit coupled to a CPW resonator fabricated using this recipe.

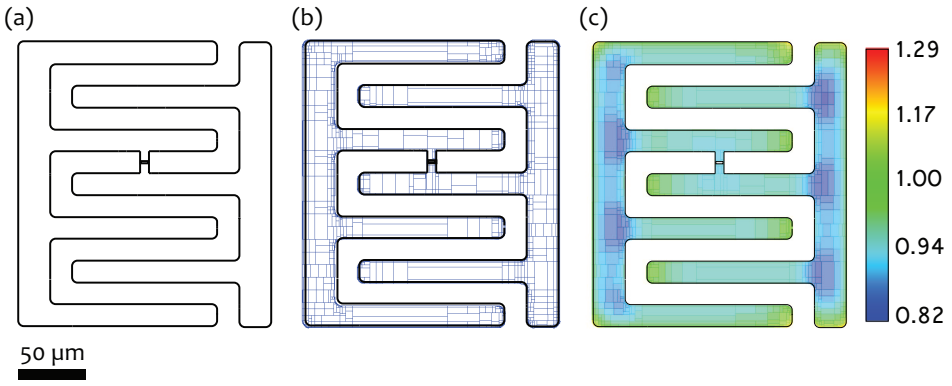

Figure 3.4: **(a)** Outline of pattern. **(b)** Grid division for doses. **(c)** Proximity corrected pattern with dose distributions given by the color scale. The parts of the pattern close to other regions of exposure are tuned down in dose, whereas the edge parts got assigned a higher dose.

3.3 The microstructure of Josephson junctions

Throughout this thesis, all our superconducting devices are based on Josephson junctions. In this section, we take a closer look at the microstructure of our Josephson junctions and how it is reflected in their electron transport properties.

3.3.1 Barrier thickness distribution

First, we investigate the thickness distribution along the Josephson junction by direct measurements of the barrier thicknesses at different positions using transmission electron microscopy (TEM). Since the tunneling current through oxide barriers decreases exponentially with an increased barrier thickness, even small variations in thickness will render an inhomogeneity of the tunneling current across the barrier. Consequently, the conductance per unit area becomes substantially smaller as compared to the case if the barrier had been homogeneously thick. In fact, as we show in Appended paper V, less than 10% of the junction area dominates the electron tunneling.

Experiments

In this study, the unpatterned $Al/AlO_x/Al$ junctions were fabricated on Si/SiO_2 substrates using thermal resistive evaporation of Al-6N (purity 99.9999%). After the first evaporation step, the 15 nm-thick Al film was statically exposed to high-purity (99.99%) O_2, in different partial oxidation pressures (P_{ox}) and times (t_{ox}), see Table 3.3. After the oxidation process, a second layer with nominal thickness of 60 nm was deposited using the same evaporation parameters as for the first layer.

The specimens for the cross-section TEM were prepared by grinding and polishing them down to a thickness of $\approx 20\,\mu$m, followed by Ar-ion milling at an ambient temperature of $-80°$C (to minimize the sample damage due to the ions). For the high-resolution (≈ 1Å) imaging, an FEI Titan 80-300 TEM/scanning TEM (STEM) was used. In particular, Annular Dark Field STEM was used for the direct measurements of the junction thicknesses.

Sample	P_{ox} [mbar]	t_{ox} [min]	$\langle l \rangle$ [nm]	σ_l [nm]	$P_{90\%}$ [%]
1	0.1	3	1.66	0.35	7.3
2	0.1	30	1.88	0.32	9.2
3	1.0	3	1.73	0.37	6.9

Table 3.3: Oxidation parameters (oxidation pressure P_{ox} and time t_{ox}) and barrier thickness measurement results (average barrier thickness $\langle l \rangle$ and standard deviation σ_l), for the three investigated samples, each containing over 300 measurement positions.

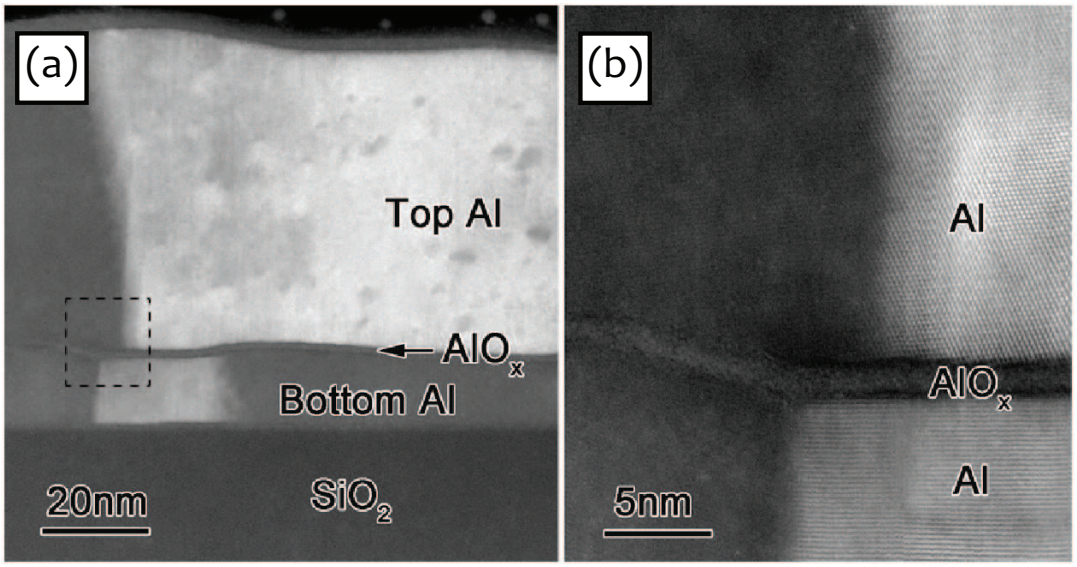

Figure 3.5: ADF STEM images of an Al/AlO$_x$/Al tunnel junction. **(a)** Cross-section overview of hte junctions layer structure, with the two Al electrodes, the barrier and the SiO_2 substrate. **(b)** A zoomed in images from the black dashed box in (a), showing the AlO$_x$ junction. Courtesy of Lunjie Zeng.

Results

In Fig. 3.5, a cross-sectional ADF STEM image shows an overview of sample 1, where the AlO$_x$ barrier is embedded between the two Al layers. The assessment of the barrier thickness is then done from the image intensity profiles, revealing the distance between the two layers of pure Al, with very high resolution. Here, the peaks in the profiles indicate the positions of the Al atomic planes. The thickness variation of the over 300 measured positions for each sample has Gaussian distributions, around mean values, $\langle l \rangle$, with standard deviations, σ_l, presented in Table 3.3.

The results for the three studied samples lead us to the conclusion that the oxidation time, t_{ox}, has a stronger impact on the barrier thickness as compared to the oxidation pressure, P_{ox}. From the obtained thickness distributions, we can study how large part of the junction area that actively contributes to its total conductance. If we model the junction as a potential barrier of height, ϕ, and thickness, l, its conductance per unit area (or specific conductance) can be expressed as [70]

$$\sigma(l) = A \times \exp[-l/\lambda], \tag{3.9}$$

where λ is the barrier attenuation length, defined as

$$\lambda = \hbar/(2\sqrt{2m\phi}) \tag{3.10}$$

and the coefficient A can be expressed as

$$A = \left[3 \times \sqrt{2m\phi}/2l\right] \times (e/h)^2 \tag{3.11}$$

with $m \approx 9.11 \times 10^{-31}$ kg being the electron mass and the barrier height is chosen to be ≈ 2 eV, which is typical for AlO$_x$ barriers [71–73], corresponding to a barrier attenuation length, $\lambda = 0.069$ nm. From the specific conductance in Eq. (3.9)

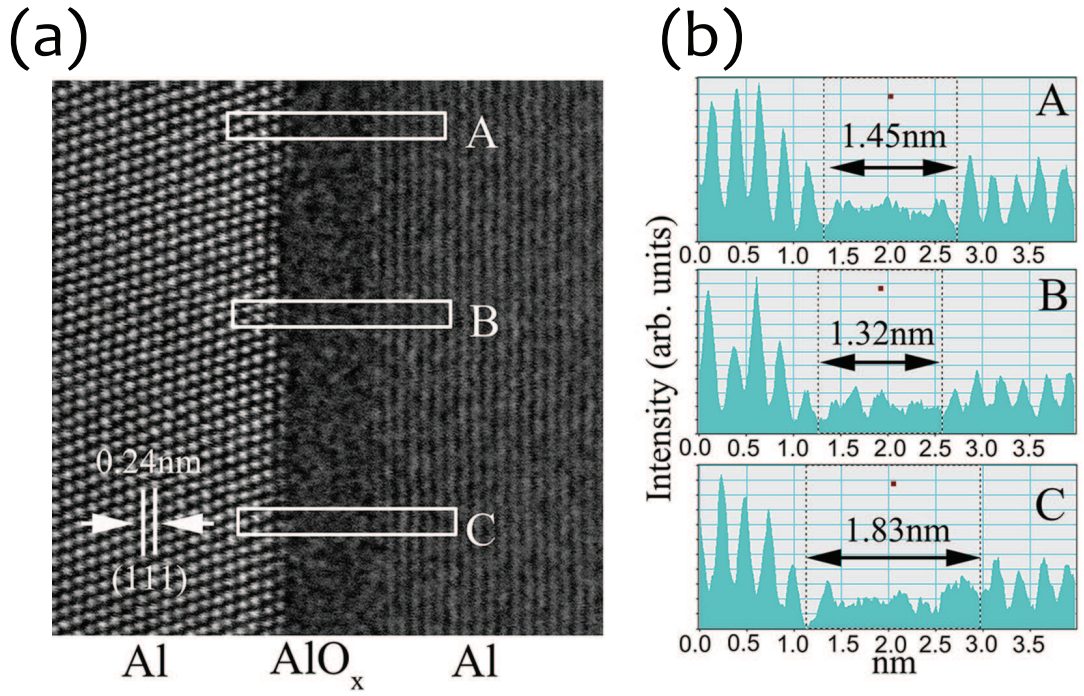

Figure 3.6: Measurement procedure from image intensity profiles of a junction in sample 3. **(a)** High-resolution ADF STEM image where the Al(1 1 1) atomic plane as well as the plane distance are indicated. The white windows labeled A, B, and C where used to measure the intensity profiles, shown in (b). Courtesy of Lunjie Zeng.

and the Gaussian distribution function for the junction thickness, $g(l)$, another distribution function can be expressed for the conductance in the tunnel junction

$$T(l) = \sigma(l) \times g(l) \tag{3.12}$$

Next, we investigate the proportion of the active area of the junction with a thickness thinner than l_x with respect to the whole barrier area by defining

$$P(l_x) = \int_{-\infty}^{l_x} T(l)dl / \int_{-\infty}^{+\infty} T(l)dl, \tag{3.13}$$

$$G(l_x) = \int_{-\infty}^{l_x} g(l_x)dl / \int_{-\infty}^{+\infty} g(l)dl. \tag{3.14}$$

The results are also shown in Table 1, indicating that 90 % of the tunnel current flows in less than 10 % of the junction area for all the measured samples. Moreover, the total junction conductance can be expressed by taking the full integral of the Gaussian distribution function, yielding

$$G(l, \sigma_l) = G_0 \exp[-l/\lambda] \exp[\sigma_l^2/(2\lambda^2)] \tag{3.15}$$

3.3.2 Atomic details of substrate-junction interface

In this section, we look at how electron energy loss spectroscopy (EELS) can be used to probe the distribution of different elements within a Josephson junction. In Appended paper VI, we study which elements are contained in the interface between an HF-etched Si substrate and a deposited Josephson junction electrode of Al.

Experiments

Similar to the sample preparation procedure described in the previous section 3.3.1, unpatterned samples were fabricated on Si substrates. Prior to the Al evaporation, the native oxide on top of the Si was wet etched 1 min in a bath containing 2% HF, leaving dangling bonds on the Si surface. After the etching, the samples were dipped in de-ionized water for 20 s and short thereafter pumped down in the load lock of the Plassys electron-beam evaporator, with the intention to prohibit new oxygen from sticking to the sample surface.

The cross-section TEM specimens were then prepared using the same polishing and Ar-ion milling techniques mentioned in the previous section 3.3.1. The high-resolution imaging, electron energy loss spectroscopy (EELS), and energy filtering transmission electron microscopy (EFTEM) were done using an FEI Titan 80-300 TEM/Scanning TEM (STEM) with a probe C_s corrector and a Gatan Imaging Filter (GIF) Tridium.

Results

From the high-resolution imaging, we can clearly see that there is an interfacial layer of about 5 nm between the bottom Al electrode and the Si substrate. The element distribution of the layers is shown in Fig. 3.7, where the EFTEM images are shown for the cases when probing Al L-edge (a), O K-edge (b), and Si L-edge (c). In Fig. 3.7(d), the image intensities are plotted as a function of distance around the interfacial layer, indicating that this layer consists of an intermixing between the Al, Si, and O.

Next, a more detailed study of this interface was done using spatially resolved STEM-EELS (in particular, energy loss near edge structure (ELNES)). Fig. 3.8(a) shows the EEL spectra acquired in the energy loss range between $\approx 70 - 130$ eV, at the interface positions shown in Fig. 3.8(b), where the background of each spectrum was removed using a power-law model. The size of the electron probe used for these spectra was estimated to be around 0.13 nm. The spectra in Fig. 3.8(a) show several indicated peaks and can be divided into two regions (marked I and II), corresponding to the characteristics of the distributions of elements Al, Si, and O. From the ELNES spectra we find further details on which reactions are more favorable, see Appended paper VI for details.

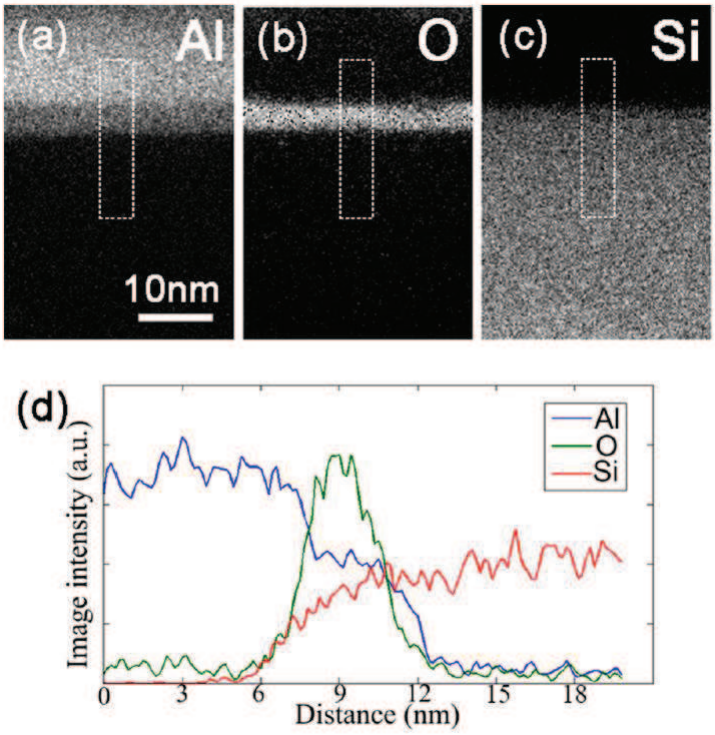

Figure 3.7: EFTEM images acquired with **(a)** Al L-edge, **(b)** O K-edge, and **(c)** Si L-edge at the region around the Al/Si interface. **(d)** Corresponding image intensity profiles of the mapped elements Al, O, and Si across the junction/substrate interface, measured within the dashed white regions in (a)-(c). Courtesy of Lunjie Zeng.

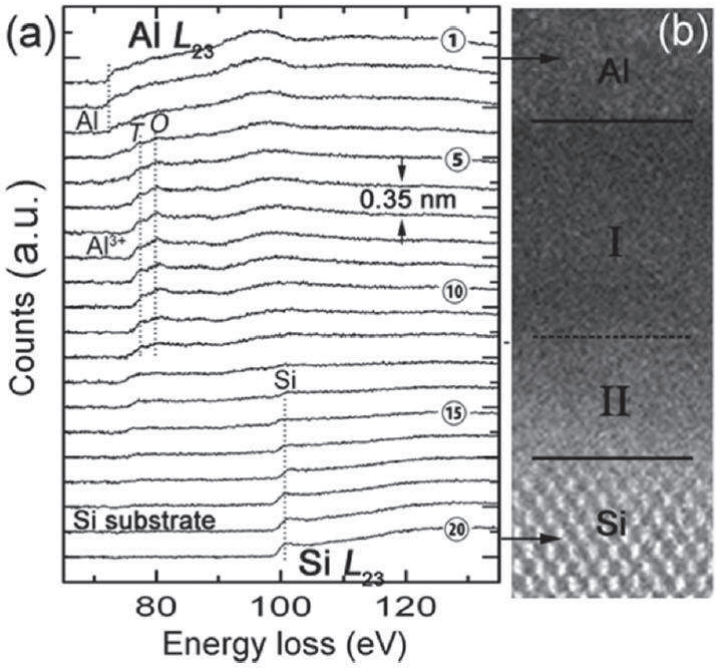

Figure 3.8: **(a)** STEM-EELS spectra acquires across the Al/Si interface, with step size of ≈ 0.35 nm between two adjacent spectra. The dashed lines indicate the positions of different edges and peaks. **(b)** STEM ADF image of the area from where the EELS spectra were taken. The black arrows indicate spectrum 1 and 20. Courtesy of Lunjie Zeng.

3.4 Cryogenic measurements

Measurements involving superconducting devices rely on our ability to create a low-noise environment for the samples by cooling them far below the critical temperature of the superconducting materials, $T \ll T_c$. Therefore, we perform the measurements in a ^{4}He/^{3}He cryogen-free dilution refrigerator with a base temperature of 7 mK.

The cooling mechanism is based on a phase separation that occurs when a mixture of ^{4}He and ^{3}He is cooled down to low temperatures (T<0.86 K), giving rise to two phases of ^{3}He with different concentration. Since this isotope is the lighter one of the two, a ^{3}He rich phase (concentrated phase) accumulates on top of the ^{4}He-rich phase (diluted phase). The cooling takes place when the ^{3}He is transported from the concentrated phase to the diluted phase through a phase boundary. This process takes place inside the mixing chamber (M/C) and is the coolest part of the cryostat. However, before this cooling effect can happen, we need to be able to condense the helium mixture, which can be done in a few different ways depending on the type of cryostat. The measurements contained in this thesis were done in two different BlueFors cryogen-free cryostats; one at Chalmers and one in Queensland, Australia. These cryostats do not need a bath of liquid He to pre-cool. Instead, a compressor is used to drive a pulse tube, transferring He gas back and forth inside the core of the cryostat, cooling the system down to about 3 K. For details on how this type of cryostat operates, the reader is referred to literature such as [74].

3.4.1 Measurement setup

Prior to the cryogenic characterization, the samples were mounted and wire-bonded to a home-made sample box, see Appendix D for details. The box consists of four parts, each computer numerical control (CNC) milled out from oxygen-free copper. In order to improve thermal anchoring as well as electrical conductivity, a few micron of gold was electroplated on each part, see Appendix A.3 for recipe. Next, the box is connectorized with SMA connectors and fed through the box walls using glass beads. Inside the box, microstrip launchers are threaded onto the glass beads and soldered on the center conductor of a printed circuit board (PCB) made from Rogers RO3010 with an effective dielectric constant of $\epsilon_r \approx 10$, matching the dielectric constant of silicon and sapphire at cryogenic temperatures. The sample is glued into a milled hole in the PCB to get thermal anchoring from the box on the backside and align the edge of the sample with the top of the circuit board. The sample is then bonded to the PCB using gold wire of diameter 25 μm. It is important to fit as many bonds as possible in order to improve the microwave transmission and to reduce the spurious inductance from the wires. The device is then mounted on the M/C tail of the cryostat.

To characterize the samples, a microwave setup was installed in the cryostat, see Fig. 3.9. Several aspects need to be taken into account when wiring up the cryostat. First, due to the limited cooling power of the fridge, the cables and components need to be well thermally anchored at each temperature stage not to heat up the system. The coaxial cables are therefore chosen to have poor thermal conductivity between the higher temperature stages while still not attenuating very much, see Figs. 3.9 and 3.10. At the lower temperatures, however, superconducting coax-lines are used with the properties of very low attenuation but still with poor thermal

conductivity. Since the cryostat cooling power is very different at the various stages, attenuators are attached to the lines, thermalizing their inner conductors. The amount of attenuation is chosen such that the resulting noise temperature matches the stage at which it is mounted.

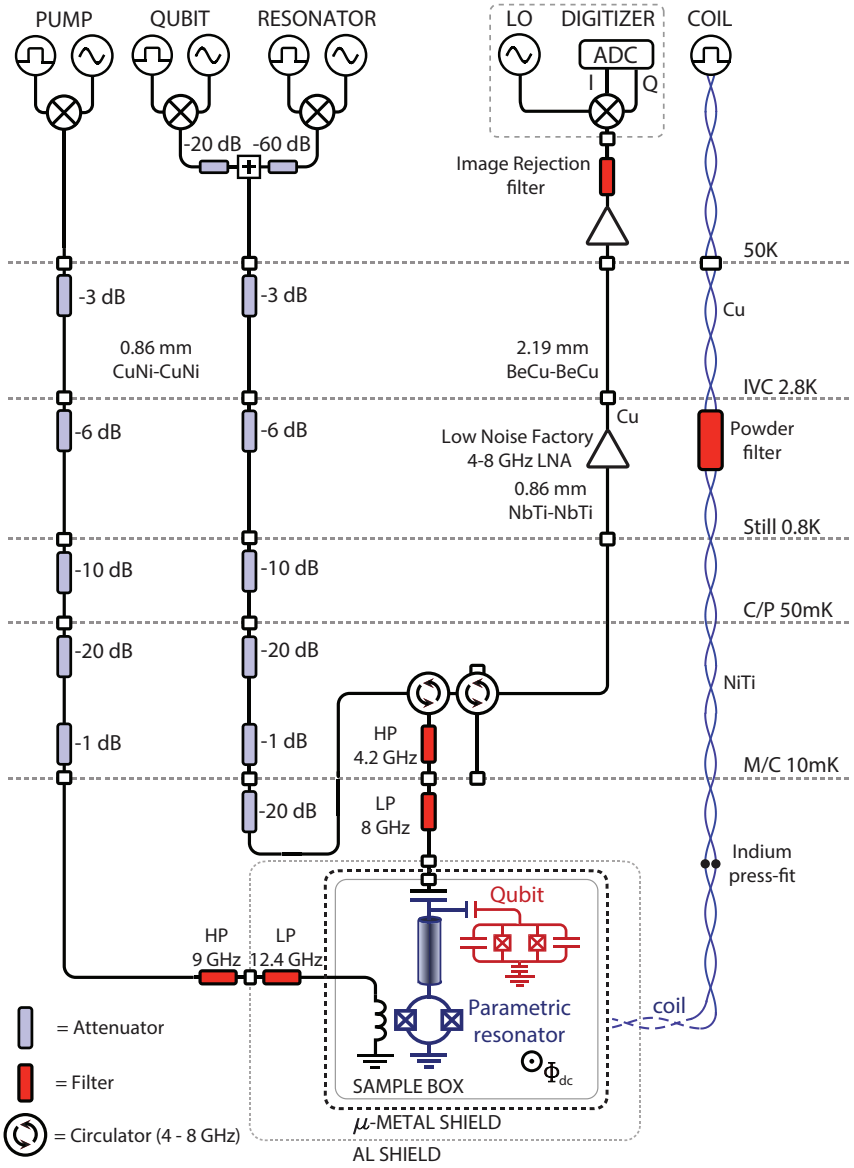

Figure 3.9: Schematic of the cryogenic microwave setup used in the BlueFors cryostat "Lumi" at Chalmers. The pulsed microwave signals are shaped using an arbitrary waveform generator (AWG), and attenuated at all temperature stages. The reflected signal is filtered in a band chosen to prohibit the pump signal from leaking through. After passing the two circulators, the signal is amplified, first using a low noise amplifier and then at room temperature. The signal is sampled and downconverted using a PXI Digitizer.

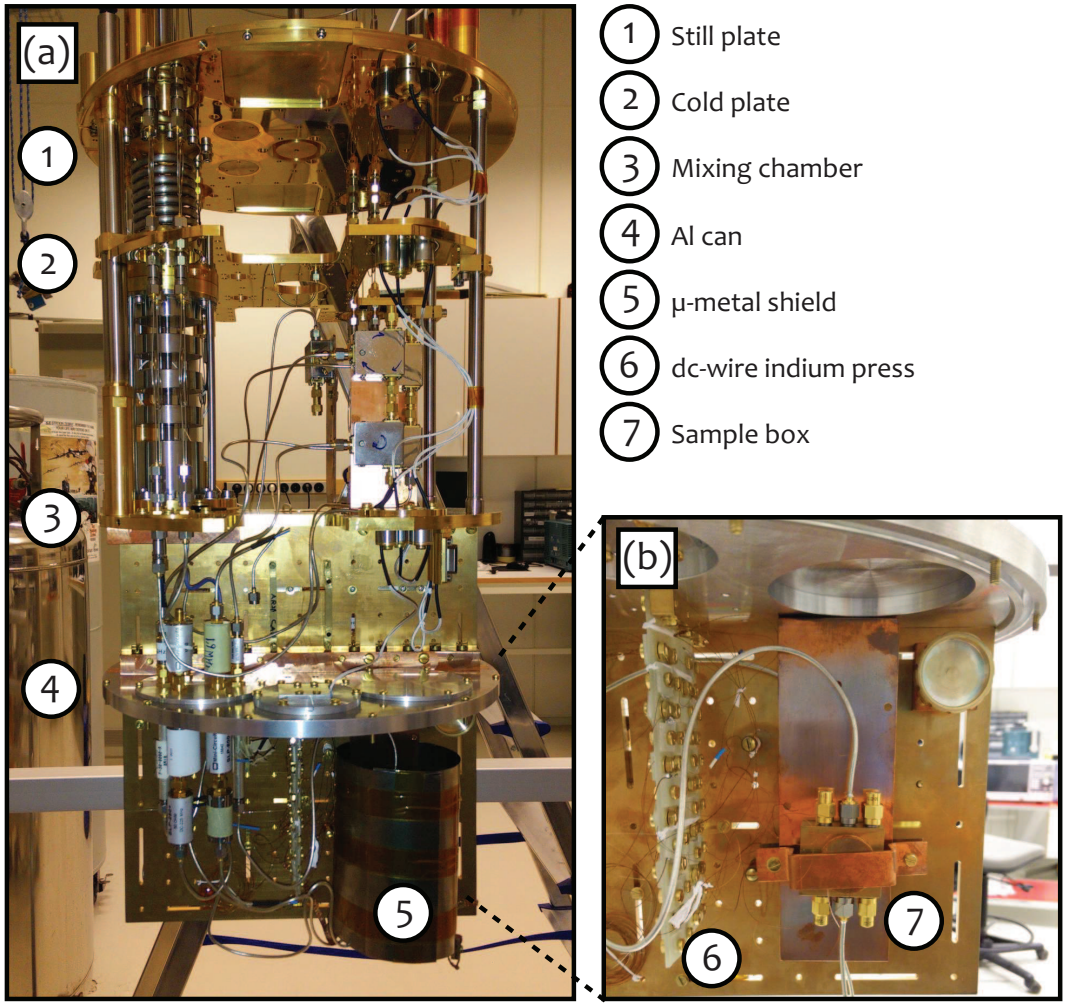

Figure 3.10: Cryostat wiring in the BlueFors cryostat "Lumi" at Chalmers. **(a)** The three lowest temperature stages of the cryostat, containing the setup used to do the JPO readout experiments. **(b)** Zoom in on the sample box, thermally anchored to the mixing chamber.

Chapter 4

4 Results

In this chapter, the experimental characterization sequence of the Josephson parametric oscillator (JPO) is presented. The section is structured as follows: First, we show how the two dominant nonlinearities, the Duffing nonlinearity and the pump-induced nonlinearity, are extracted and predicted. The details of this study are presented in Appended paper I. Second, we connect a transmon qubit to the JPO and utilize the dispersive qubit–resonator coupling as well as the strong oscillation response of the JPO to build a high-fidelity, single-shot readout. The details of the readout can be found in Appended paper II.

4.1 Static characterization

In this section, an external superconducting magnetic coil is used to apply dc-magnetic flux through the SQUID loop of the resonator. This allows us to tune the resonant frequency of the device by changing its Josephson inductance and thus its electrical length.

4.1.1 Frequency tuning curvature

The first important step when characterizing the parametric resonator is to measure the resonant frequency and its dependence on the static dc-flux bias, $F = \pi\Phi_{\mathrm{dc}}/\Phi_0$, using a vector network analyzer. However, since the device exhibits the behavior of a Duffing oscillator, the line shape of the resonator magnitude response (as well as its resonant frequency) is dependent on the resonator photon number, $|A|^2$. This effect is more pronounced when the critical current of the Josephson junctions is suppressed, *i.e.* when the resonator frequency is far detuned away from its maximum value, for $F \to \pm\pi/2$. In Fig. 4.1(a), the Duffing response is shown and we can find a power level below which the linewidth is more linear showing a Lorentzian response, see section 2.4.3. This is important when extracting quality factors and damping rates, since Eq. (2.5) only is valid for a Lorentzian line shape.

After identifying a power level below which the resonator exhibits linear response, we continue by extracting the inductive participation ratio, γ_0, yielding how large

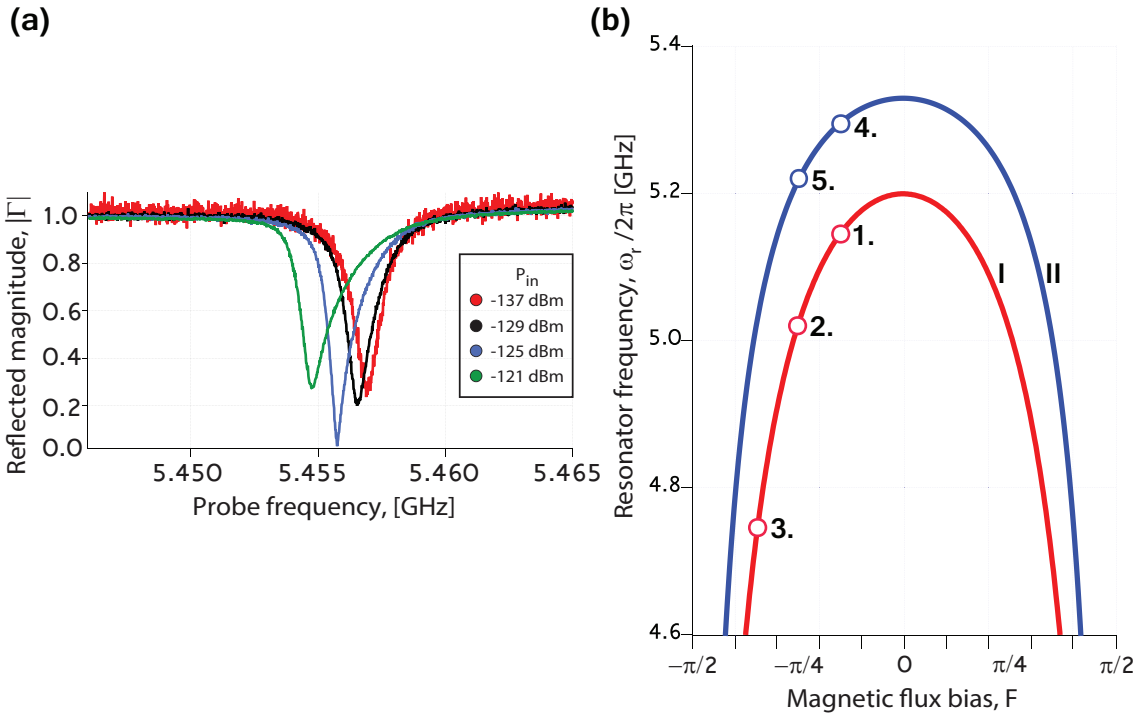

Figure 4.1: **(a)** The reflected magnitude response for incrementally increase of the probe power for a sample with a more pronounced Duffing nonlinearity. **(b)** Extracted resonant frequencies for the two devices I and II, listed in Table 4.1, fitted to Eq. (4.1), with different inductive participation ratios, γ_0, yielding slightly different frequency-flux curvatures.

the Josephson inductance is as compared to that of the resonator. This is done by sweeping the magnetic flux, F, and measuring the magnitude and phase of the reflection coefficient, S_{11}. In Fig. 4.1(b), the resonant frequencies for two devices, with slightly different participation ratios, are extracted for each point in flux and fitted to the function in Eq.(2.8) we recall from section 2.1.2

$$\omega_r(F) \approx \frac{\omega_{\lambda/4}}{1 + \gamma_0 / \left|\cos(F)\right|}. \tag{4.1}$$

In addition to the participation ratio, we can also extract the bare resonator frequencies, $\omega_{\lambda/4}$, revealing what the resonant frequency would have been in absence of the inductance contribution from the SQUID. The extracted parameters for these two devices are presented in Table 4.1.

Sample	$\omega_{\lambda/4}/2\pi$ [GHz]	$\omega_r(0)/2\pi$ [GHz]	γ_0[%]	I_c [μA]
I (Paper I)	5.645	5.200	8.98	2.18
II (Paper I)	5.626	5.344	5.63	3.48
III (Paper II)	5.550	5.271	5.30	3.14

Table 4.1: Extracted resonator parameters for the two measured samples, with $\omega_{\lambda/4}$ and $\omega_r(0)$ denoting the bare and zero-flux resonant frequencies, respectively. The inductive participation ratios and critical currents are denoted γ_0 and I_c, respectively.

4.1.2 Duffing nonlinearity

After extracting the participation ratio from the frequency tunability, we investigate the effective Duffing parameter, α which depends both on γ_0 and on the magnetic flux bias recalling Eq. (2.47)

$$\alpha \approx \alpha_0 \left(\frac{\gamma_0}{\cos(F)} \right)^3, \tag{4.2}$$

with $\alpha_0 = \pi^2 \omega_{\lambda/4} Z_0 / R_K$ and $R_K = h/e^2$ being the quantum resistance. We can extract the Duffing parameter by measuring the frequency shift of the resonator by probing it with incrementally increased powers at a fixed bias point, see Appended paper I, but far below the instability threshold at which the system bifurcates [75, 76]. The resonance then undergoes a nonlinear frequency shift from $\delta\omega|_{A=0} = 0$ to $\delta\omega|_{A\neq 0} = -\alpha|A|^2$, where $|A|^2$ is the number of photons in the resonator and α represents the frequency shift per photon. This nonlinear shift can be expressed in terms of the probe power $|B|^2$ (in units of photons per second) and the resonator damping rates,

$$\delta\omega = -\frac{2\alpha\Gamma_0}{\Gamma^2}|B|^2. \tag{4.3}$$

We extract the Duffing parameter α using Eq. (4.3) at five different bias points for sample III, listed in Table 4.2. In Fig. 4.2(a), the resonant frequency is plotted as a function of the probe power. The five considered flux bias points are indicated in Fig. 4.2(b). Note that the Duffing shift is more pronounced as we move down on the tuning curve.

4.1.3 Calibration of the resonator photon number

In this section, we study how the Duffing nonlinearity of the resonator can be utilized as a probe of the intra-resonator field, allowing us to calibrate the photon number, $|A|^2$, by extracting the attenuation of our probe line as well as the net gain of our amplifier chain. The Duffing-shifted resonant frequency as a function of input probe power takes the following form,

$$\omega_r(P_s) = \omega_r(0) - \frac{2\alpha\Gamma_0}{\Gamma^2} \frac{10^{(P_s - Att - 30)/10}}{\hbar\omega_r(0)}, \tag{4.4}$$

where $\omega_r(0)$ denotes the resonant frequency with zero photons in the resonator, Γ_0 and Γ are the external and total damping rates, respectively, and α is the Duffing frequency shift per photon, recall Eq. (4.2). Using Eq. (4.4), we can fit the extracted resonant frequencies as a function of input probe power at different flux bias points F, with the attenuation, Att, as the only fitting parameter (since α can be extracted separately by fitting $\omega_{\lambda/4}$ and γ_0, recall Eq. (4.1)). This is shown for sample III in Fig. 4.2(a), where the data for five different flux bias points are fitted to attenuations presented in Table 4.2. From these, we obtain an average attenuation $\langle Att \rangle = 127.5\,\text{dB}$, which can be compared with the installed 120 dB, indicating that we have an additional cable loss of 7.5 dB at the measurement frequency.

Moreover, from the same measurement we can also obtain an estimate for the

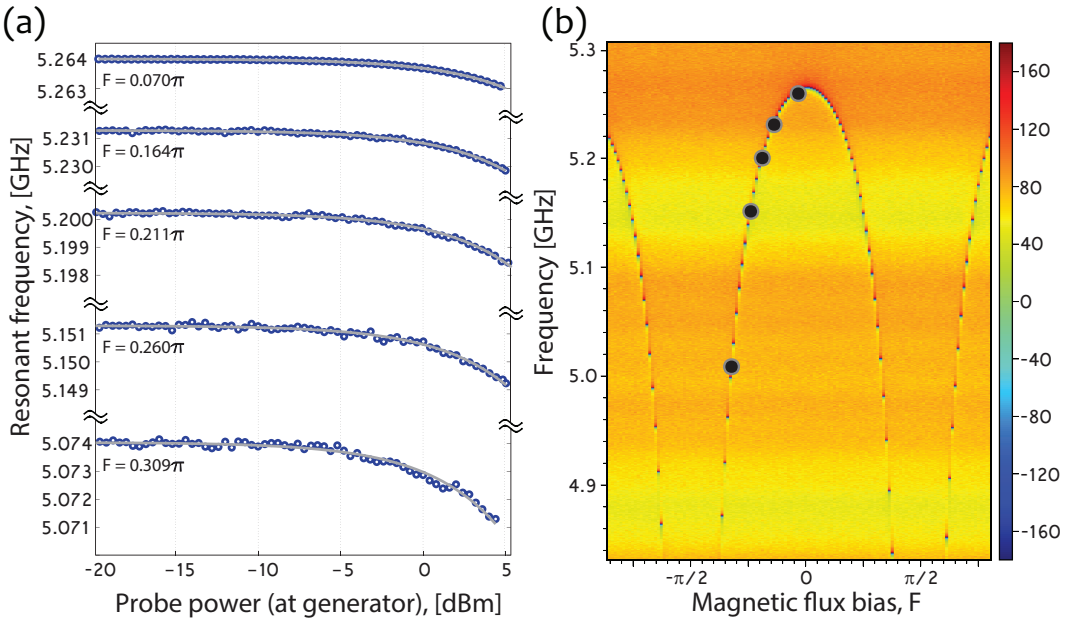

Figure 4.2: **(a)** Extraction of the non-linear Duffing frequency shift as a function of probe power, for five different flux bias points. The grey solid lines are fits to Eq. (4.4), indicating an increased shift as the resonant frequency moves further down on the tuning curve. For every point, we fit the attenuation of the input line, *Att*, see Table 4.2. **(b)** The frequency tuning curve in which the five bias points used in (a) are indicated.

gain of the amplifier chain by assuming that all the signal gets reflected when it is far off resonance with the resonator. Then, the gain is obtained from the relation

$$G = |S_{11}|^2 + Att, \tag{4.5}$$

where S_{11} is the measured reflection coefficient when far detuned. For the five gain estimates presented in Table 4.2, we obtain a fitted gain of $G = 81.0 \pm 0.17$ dB[1], at our given bias point, which can be compared with our 91 dB of installed amplification. We attribute this discrepancy to cable and interconnect losses along the amplifier line.

dc-flux bias	F/π	0.070	0.164	0.211	0.260	0.309	
Attenuation	*Att*	-126.9	-127.1	-127.5	-127.8	-127.9	dB
Gain	*G*	80.3	80.6	81.4	81.4	82.0	dB

Table 4.2: Extracted attenuation for the five different dc-flux bias points used for fitting the Duffing nonlinearity from Eq.(4.4), see Fig. 4.2. The corresponding gain values were obtained from Eq. (4.5).

Next, the obtained calibration of the amplifier chain gain, G, can now be used to calculate the conversion factor between our measured power on the digitizer and the number of photons in the resonator, using the following relation,

[1]The error bar for the gain value originates from the uncertainty of the linear fit. However, by also taking into account gain drift over time another ±0.2 dB should be added to this error.

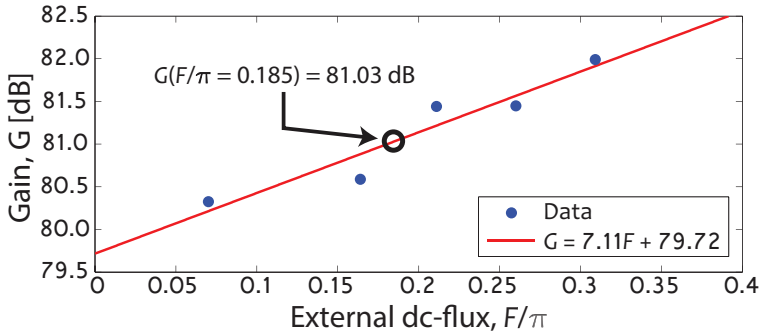

Figure 4.3: Extracted values for the net gain of the amplifier chain plotted as a function of the magnetic flux bias point, extracted using Eq. (4.5). The data points are fitted to a linear function, allowing us to infer a gain for the particular flux bias point used throughout the readout demonstration.

$$|A|^2 = \frac{P_s - P_n}{2(\Gamma_0/2\pi)\hbar\omega_r^{|0\rangle}10^{G/10}}, \tag{4.6}$$

where P_s and P_n denote our signal and noise power levels, respectively. We demonstrate this for the bottom panel of Fig. 4.8, where the resonator is probed at a frequency $\omega_r^{|0\rangle}/2\pi = 5.212\,\mathrm{GHz}$. The external damping rate is $\Gamma_0/2\pi = 1.02\,\mathrm{MHz}$, and we calculate the background power level from the end of the trace (when the pump is off). From the obtained SNR, the number of added noise photons can be estimated accordingly, $|A|^2/\mathrm{SNR}^2 = 16.1 \pm 1.3$, which corresponds to a system noise temperature of $4.03 \pm 0.33\,\mathrm{K}$.

4.2 Parametric characterization

Eventhough the static characterization allows us to extract important system parameters, the core physics which is exploited in this thesis is based on modulating (or pumping) the boundary condition and thus the frequency of our resonator at close to twice its resonant frequency. Such a modulation (at strong enough amplitude) gives rise to parameteric oscillations. In this section, we present how the parametric oscillation properties of the device are studied and analyzed.

4.2.1 Pump-induced nonlinearity

Apart from the Duffing non-linearity, a second nonlinear effect we study enters the dynamics when the parametric pumping is turned on and gets sufficiently strong for higher order terms of the mixing product expansion to affect the resonator [22, 65]. To investigate this nonlinearity, we minimize the Duffing nonlinearity by turning off the probe signal. We then parametrically pump the flux degenerate around a bias point a bit higher up on the flux curve where the Duffing influence is weaker, see Fig. 4.2. As we recall from Eq. (2.36), the first higher-order term is proportional to the square of the pump strength and has the effect of shifting the resonator down in frequency as a consequence of rectification in the flux−frequency transfer function. As with the Duffing parameter, the pump-induced nonlinearity parameter can be expressed in terms of γ_0 and F as

$$\beta = \frac{\beta_0}{\gamma_0}\frac{\cos^3(F)}{\sin^2(F)}, \tag{4.7}$$

with $\beta_0 = \Gamma/\omega_{\lambda/4}$. We reveal this effect by detecting the region of parametric instability in the parameter-plane spanned by the pump−resonator detuning δ' and the effective pump strength ϵ', see Fig. 4.4. The energy of the field inside the resonator originates from the pump, and starts to build up exponentially in time when ϵ' is sufficiently strong to compensate for the total damping rate of the resonator: $\epsilon' > \Gamma$. After pumping for some time, the field saturates to a steady state set by the Duffing nonlinearity at the given point in the $(\delta' - \epsilon')$-plane, which we expect to shift the resonator frequency out from the degenerate parametric pumping condition, $\omega_p \approx 2\omega_r$. The boundaries represent the bifurcation threshold at which the resonator enters into the parametric bistable regime, where oscillations in one of two metastable states of the system Hamiltonian occur [37]. In Fig. 4.4, the theoretical prediction from Eq. (2.43) is compared with the experimental observation of the parametric region.

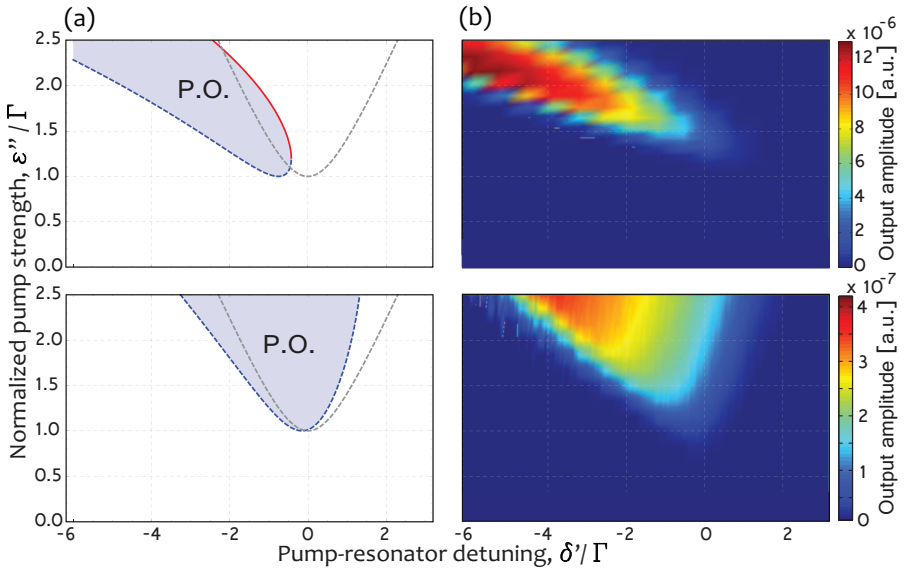

Figure 4.4: (a) Theoretical parametric-oscillation region (P.O.) in the $(\delta' - \epsilon')$-plane. The dashed blue and solid red lines are the two solutions to Eq. (2.43), whereas the dashed gray line indicates the symmetric region in Eq. (2.35), in the absence of a pump-induced frequency shift β. The two filled theoretical regions are plotted for $\beta_0/\gamma_0 = 0.22$. The top and bottom traces are plotted for magnetic flux bias points $F_4 = -0.15\pi$ and $F_5 = -0.25\pi$, respectively. **(b)** Measured amplitude response around half of the pump frequency at the same bias points as the theoretical curves $F_4 = -0.15\pi$ (top) and $F_5 = -0.25\pi$ (bottom) for sample II, see Fig. 4.1(b). The facets of the data are interpolated to guide the eye.

4.2.2 Flux dependence of nonlinearities

After studying the Duffing and pump-induced nonlinearities, there are some important connections to make between these nonlinear effects, magnetic flux bias, and participation ratio, γ_0. In Fig. 4.5(b), the magnetic flux dependence of the two aforementioned nonlinearities is plotted for three different values of γ_0. From the plot, it is clear that the two nonlinear effects contribute differently at different flux bias regimes. When the resonant frequency is close to its maximum, $(F \to 0)$, the Duffing nonlinearity is suppressed, whereas the pump-induced nonlinearity dominates. On the other hand, when the resonator is far detuned from the top, $(F \to \pm\pi/2)$, the pump-induced nonlinearity is suppressed and the Duffing nonlinearity dominates.

Both these nonlinearities contributes to saturating the amplitude of parametric oscillations in the resonator. Therefore, it is important to keep these two effects in mind when chosing flux bias point.

4.2.3 Finding the parametric instability threshold

In this section, a method for calibrating the parametric instability threshold is presented. It is hard to experimentally find the parametric oscillation threshold with good precision, when only considering the parametric oscillation region, whose observed shape gets smeared out by the amplified vacuum noise. Instead, an alternative method is to use a weak probe signal, and we thus probe the parametrically amplified response as we sweep the pump amplitude across the instability threshold.

We probe at the resonant frequency of the resonator $(\omega_s = \omega_r)$, while applying a

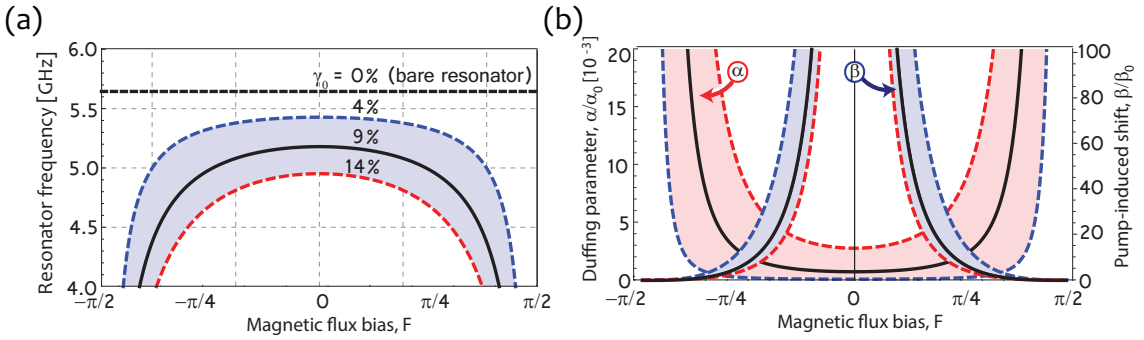

Figure 4.5: **(a)** The resonator frequency as a function of magnetic flux from Eq. (4.1) for a bare non-tunable resonator ($\gamma_0 = 0$) (black dashed line) and three values of the inductive participation ratio $\gamma_0 = 0.040$, 0.090, and 0.14, in dashed blue, solid black, and dashed red, respectively. **(b)** Magnetic-flux dependence of the normalized Duffing nonlinearity parameter, α/α_0 from Eq. (4.2) (left axis) and pump-induced frequency shift parameter, β/β_0 from Eq. (4.7) (right axis), shown in red and blue regions, respectively. The three different traces correspond to the same values of γ_0 as in (a).

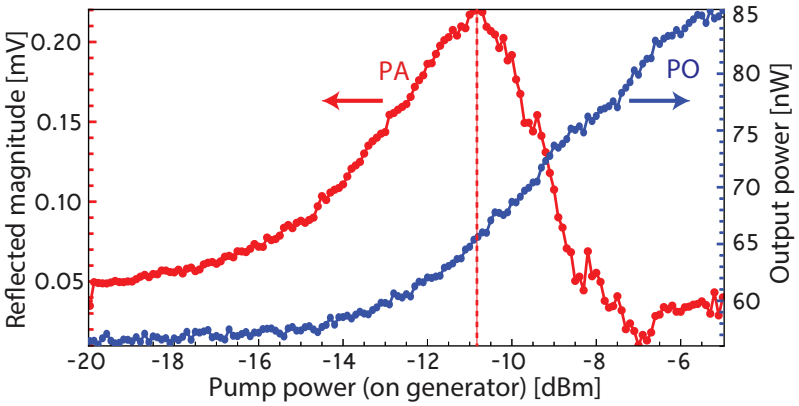

Figure 4.6: Reflected magnitude of non-degenerate parametric amplification (PA, red trace and left y-axis) and power of parametric oscillations (PO, blue trace and right y-axis) as a function of pump power across the instability threshold (dashed line).

slightly detuned pump signal, such that $(\omega_p - 2\omega_s)/2\pi = 100\,\text{kHz}$. The signal then undergoes phase-preserving parametric amplification (red trace in Fig. 4.6), while the parametric oscillations are cancelled out since we measure the average amplitude of the field. The parametric amplification has maximum efficiency just at the threshold. In Fig. 4.6, we plot the magnitude of the reflected signal as a function of the pump power (at the generator), yielding an oscillation threshold $P_{\text{th}} = -10.8\,\text{dBm}$, as indicated by the dashed red line. As a comparison, another measurement was performed to instead probe the parametric oscillations (PO), where we measured the output power without the probe signal ($B(t) = 0$) and with zero pump-resonator detuning, such that $(\omega_p - 2\omega_r)/2\pi = 0$ — see blue trace and right y-axis in Fig. 4.6.

4.3 The Josephson parametric oscillator readout

In this section, the reader is introduced to the results presented in Paper II. In this work, we demonstrate a single-shot readout technique based on coupling a superconducting qubit to the parametric oscillator, recall section 2.5.2. The readout contrast offered by our technique relies on two phenomena; the qubit state dependent dispersive frequency shift that a qubit exerts on the resonator (see Fig. 4.4 and section 2.4.3) and the fact that parametric oscillations only occur within a confined frequency span (see section 2.2.2). Thus, as a consequence of exciting the qubit, the pump condition needed for the oscillations is modified. This allows us to encode the state of the qubit into two distinct oscillation amplitudes: one quiet state with zero photons in the resonator and one populated state. As we will see in this section, the strong nature of the parametric oscillations allows us to distinguish the state of the qubit in a single-shot measurement, with a state-discrimination of 81.5 %. From an error budget, we can infer a readout fidelity of 98.7 %.

4.3.1 Device characterization

Magnetic flux sweep: oscillator and transmon spectroscopy

The starting point of the device characterization is to sweep the magnetic flux and spectroscopically probe the transmon transition frequency, using regular dispersive readout of the resonator, see section 2.4.3. However, since the same superconducting coil is used to generate the static magnetic flux for both the resonator and the transmon, a batch measurement is performed in order to track the resonator frequency for every magnetic flux bias point[2].

Starting with the qubit characterization, we first extract the qubit−resonator coupling rate, $g_{01}/2\pi = 46\,\mathrm{MHz}$, from the minimum frequency separation of the vacuum-Rabi splitting, see Fig. 4.7(a).

Next, we extract the charging energy, $E_C/2\pi = 453\,\mathrm{MHz}$, by studying the dependence of the dispersive frequency shift as a function of the qubit-resonator detuning, Δ, as we excite the transmon to a mixed state by applying a continous signal at the qubit transition frequency. This gives us two resonator peaks separated by 2χ, see inset in Fig. 4.7(b). By then using our knowledge about the coupling rate, g_{01}, the data can be fitted to the relation [39],

$$\chi(\Delta) = \frac{g_{01}^2}{\Delta}\left(\frac{E_C}{\Delta - E_C}\right), \tag{4.8}$$

with the charging energy, E_C, as the only fitting parameter, see Fig. 4.7(b).

Finally, the Josephson energy, E_J, is extracted by fitting the transmon spectrum, well approximated by Eq. (3.6), keeping E_J as the only fitting parameter. For the sample presented in Appended paper II, the Josephson energy was $E_J = 9.82\,\mathrm{GHz}$.

[2]The batch consists of three steps: ① Find the resonator in a coarse sweep. ② Make a fine sweep around the minimum magnitude value of step 1. Fit the obtained magnitude response to a Lorenzian, finding the exact resonant frequency. ③ Lock the resonator probe on resonance and sweep the qubit probe.

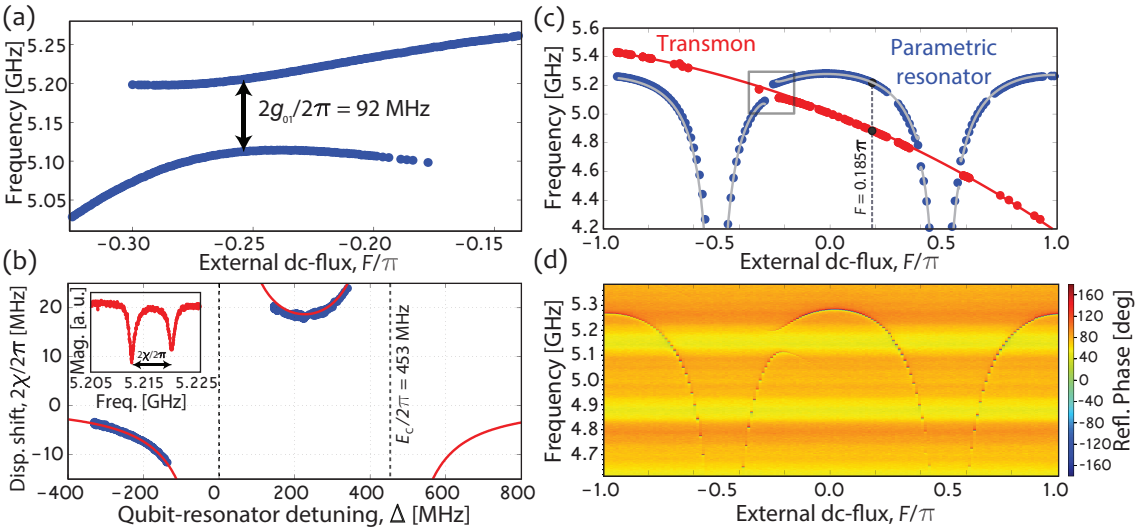

Figure 4.7: **(a)** Vacuum-Rabi splitting around the flux-bias point where the transmon frequency crosses that of the resonator. The minimum frequency splitting yields a qubit-resonator coupling $g_{01}/2\pi = 46\,\text{MHz}$. **(b)** Dispersive frequency shift, $2\chi/2\pi$, extracted as a function of the qubit−resonator detuning, Δ, fitted to Eq. (4.8). The two dashed lines indicate two asymptotes, located at $\Delta = 0$ and $\Delta = E_C$. From the fit, we extract a transmon charging energy of $E_C/2\pi = 453\,\text{MHz}$. **Inset:** The dispersive shifts for every magnetic flux bias point are extracted from the peak separation between the two resonator peaks, when continously probing the qubit. **(c)** Combined frequency spectrum obtained from qubit spectroscopy of the transmon qubit (in red) and through standard reflectometry for the resonator (in blue). The solid red and grey lines are fits. The dashed grey line, at resonator flux bias $F = 0.185\pi$, indicates the bias point at which we later demonstrate the readout method. **(d)** Raw data of the reflected phase from which the extracted resonator frequency in (c).

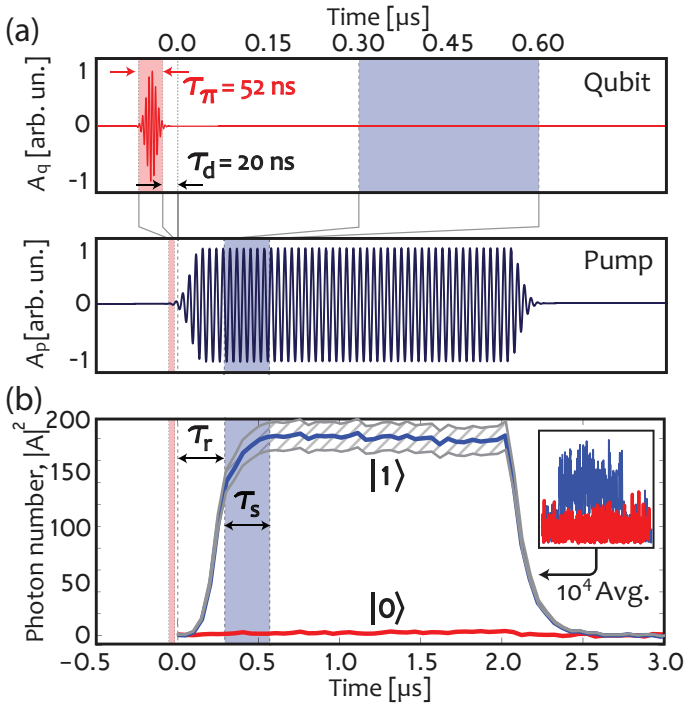

Figure 4.8: Qubit readout by the Josephson parametric oscillator. **(a)** Pulse sequence: The qubit π-pulse (in red), with Gaussian edges and a plateau of duration $\tau_\pi = 52\,\text{ns}$, is followed by a short delay, $\tau_d = 20\,\text{ns}$, before the pump is turned on at time $t = 0$. **(b)** The solid blue and red traces show the inferred photon number, $|A|^2$, in the resonator, with and without a prior π-pulse on the qubit, respectively. The traces are the result of 10^4 averages of the raw data; the inset shows a single instance of the raw data on the same time axis as the main plot. Prior to the sampling window of width $\tau_s = 300\,\text{ns}$, a delay $\tau_r = 300\,\text{ns}$ is added to avoid recording the transient oscillator response during the rise time of the oscillations. The two solid grey borders around the average photon number represent our uncertainty, originating from the amplifier gain calibration.

Parametric oscillation response and qubit state encoding

To demonstrate the parametric oscillation qubit readout, we choose the flux bias point $F = 0.185\pi$, indicated with the dashed gray line in Fig. 4.7(c). At this bias point, the resonator and qubit frequencies are $\omega_r^{|0\rangle}/2\pi = 5.218\,\text{GHz}$ and $\omega_a/2\pi = 4.885\,\text{GHz}$, respectively, yielding a qubit−resonator detuning of $\Delta/2\pi = -334\,\text{MHz}$ and an effective dispersive shift of $2\chi/2\pi = -7.258\,\text{MHz}$. We measure a Purcell-limited qubit relaxation time $T_1 = 4.24\,\mu\text{s}$ and Ramsey decay time $T_2^* = 1.66\,\mu\text{s}$, see section 2.4.4.

Once the magnetic flux bias point has been established, the high-fidelity readout must be able to map the ground and excited states of the qubit onto different states of the parametric oscillator. In our present device, we obtain maximum readout contrast if we encode the ground state $|0\rangle$ in the "quiet" state (empty resonator) and the excited state $|1\rangle$ in the "populated" state of the resonator. The pulse sequence, illustrated in Fig. 4.8(a), consists of a qubit manipulation pulse (in red), followed by a pump-pulse (in blue). Fig. 4.8(b) shows the resulting output from the JPO, when operated with the pump settings $[\delta^{|0\rangle}/\Gamma = -5.34, \epsilon/\Gamma = 3.56]$, yielding a photon number of $|A|^2 = 185 \pm 15$ obtained using the calibration protocol presented in section 4.1.3.

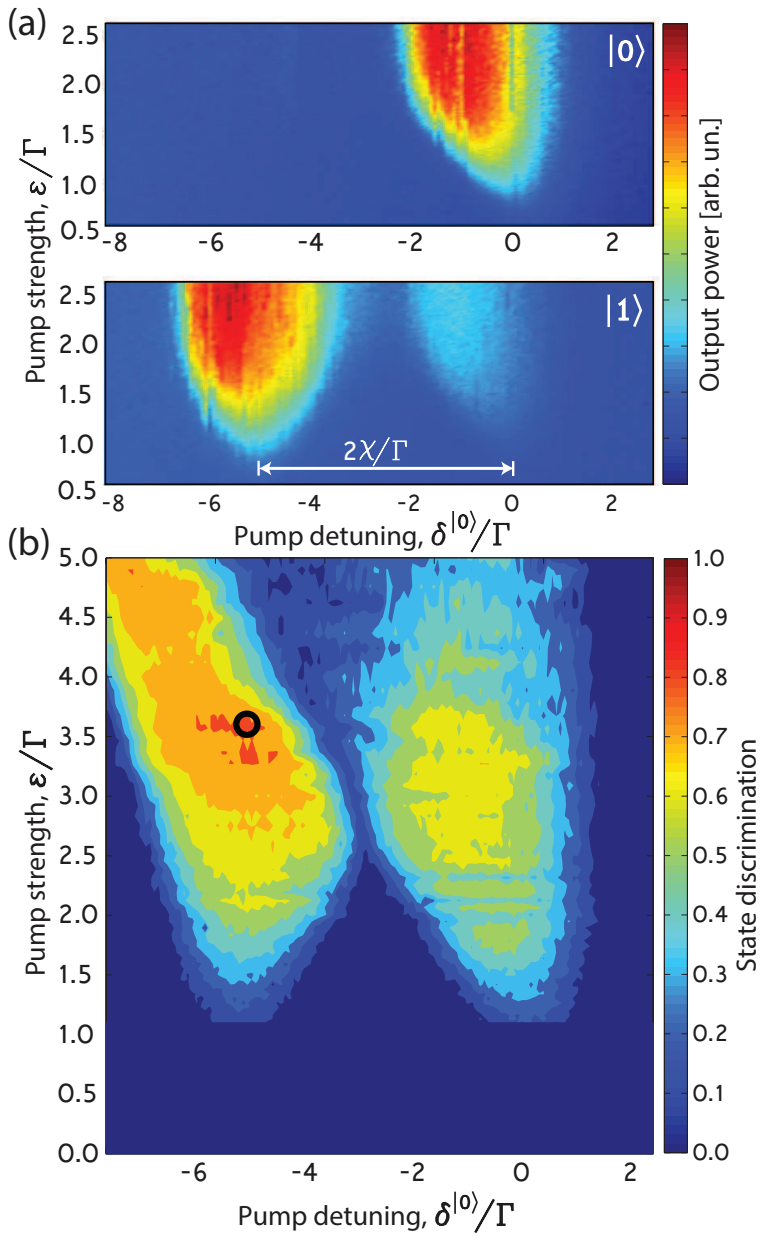

Figure 4.9: Parametric oscillations, and state discrimination. **(a)** Output field of the resonator when the qubit is in its ground state $|0\rangle$ (top panel) and excited state $|1\rangle$ (bottom panel). **(b)** Contour plot of the state discrimination within the two parametric oscillation regions. The black circle in the left region, located at $[\delta^{|0\rangle}/\Gamma = -5.34, \epsilon/\Gamma = 3.56]$, represents the bias point used throughout the rest of the analysis and in Fig. 4.8(b). The state discrimination at this point is 81.5%.

4.3.2 Fidelity analysis

We evaluate the obtainable readout state discrimination by collecting quadrature-voltage histograms at every point within the two regions of parametric oscillations in the $[\delta, \epsilon]$-plane — see Fig. 4.9(b). We choose the same pump operation point, $\delta^{|0\rangle}/\Gamma = -5.34$, $\epsilon/\Gamma = 3.56$, for which the output field is shown in Fig. 4.8(b) indicated by the black circle, and show the characterization in detail in Fig. 4.10. At this operation point, the state discrimination has reached a plateau around 81.5%. Each histogram in Fig. 4.10(a–b) contains in-phase (V_I) and quadrature (V_Q) voltage measurements from 10^5 readout cycles, with each measurement being the mean quadrature voltage within the sampling time τ_s (blue window in Fig. 4.8). We project each of the 2D-histograms onto its real axis, and thus construct 1D-histograms of the V_I component — see Fig. 4.10(c). We can then extract a signal-to-noise ratio $\mathrm{SNR} = |\mu_{|1\rangle} - \mu_{|0\rangle}|/(\sigma_{|1\rangle} + \sigma_{|0\rangle}) = 3.39$, where μ and σ denote the mean value and standard deviation, respectively, of the Gaussians used to fit the histograms. The peak separation of the histograms gives a confidence level of 99.998% for the readout fidelity. The peak appearing in the center of the blue trace arises mainly from qubit relaxation prior to and during the readout. We analyze this and other contributions in the next section.

To extract the measurement fidelity from the histograms, we plot the cumulative distribution function of each of the two traces in Fig. 4.10(c), by summing up the histogram counts symmetrically from the center and outward, using a voltage threshold, V_{th}. From these sums, we obtain the S-curves of the probability to find the qubit in its ground state as a function of the voltage threshold value — see Fig. 4.10(d). We define the fidelity of the measurement as the maximum separation between the two S-curves.

4.3.3 Error budget analysis

To evaluate the fidelity of the readout itself, as compared to the fidelity loss associated with qubit errors, we will now make an error budget, for details see Appended paper II as well as its Supplementary Information. From the histograms in Fig. 4.10(c), we can account for 81.5% of the population, thus missing 18.5%. To find the remaining contributions, we run a Monte Carlo simulation of the qubit population, consisting of the same number of 10^5 readout cycles as in the measured histograms, see code presented in Appendix E. The simulation results are binned in the same way as the measurements, using the Gaussian fits as boundaries, and taking into account the following statistics: (i) qubit relaxation and preparation errors, (ii) thermal population of the qubit, (iii) spurious switching events by π radians of the oscillator phase during readout (yielding a reduced sampled voltage), and (iv) peak-separation error due to the limited signal-to-noise ratio.

We find that the main contribution to the loss of fidelity is due to relaxation prior to and during the readout. From the extracted relaxation time, $T_1 = 4.24\,\mu$s, we obtain a fidelity loss of 11.6%. This error can be made smaller by coupling the resonator more strongly to the transmission line, thereby decreasing the rise time of the output field, and by improving the T_1 time of the qubit by *e.g.* using a Purcell filter [51, 77, 78]. Note, however, that an increased resonator damping rate, Γ_0, yields an increased bandwidth of the parametric oscillation region. Consequently,

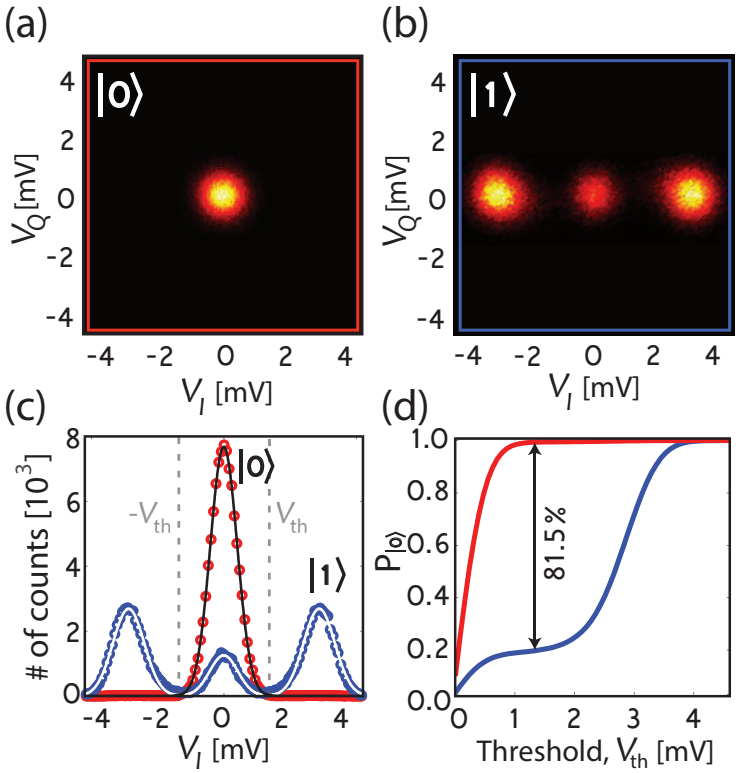

Figure 4.10: Quadrature voltage histograms of the parametric oscillator output, collected after digital sampling. The pump bias point was $[\delta^{|0\rangle}/\Gamma = -5.34, \epsilon/\Gamma = 3.56]$ — see Fig. 4.9(b). In panel **(a)**, the qubit was in its ground state; in **(b)**, a π pulse was applied prior to the readout pulse. **(c)** 1D-histograms of the in-phase voltage component, V_I, from the quadrature histograms in (a) and (b). The black and white solid lines are Gaussian fits, from which we extracted a signal-to-noise ratio of 3.39. **(d)** Cumulative distribution functions, corresponding to the $|0\rangle$ and $|1\rangle$ states, obtained by sweeping a threshold voltage, V_{th}, from the center of the two histograms ($V_I = 0$). The maximum separation between the two S-curves yields a state discrimination of 81.5 %.

the qubit–resonator coupling, g_{01}, needs to be increased accordingly to result in a sufficiently large dispersive frequency shift. From the simulation, we further attribute 4.5% to qubit preparation errors. Another 1.1% can be explained from thermal population of the qubit; this corresponds to an effective qubit temperature of $T_q = 45\,\mathrm{mK}$. By adding these loss contributions due to the qubit to the measured state discrimination, we obtain a readout fidelity $F_{\mathrm{ro}} = 81.5\% + 11.6\% + 4.5\% + 1.1\% = 98.7\%$.

There are also errors introduced by the parametric oscillator itself. A major error is caused by switching events between the π-shifted oscillating states, which reduce the overall measured voltage amplitude. To extract the probability of switching, we performed a separate control measurement that yielded 2.4% switching probability, which translates to a maximal fidelity loss of half of that, 1.2%. The switching rate of the parametric oscillator depends on many parameters, including damping rates and bias points; this error can therefore, with careful engineering, be decreased even further. We could, however, eliminate the effect of phase-switching events by using a detection scheme that measures the absolute value of the output field, instead of

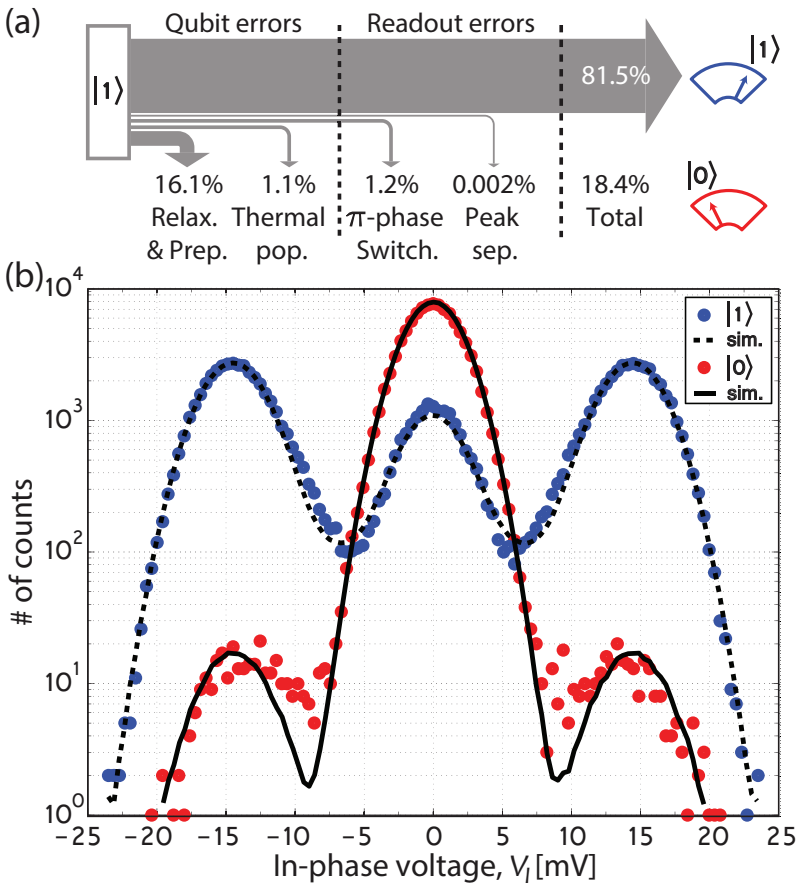

Figure 4.11: **(a)** Schematics of the different contributions going into the Monte Carlo simulation. The errors are divided into qubit errors and readout errors. **(b)** The solid red and blue dots are the histogram bins from Fig. 4.10(c), here plotted on a logaritmic scale. The solid and dashed black lines represent the outcome of the simulation of the different error contributions.

the amplitude.

The last and smallest contribution to the fidelity loss is the peak separation error, which accounts for the intrinsic overlap between the histograms. However, this contribution is only 0.002% for our SNR of 3.39, and can therefore be neglected.

4.4 Multimode parametric amplifier

In this section, we discuss the main idea behind the measurements on a multimode parametric amplifier, developed mainly by M. Simoen and published in Appended paper IV. In principle, this device is constructed from the same type of $\lambda/4$ parametric resonator as discussed throughout the rest of this thesis. However, with the important distinction that its fundamental resonant frequency is designed to be around 1 GHz, allowing us to access higher modes of the resonator within our measurement band (4 - 8 GHz). In particular, the system is characterized as a parametric amplifier, both using single and multimode pumping.

Characteristic frequency spectrum

As with all parametric resonators, the first step in the device characterization is to investigate its frequency tuning as a function of applied magnetic flux. However, in this case we are not interested in the fundamental mode of the slightly anharmonic resonator spectrum, but higher harmonics thereof. In Fig. 4.12, the frequency spectra of the two investigated modes ($m = 2, 3$) are plotted as a function of external magnetic flux, fitted to the characteristic equation

$$\frac{\pi f_m}{2f_{\lambda/4}} \tan\left(\frac{\pi f_m}{2f_{\lambda/4}}\right) = \left|\cos\left(\frac{\pi\Phi_{\mathrm{dc}}}{\Phi_0}\right)\right| \frac{L_r}{L_{\mathrm{sq}}} - \frac{\pi f_m}{2f_{\lambda/4}} \frac{C_{\mathrm{sq}}}{C_r}, \tag{4.9}$$

where L_{sq} and C_{sq} denote the SQUID inductance (at zero flux) and capacitance, respectively. The resonant frequencies of the two higher modes ($m = 2, 3$), are related to the fundamental frequency as $f_m(0) \approx (2m+1) \times f_0(0)$ and can be tuned down to minimum frequencies $f_m(\Phi_0/2) \approx (2m) \times f_0(0)$, see Fig. 4.12(a).

Single- and multimode parametric operation

The aim of this study is to investigate and compare two different ways to obtain parametric amplification in the device. In the single mode pumping scheme, both the signal and the idler of the downconverted pump signal fall within the same mode, $f_p = 2f_m$, see Fig. 4.12(b). In the multimode case, the pump tone is instead applied at the sum frequency of two modes, $f_p = f_m + f_{m+1}$, which means that the signal and idler will appear in two different modes, see Fig. 4.12(c).

Appended paper IV describes a comparative study between the two different operation modes. After calibrating the measurement line using a shot-noise thermometer, the amplifier performance is presented in terms of the amplifier gain, amount of added noise photons, gain-bandwidth product, and saturation power. In conclusion, both single and two mode pumping yield quantum limited amplification.

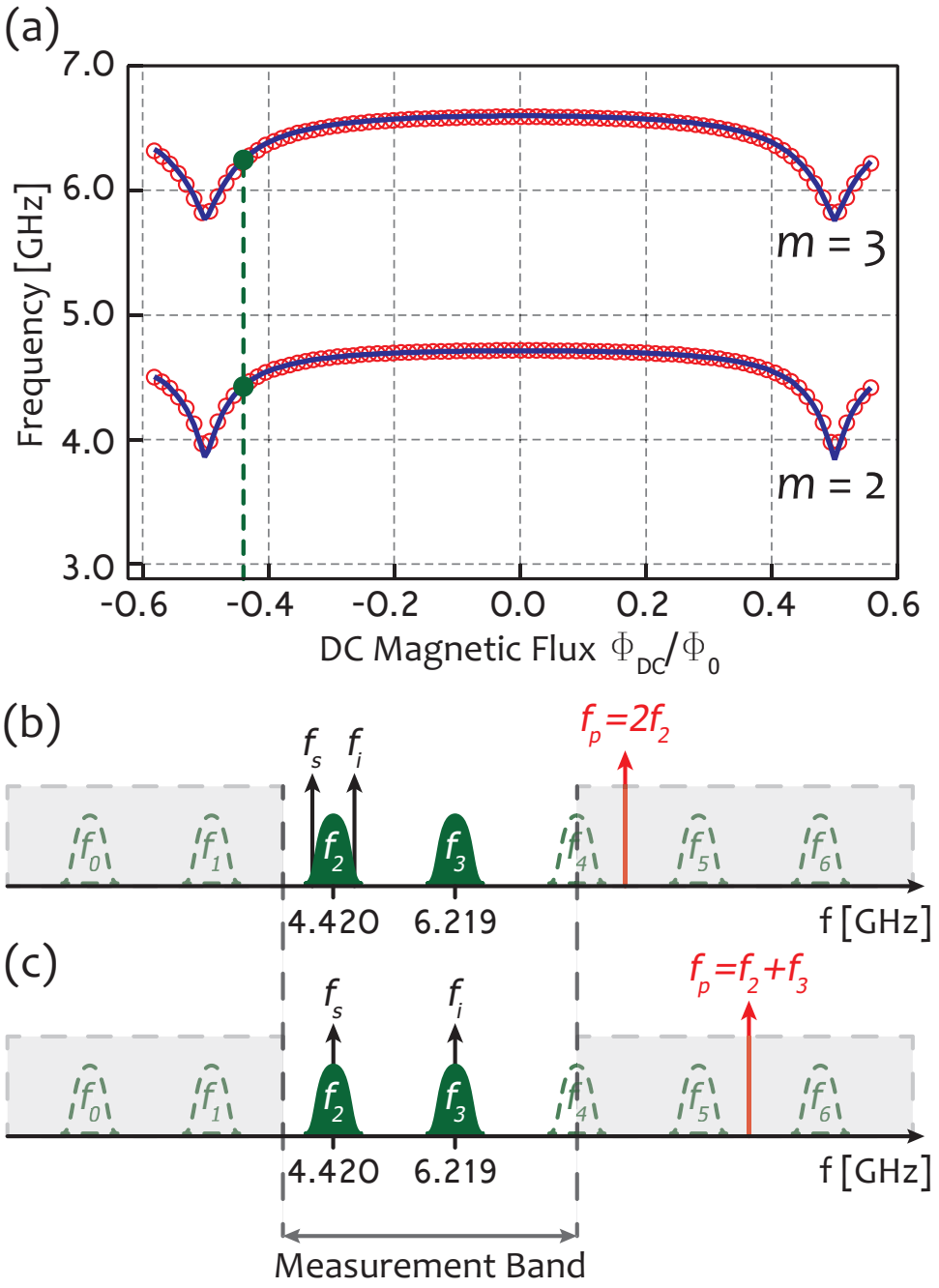

Figure 4.12: **(a)** Measured resonant frequencies of modes $m = 2, 3$ as a function of applied magnetic flux, Φ_{dc}, red circles. The zero flux frequencies of these modes are $f_2(0) = 4.713\,\mathrm{GHz}$ and $f_3(0) = 6.588\,\mathrm{GHz}$. The blue solid lines are fits to Eq. 4.9, where the two modes were numerically fitted simultaneously. The dashed green line indicate the operation point, $\Phi_{\mathrm{dc}} = -0.44\Phi_0$, around which the parametric characterization was performed. **(b)** When the pump tone is applied at a frequency $f_p = 2 \times f_2$ and the signal tone, f_s, falls within the linewidth of mode 2. The idler tone is then generated such that $f_s + f_i = f_p$, *i.e.* symmetric around $f_p/2$. **(c)** If the pump tone instead is applied at $f_p = f_2 + f_3$ and the signal falls within the linewidth of mode 2. Again, the idler is generated symmetrically around $f_p/2$ with respect to the signal and will thus end up in mode 3. The image is modified from the original in Appended Paper IV, with permission from M. Simoen.

Chapter 5

5 Summary & Outlook

Throughout the core of this thesis, focus has been on developing a single-shot readout technique for a superconducting qubit embedded in a Josephson parametric oscillator (JPO). Our device consists of a superconducting quarter-wavelength resonator, shorted to ground via a tailored nonlinear inductance, realized by a pair of Josephson junctions connected in parallel, forming a SQUID. By threading a magnetic flux through the loop of the SQUID, its inductance (and thus the electrical length of the resonator) is modified allowing us to control the resonant frequency of the device. A static dc-flux is supplied using a superconducting coil mounted on the sample box, whereas ac-flux is applied using an on-chip fast tuning line. By modulating (or pumping) the resonant frequency of the JPO, parametric oscillations build up the field inside the resonators within a certain region in pump strength and frequency.

Paper I is dedicated to characterize two dominant non-linearities present in the system, namely, the Duffing nonlinearity and the pump-induced nonlinearity. The first one arises from the nonlinearity of the Josephson inductance and is therefore photon-number dependent, whereas the second is a rectification effect due to the nonlinear flux curve on which the resonant frequency is modulated. Common for both these effects is the associated shift of the resonant frequency of the JPO, which ultimately saturates the amplitude of parametric oscillations. The most important message from this study is that both these effects easily can be predicted, by extracting the inductive participation ratio from the resonator. Moreover, the two effects are dominant in different limits of the applied magnetic flux. The results presented in this study can be thought of as a first necessary step towards realizing the JPO qubit readout. My contribution to this work was the device fabrication and data analysis. The data was aquired by Y. Reshitnyk at University of Queensland in Australia. W. Wustmann and V. Shumeiko contributed with important theoretical input.

In **Paper II**, the main results of the thesis are presented. Here, a superconducting transmon qubit is embedded in the Josephson parametric oscillator. We demonstrate a new single-shot readout technique, utilizing the strong nature of the parametric oscillations, as well as the dispersive shift exerted on the resonator when

exciting the qubit. Consequently, we can encode the quantum state of the qubit onto the response of the parametric oscillator: the excited state of the qubit, $|1\rangle$, corresponds to the oscillating state with 185±15 photons in the resonator, whereas the ground state, $|0\rangle$, corresponds to an empty resonator. Throughout this project, I designed, fabricated, and measured the device.

In **Paper III**, a linearized circuit impedance model for the flux-driven SQUID, called "the pumpistor", is presented. The main idea behind this work is to develop a useful framework, allowing for engineering of more advanced parametric circuits. The notion is that the frequency mixing taking place in the SQUID appears as a negative resistance (for proper choice of the pump phase), thus providing gain. In this paper, the model is outlined for the same design of quarter-wavelength parametric resonator that is used in papers I and II. However, this model can easily be generalized to more complex circuits and pumping schemes. This work was mainly developed by K. Sundqvist and my contribution was discussions about circuit realizations and input on measurements of the quarter-wavelength superconducting resonators for which the model was originally developed.

In **Paper IV**, we explore the performance of a multimode parametric amplifier, specifically designed to have a fundamental mode frequency of less than 1 GHz, thus allowing us to access its higher harmonics within the bandwidth of our measurement setup. In particular, we study and compare degenerate parametric amplification, using a single resonant mode, with nondegenerate parametric amplification, using two different modes. A shot-noise thermometer is used to evaluate the noise performance of the two pumping schemes and we show that the quantum limit is reached for both operation schemes. This project was carried out by M. Simoen and my contribution was assistance with input on fabrication as well as discussions throughout the project.

In **Paper V**, we investigate the thickness distribution along our Josephson junctions using transmission electron microscopy. By measuring the junction thickness at several positions along the junction, we collect statistics on the barrier thickness variation for junctions fabricated using different oxidation parameters. Our results suggest that the oxidation time has a larger impact on the barrier thickness as compared to the oxidation pressure. Moreover, we confirm the previous observation that only less than 10 % of the junction area contributes to its conductance. This work was carried out by L. Zeng and my contribution was to discuss the aspects of fabrication of the devices and inpact of the different oxidation processes used for the TEM study.

Finally, **Paper VI** describes the atomic details of an observed interfacial layer between the bottom electrode of our Josephson junction and an HF-treated Si substrate. Here, we again use transmission electron microscopy to study the element contents within this interfacial layer with atomic resolution, finding intermixing between Al from the junction electrode, O from the interface, and Si from the substrate. The method relies on studying the electron energy loss spectrum of a scanning TEM measurement and can be readily applied to study other interfaces, yielding detailed information about the content of the studied region. My contribution to this work, mainly carried out by L. Zeng, was to fabricate the device and support input on fabrication details on the oxidation process.

There are many interesting future perspectives for the work presented in this thesis. First of all, there are a couple of immediate ways to improve the readout

fidelity of the Josephson parametric oscillator readout. The qubit relaxation prior to and during the readout can be reduced by placing a properly designed Purcell filter on the output of the device, thus enhancing the coherence time of the qubit, while allowing us to make the readout resonator faster. Also the fidelity errors due to the parametric oscillator can be removed by modifying the detection scheme in such a way that the switching events of the parametric oscillator is not reducing the readout fidelity. After these modifications have been properly implemented, our readout scheme could be frequency multiplexed and more qubits could be added to each resonator, realizing various gates jointly readout using the parametric oscillators. In addition, the qubits could also by themselves serve as probes to study the internal dynamics of the parametric oscillator, where a photon-number sensitive probe could be useful. Finally, the parametric resonator could be used as a squeezer to expose the qubit to squeezed light. This could potentially be more efficient as compared to when the squeezed light is inserted via the coupling capacitor.

Appendix A

Clean room processes

A.1 Recipe for parametric amplifiers

In this appendix, we present the clean room recipes used for fabricating the parametric amplifiers which were used as pre-amplifiers during some of the cooldowns. All devices were fabricated on p-doped 2"-silicon wafers with 400 nm wet grown oxide in the Nanofabrication Laboratory at Chalmers.

1. Cleaning the wafer

1165 Remover	$60 - 70°$C, 10 min
	Rinse in IPA and blowdry with N_2
Ultrasonic bath	100%, 1 min
IPA bath	Circulation 2 min
QDR bath	Rinse in IPA and blowdry with N_2

2. Deposition of Niobium in MTD 450 sputter

Deposition rate	0.667 nm/s
Pre-sputter time	5 min
Nb DC-power	200 W
Ar pressure	8 μbar
Ar Flow	60 sccm
Thickness	40 + 40nm (cool down for 4 min inbetween)

3. Photolithography to define alignment marks and bonding pads

1165 Remover	$60-70$°C, 5 min
	Rinse in IPA and blowdry with N_2
Ashing	50 W, 40 sccm O_2, 20 s
Pre-bake on hotplate	110°C, 1 min
Spin lift-off resist LOR3B	3000 rpm, 1 min, $t_{acc} = 1.5$ s ($t \approx 350$nm)
Softbake on hotplate	200°C, 5 min
Spin photoresist S1813	3000 rpm, 1 min, $t_{acc} = 1.5$ s ($t \approx 150$nm)
Softbake on hotplate	110°C, 2 min
Expose pattern	MA6 mask aligner, Lo-vac mode, $P_{vac} = 0.4$ bar
	6 W/cm^2, $t_{exp} = 8.5$ s
Develop in MF319	45 s (Lift up and rinse after 20 s.)
QDR bath	Rinse in IPA and blowdry with N_2

4. Electron beam evaporation of metals in Lesker PVD225

Ashing in O_2-plasma	50 W, 20 s
Chamber pressure	$P_{ch} \leq 10^{-7}$mbar
E-beam evaporation	Sticking layer (Ti), 30Å, 1 Å/s
	Contact layer (Au), 800Å, 1-2 Å/s
	Stopping layer (Pd), 100Å, 1 Å/s
Lift-off in 1165 Remover	$60-70$°C, $t \approx 30$ min
	Rinse in IPA and blowdry with N_2

5. Electron beam lithography to define resonators in JEOL JBX-9300FS

Ashing in oxygen plasma	50 W, 20 s
Pre-bake on hotplate	130°C, 1 min
Spin UV60,0.75	3000 rpm, $t_{acc} = 1.5$ s for 1 min
Softbake on hotplate	130°C, 1 min
Expose JEOL JBX-9300FS	$V_{acc} = 100$kV, I = 70 nA, Dose: 27 μC/cm^2
Post-bake on hotplate	130°C, 1 min
Develop UV60 resist	MF-CD-26, 40 s
QDR bath	Blowdry with N_2

6. Etching of Niobium to defining waveguides in Oxford Plasmalab System 100

NF_3	50 sccm for ≈45 s
RF Generator power	30 W
ICP power	200 W
Laser interferometer mode	End point detection
Ashing in oxygen plasma	50 W, 20 s, 10 sccm
1165 Remover	$60-70$°C, 5 min
	Rinse in IPA and blowdry with N_2

7. Electron beam lithography to define Josephson junctions in JEOL JBX-9300FS

Ashing in oxygen plasma	50 W, 20 s
Spin MMA(8.5)EL10	500 rpm, $t_{acc} = 2$ s for 5 s
	2000 rpm, $t_{acc} = 5$ s for 45 s (≈ 570 nm)
Softbake on hotplate	170°C, 5 min
Spin ZEP 520A(1:1)	3000 rpm, $t_{acc} = 1.5$ s, 1 min (≈150 nm)
Softbake on hotplate	170°C, 5 min
Expose	$V_{acc} = 100$kV, I=2 nA, Dose: 300μC/cm^2

8. Dicing of wafer into individual 5x7 mm chips in Loadpoint Microace 3+

Alignment of camera	Make a test cut and adjust the camera to match the blade
Alignment cuts from frontside	Make cuts in both channel A and B one pitch away from first cut
	Protect active region using another piece of tape
Dicing from backside	Cut all way through the wafer in both channels
Blade type:	5KT22L50
Blade feed rate:	3 mm/s
Spindle speed:	35 000 rpm

9. Two-angle evaporation of Al/AlO_X/Al Josephson junctions in Plassys MEB 550 S

Develop top resist	o-xylene 96% grade, 3 min
	Dip in IPA and immediately blowdry with N_2
Develop bottom resist	H_2O:IPA 1:4, 4 min 50 s (undercut $\geq 0.2\mu$m)
Ashing in oxygen plasma	50 W, 20 s
Electron beam evaporation	$P_{ch} \leq 3 \times 10^{-7}$mbar
Ar ion milling	250V, 20mA, $\pm 30°$, 1+1 min
Bottom layer of Al	40 nm, 5Å/s, $\alpha = 28°$
Dynamic oxidation	$P_{ox} = 0,2$ mbar, $t_{ox} = 30$ min
Top layer of Al	65 nm, 5Å/s, $\alpha = -28°$
Lift-off in 1165 Remover	$60 - 70°$C, ≈ 20 min
	Rinse in IPA and blowdry with N_2

A.2 Recipe for parametric readout samples

In this appendix, we present the clean room recipe used for fabricating the parametric readout samples consisting of the parametric resonators with embedded transmon qubits. As oppose to the parametric amplifiers, these samples were fabricated on 2" C-plane sapphire wafers in the Nanofabrication Laboratory at Chalmers.

1. Cleaning the wafer

1165 Remover	$60-70$°C, 10 min
	Rinse in IPA and blowdry with N_2
Ultrasonic bath	100%, 1 min
IPA bath	Circulation 2 min
QDR bath	Rinse in IPA and blowdry with N_2

2. Furnace tube annealing

Temperature	1100°C
Ramp up time	4 hours, (5°C/min)
Hold time	6 hours
Ramp down time	4 hours, (5°C/min)
Environment	O_2:N_2, 1:4

2. Deposition of Niobium in MTD 450 sputter

Deposition rate	0.667 nm/s
Pre-sputter time	5 min
Nb DC-power	200 W
Ar pressure	8μbar
Ar Flow	60 sccm
Thickness	40 + 40nm (cool down for 4 min inbetween)

4. Photolithography to define alignment marks and bonding pads

1165 Remover	$60-70$°C, 5 min
	Rinse in IPA and blowdry with N_2
Ashing	50 W, 40 sccm O_2, 20 s
Pre-bake on hotplate	110°C, 1 min
Spin lift-off resist LOR3B	3000 rpm, 1 min, $t_{acc} = 1.5$ s ($t \approx 350$nm)
Softbake on hotplate	200°C, 5 min
Spin photoresist S1813	3000 rpm, 1 min, $t_{acc} = 1.5$ s ($t \approx 150$nm)
Softbake on hotplate	110°C, 2 min
Expose pattern	MA6 mask aligner, Lo-vac mode, $P_{vac} = 0.4$ bar
	6 W/cm^2, $t_{exp} = 8.5$ s
Develop in MF319	45 s (Lift up and rinse after 20 s.)
QDR bath	Rinse in IPA and blowdry with N_2

5. Electron beam evaporation of metals in Lesker PVD225

Ashing in O_2-plasma	50 W, 20 s
Chamber pressure	$P_{ch} \leq 10^{-7}$mbar
E-beam evaporation	Sticking layer (Ti), 30Å, 1 Å/s
	Contact layer (Au), 800Å, 1-2 Å/s
	Stopping layer (Pd), 100Å, 1 Å/s
Lift-off in 1165 Remover	$60-70$°C, $t \approx 30$ min
	Rinse in IPA and blowdry with N_2

6. Electron beam lithography to define resonators in JEOL JBX-9300FS

Ashing in oxygen plasma	50 W, 20 s
Pre-bake on hotplate	130°C, 1 min
Spin UV60,0.75	3000 rpm, t_{acc} = 1.5 s for 1 min
Softbake on hotplate	130°C, 1 min
Expose JEOL JBX-9300FS	V_{acc} = 100kV, I = 35 nA, Dose: 27 μC/cm^2
Post-bake on hotplate	130°C, 1 min
Develop UV60 resist	MF-CD-26, 40 s
QDR bath	Blowdry with N_2

7. Etching of Niobium to defining waveguides in Oxford Plasmalab System 100

NF_3	50 sccm for ≈55 s
RF Generator power	30 W
ICP power	200 W
Laser interferometer mode	End point detection
Ashing in oxygen plasma	50 W, 20 s, 10 sccm
1165 Remover	60 − 70°C, 5 min
	Rinse in IPA and blowdry with N_2

8. Electron beam lithography to define Josephson junctions in JEOL JBX-9300FS

Ashing in oxygen plasma	50 W, 20 s
Spin MMA(8.5)EL10	500 rpm, t_{acc} = 2 s for 5 s
	2000 rpm, t_{acc} = 5 s for 45 s (≈ 570 nm)
Softbake on hotplate	170°C, 5 min
Spin SX AR-P 6200/2, 2:1	2000 rpm, t_{acc} = 1.5 s, 1 min (≈150 nm)
Softbake on hotplate	170°C, 5 min
Expose	V_{acc} = 100kV, I=2 nA, Dose: 380μC/cm^2

9. Dicing of wafer into individual 5x7 mm chips in Loadpoint Microace 3+

Alignment of camera	Make a test cut to adjust the camera to match the 500 μm thick blade
Dicing from backside Ch A	Cut half way through the wafer using cut auto
	Cut all way through the wafer using cut single and height sense in between
Dicing from backside Ch B	Cut half way through the wafer using cut auto
	Cut all way through the wafer using cut single and height sense in between
Blade type:	K015-600 JXS
Blade feed rate:	0.3 mm/s
Spindle speed:	21 000 rpm

10. Two-angle evaporation of $Al/AlO_X/Al$ Josephson junctions in Plassys MEB 550 S

Develop top resist	n-amyl acetate 99%, 3 min
	Dip in IPA and immediately blowdry with N_2
Develop bottom resist	H_2O:IPA 1:4, 5 min 30 s (undercut $\geq 0.2\mu$m)
Ashing in oxygen plasma	50 W, 20 s
Electron beam evaporation	$P_{ch} \leq 3 \times 10^{-7}$mbar
Planetary rotation	position 1 (exposing the parametric resonator SQUID)
Ar ion milling	250V, 20mA, $\pm 30°$, 1+1 min
Bottom layer of Al	40 nm, 5Å/s, $\alpha = 20°$
Dynamic oxidation	$P_{ox} = 0,2$ mbar, $t_{ox} = 35$ min
Top layer of Al	65 nm, 5Å/s, $\alpha = -20°$
Planetary rotation	position 2 (exposing the transmon junctions)
Ar ion milling	250V, 20mA, $\pm 30°$, 1+1 min
Bottom layer of Al	40 nm, 5Å/s, $\alpha = 20°$
Dynamic oxidation	$P_{ox} = 1$ mbar, $t_{ox} = 50$ min
Top layer of Al	65 nm, 5Å/s, $\alpha = -20°$
Lift-off in 1165 Remover	$60 - 70°$C, ≈ 20 min
	Rinse in IPA and blowdry with N_2

A.3 Electroplating of gold

Preparations

1. Pour the BDT 200 gold solution in a plastic beaker and heat it up by placing it in heated DI water bath. Set the bath temperature set point to 80°C and monitor the BDT temperature using a stick thermometer. When it has reached 58°C, reduce the set point of the water bath to 60°C.
2. Heat up another glass beaker of water to 55°C on a hotplate. This water is for rinsing the goldplated pieces.
3. Prepare a plastic beaker of copper etch solution.
4. Place the magnet stirrer on the bottom of the beaker and make sure it can rotate freely.
5. Measure the surface area of all the pieces.
6. Stick down the metal grid into the gold solution such that the surface area is the same as the work piece.
7. Mount the workpiece on a metal wire or clamped with tweezers and attach it to the other electrode.

Gold plating procedure

1. Turn on the plating and carefully ramp up the current such that the current density (≈ 2 mA/cm^2) matches the size of the work piece.
2. Monitor the surfaces to ensure that the gold sticks to the work piece. If not, turn off the current and re-mount the work piece. This can also be needed if the gold has not reached all surfaces of the work piece.
3. Let the piece be in the plating bath for about 20 min in total.
4. Ramp down the current and turn off the power supply.
5. Dip the mounted workpiece in the 55° C water beaker and then rinse it with the DI-water gun.
6. Blowdry with N_2.

Appendix B

Resonator fitting function

In order to extract the quality factors of the resonator (driven in its linear regime), we derive an expression for the lumped element representation of the resonant cavity, see Fig. 2.1(b), valid close to resonance. The reflection coefficient, S_{11} can be related to the impedance of the probe line, Z_0 and the resonator, Z_r as [11],

$$S_{11} = \frac{Z_r - Z_0}{Z_r + Z_0}, \tag{B.1}$$

where the impedance of the lumped element resonator circuit is

$$Z_r = \frac{1}{i\omega C_c} + \left(\frac{1}{R_r} + \frac{1}{i\omega L_r} + i\omega C_r\right)^{-1} = \frac{1 - \omega^2 L_r(C_r + C_c) + \frac{i\omega L_r}{R_r}}{i\omega C_c(1 - \omega^2 L_r C_r) - \frac{\omega C_c L_r}{R_r}}. \tag{B.2}$$

Substitution of (B.2) into (B.1) yields

$$S_{11} = \frac{1 - \omega^2 L_r\left(C_r + C_c\left(1 - \frac{Z_0}{R_r}\right)\right) + i\omega\left(\frac{L_r}{R_r} - Z_0 C_c\left(1 - \omega^2 L_r C_r\right)\right)}{1 - \omega^2 L_r\left(C_r + C_c\left(1 + \frac{Z_0}{R_r}\right)\right) + i\omega\left(\frac{L_r}{R_r} + Z_0 C_c\left(1 - \omega^2 L_r C_r\right)\right)}. \tag{B.3}$$

Assuming that $R_r \gg Z_0$ and introducing $\omega_0 = 1/\sqrt{L_r(C_r + C_c)}$ and $x = \omega/\omega_0$ yields

$$S_{11} = \frac{1 - x^2 + ix\omega_0\left(\frac{L_r}{R_r} - Z_0 C_c\left(1 - x^2\omega_0^2 L_r C_r\right)\right)}{1 - x^2 + ix\omega_0\left(\frac{L_r}{R_r} + Z_0 C_c\left(1 - x^2\omega_0^2 L_r C_r\right)\right)}. \tag{B.4}$$

The aim is to express the resonator impedance in terms of the internal and external quality factors as well as the resonance frequency. We can relate these quantities to the circuit elements as,

$$Q_i = \omega_0 R_r(C_r + C_c), \tag{B.5}$$

$$Q_e = \frac{C_r + C_c}{Z_0 C_c^2 \omega_0}, \tag{B.6}$$

$$S_{11} = \frac{1 - x^2 + ix\left(\frac{\omega_0^2 L_r (C_r+C_c)}{Q_i} + \frac{x^2 C_r - (C_r+C_c)}{C_c Q_e}\right)}{1 - x^2 + ix\left(\frac{{\omega_0}^2 L_r (C_r+C_c)}{Q_i} + \frac{(C_r+C_c) - x^2 C_r}{C_c Q_e}\right)}. \tag{B.7}$$

Next, we introduce the coupling parameter as the ratio of the coupling capacitance to the total capacitance $\kappa = C_c/(C_r + C_c) \ll 1$ and emphasize that the frequency is in close vicinity from the resonator frequency

$$\omega = \omega_0 + \delta\omega, \tag{B.8}$$

$$S_{11} = \frac{1 - \left(1 + 2\frac{\delta\omega}{\omega_0}\right) + i\left(1 + \frac{\delta\omega}{\omega_0}\right)\left(\frac{1}{Q_i} - \frac{1-(1-\kappa)\left(1+2\frac{\delta\omega}{\omega_0}\right)}{\kappa Q_e}\right)}{1 - \left(1 + 2\frac{\delta\omega}{\omega_0}\right) + i\left(1 + \frac{\delta\omega}{\omega_0}\right)\left(\frac{1}{Q_i} + \frac{1-(1-\kappa)\left(1+2\frac{\delta\omega}{\omega_0}\right)}{\kappa Q_e}\right)} =$$

$$= \frac{-2\frac{\delta\omega}{\omega_0} + i\left(\frac{1}{Q_i} - \frac{1}{Q_e} + \frac{2(1-\kappa)\frac{\delta\omega}{\omega_0}}{\kappa Q_e}\right) + i\left(\frac{\frac{\delta\omega}{\omega_0}}{Q_i} - \frac{\frac{\delta\omega}{\omega_0}}{Q_e} + \frac{2(1-\kappa)\left(\frac{\delta\omega}{\omega_0}\right)^2}{\kappa Q_e}\right)}{-2\frac{\delta\omega}{\omega_0} + i\left(\frac{1}{Q_i} + \frac{1}{Q_e} - \frac{2(1-\kappa)\frac{\delta\omega}{\omega_0}}{\kappa Q_e}\right) + i\left(\frac{\frac{\delta\omega}{\omega_0}}{Q_i} + \frac{\frac{\delta\omega}{\omega_0}}{Q_e} - \frac{2(1-\kappa)\left(\frac{\delta\omega}{\omega_0}\right)^2}{\kappa Q_e}\right)}. \tag{B.9}$$

Now, we multiply with $-\omega_0/2$ and assume small frequency detuning

$$\kappa Q_i, \kappa Q_e \gg 1 \tag{B.10}$$

$$S_{11} = \frac{\delta\omega - i\left(\frac{\omega_0}{2Q_i} - \frac{\omega_0}{2Q_e} + \frac{(1-\kappa)\delta\omega}{\kappa Q_e}\right) - i\left(\frac{\delta\omega}{2Q_i} - \frac{\delta\omega}{2Q_e} + \frac{(1-\kappa)\frac{\delta\omega^2}{\omega_0}}{\kappa Q_e}\right)}{\delta\omega - i\left(\frac{\omega_0}{2Q_i} + \frac{\omega_0}{2Q_e} - \frac{(1-\kappa)\delta\omega}{\kappa Q_e}\right) - i\left(\frac{\delta\omega}{2Q_i} + \frac{\delta\omega}{2Q_e} - \frac{(1-\kappa)\frac{\delta\omega^2}{\omega_0}}{\kappa Q_e}\right)} \approx$$

$$\approx \frac{\delta\omega - i\left(\frac{\omega_0}{2Q_i} - \frac{\omega_0}{2Q_e}\right)}{\delta\omega - i\left(\frac{\omega_0}{2Q_i} + \frac{\omega_0}{2Q_e}\right)} \tag{B.11}$$

Finally, we can divide all terms by a factor of 2π and introduce the linewidths (damping rates) associated with the two quality factors $\Gamma_{R,0} = f_0/(2Q_{i,e})$, yielding reflection coefficients on the form

$$S_{11} = \frac{\delta f^2 + (\Gamma_R^2 - \Gamma_0^2) + i2\Gamma_0\delta f}{\delta f^2 + (\Gamma_R + \Gamma_0)^2}. \tag{B.12}$$

The magnitude and phase of the reflection coefficient are thus

$$|S_{11}| = \sqrt{\mathrm{Re}\left[S_{11}\right]^2 + \mathrm{Im}\left[S_{11}\right]^2} = \frac{\sqrt{\left(\delta f^2 + (\Gamma_R^2 - \Gamma_0^2)\right)^2 + \left(2\Gamma_0\delta f\right)^2}}{\delta f^2 + (\Gamma_R + \Gamma_0)^2}, \tag{B.13}$$

$$\arg\left(S_{11}\right) = \arctan\left(\frac{\mathrm{Im}\left[S_{11}\right]}{\mathrm{Re}\left[S_{11}\right]}\right) = \arctan\left(\frac{\Gamma_0 \delta f}{\delta f^2 + \left(2\Gamma_R + \Gamma_0\right)^2}\right). \tag{B.14}$$

Appendix C

Conformal mapping

To simulate the inductance and capacitance per unit length we use conformal mapping, where the electric field lines between the center conductor and ground planes are mapped onto those of a parallel plate capacitor. The dielectric environment of the sample layers is taken into account by deriving a capacitance assosiated with each dielectric layer. In this section, we go through the equations used to simulate the characteristic impedance.

We start out from the capacitance of the partial dielectric regions, C_1 and C_2 is expressed as

$$C_i = 2\epsilon_0 \left(\epsilon_{r,i} - 1\right) \frac{K(k_i)}{K(k_i')}, \tag{C.1}$$

where ϵ_0 and $\epsilon_{r,i}$ are the vacuum and relative perimittivity, respectively, and K denotes elliptic integrals with modulus, k_i and k_i', defined as

$$k_i = \frac{\sinh\left(\pi w/4h_i\right)}{\sinh\left(\pi(w+2g)/4h_i\right)} \qquad k_i' = \sqrt{1-k_i} \qquad i \in [1,2], \tag{C.2}$$

where w and g are the widths of the center conductor and gaps, respectively. Next, the capacitive contribution from the vacuum in absence of the dielectric layers below the conductor is given by

$$C_{\text{vac}} = 2\epsilon_0 \left[\frac{K(k_3)}{K(k_3')} + \frac{K(k_4)}{K(k_4')}\right] \tag{C.3}$$

with corresponding modulus

$$k_j = \frac{\tanh\left(\pi w/4h_j\right)}{\tanh\left(\pi(w+2g)/4h_j\right)} \qquad k_j' = \sqrt{1-k_j} \qquad j \in [3,4]. \tag{C.4}$$

We can now define an effective dielectric constant

$$\epsilon_{\text{eff}} = 1 + q_1(\epsilon_{r,1} - 1) + q_2(\epsilon_{r,2} - 1) \tag{C.5}$$

where q_1 and q_2 are the partial filling factors, defined as

$$q_i = \frac{K(k_i)}{K(k_i')} \left[\frac{K(k_3)}{K(k_3')} + \frac{K(k_4)}{K(k_4')} \right]^{-1} \qquad i \in [1, 2] \tag{C.6}$$

Moreover, the phase velocity and characteristic impedance can be expressed in terms of the effective dielectric constant

$$v_{\mathrm{ph}} = \frac{c}{\sqrt{\epsilon_{\mathrm{eff}}}} \tag{C.7}$$

$$Z_c = \frac{1}{cC_{\mathrm{vac}}\sqrt{\epsilon_{\mathrm{eff}}}} = \frac{60\pi}{\sqrt{\epsilon_{\mathrm{eff}}}} \left[\frac{K(k_3)}{K(k_3')} + \frac{K(k_4)}{K(k_4')} \right]^{-1} \tag{C.8}$$

Inductance and capacitance per unit length

After calculating the cross section geometry, we can use the same conformal mapping to obtain information about the inductance and capacitance per unit length of the coplanar waveguide transmission line

$$L = \frac{\mu_0}{2} \left[\frac{K(k_3)}{K(k_3')} + \frac{K(k_4)}{K(k_4')} \right]^{-1} \tag{C.9}$$

$$C = 2\epsilon_0\epsilon_{\mathrm{eff}} \left[\frac{K(k_3)}{K(k_3')} + \frac{K(k_4)}{K(k_4')} \right]^{-1} \tag{C.10}$$

Appendix D

Sample box D

In this section, we take a closer look at the sample box used for all cryogenic measurements throughout this thesis. The box consists of four oxygen free Cu parts, each manifactured using an in-house CNC mill. To get a better thermal contact between the mixing chamber of the cryostat and the sample, the pieces are electroplated in Au (without any adhesion layer) prior to assembly. An overview of the sample box design is shown in Fig. D.1 and a step-by-step assemly guide is shown in Fig. D.2.

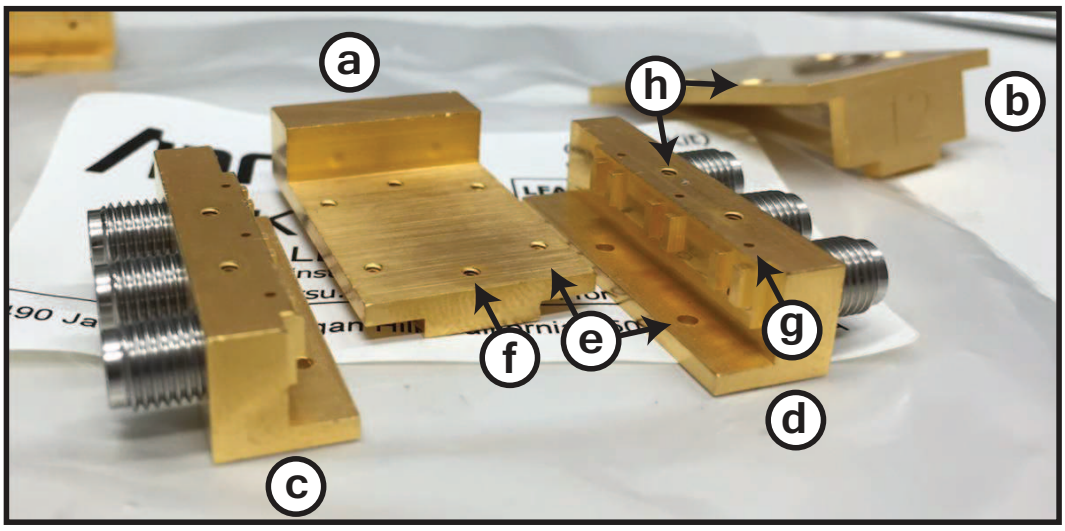

a Bottom
b Lid
c Left side
d Right side
e Bottom assembly
f PCB hole
g Solder pit
h Lid assembly

Figure D.1: Overview of the different parts of the connectorized sample box.

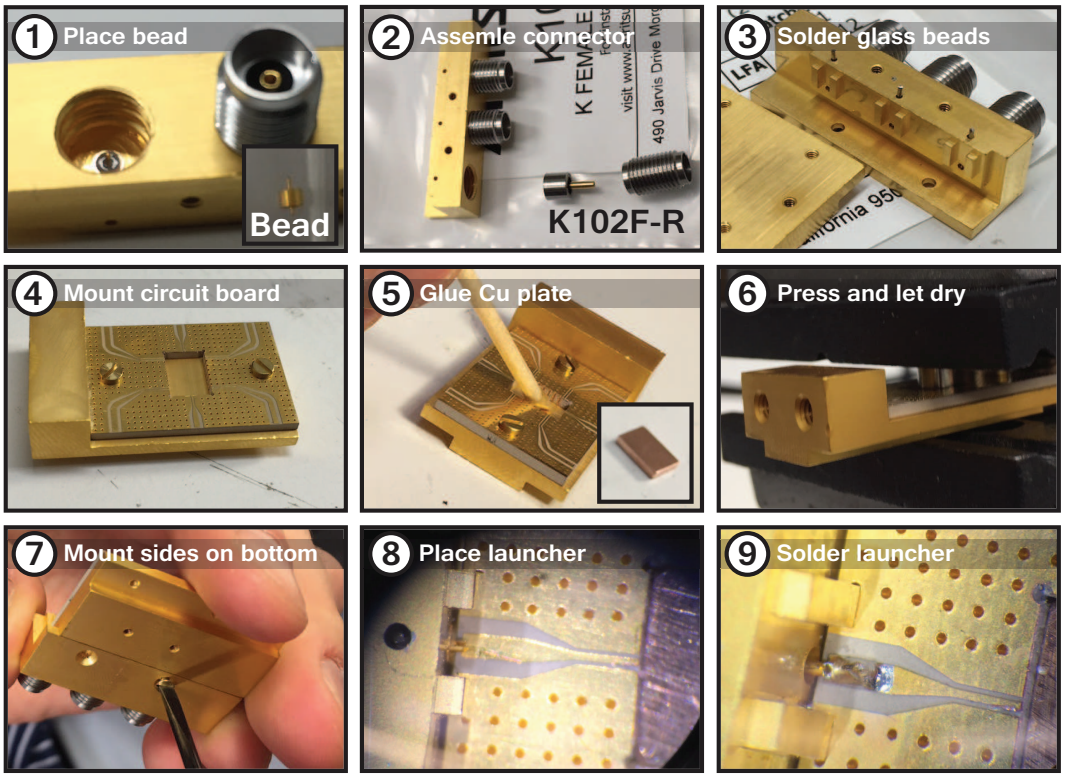

Figure D.2: The sample box assembly step-by-step. (1) Place the glass bead (Huber & Suhner) into the milled out pits, such that the "body" of the bead is aligned with its surrounding edges. Important here is to let the long side of the pin face the K-connector. (2) Screw in the two pieces of the K-connector (Anritsu K102F-R) and make sure that it is properly tightened. If not, the connector might come out later when disconnecting an attached wire. (3) Solder the glass beads by feeding down a small piece of solder into the solder pits. Place the whole side on a hotplate until the solder has melted into the pits. This usually take about 1.5 min @ 300°C. If heated for too long time, the gold will diffuse into the Cu.
(4) Mount the printed circuit board onto the bottom plate using two M1.6 screws. (5) Put some glue in the milled out sample position and place a piece of Cu inside of the pit. This Cu will help to thermalize the sample by anchoring it to the sample box. (6) Place the bottom piece in a vise and press using a proper spacer and let the glue dry. (7) Mount the two side pieces on the bottom piece. Here, the M1.6 screws used need to be filed down to ensure that they do not reach the PCB on the other side. (8) Place microstrip launchers (Anritsu K110-1-R) on the pins from the inside of the box. Make sure that they slide on to the pin properly and that its "lip" reaches the center conductor of the PCB waveguide. (9) Solder the launcher to the PCB and test measure the whole connector, making sure that the center conductor is not shorted to ground (outside of the box).

Appendix E

Program code

E.1 Qubit spectroscopy batch script

The following Python code was used to perform the qubit spectroscopy batch measurements. The functions and routines called throughout the script are part of the Labber™software package developed by Simon Gustavsson[1].

```
import os
import numpy as np
from scipy.optimize import curve_fit
import datetime
import time
import ScriptTools

# Set path to executable
ScriptTools.setExePath('C:\Simons Software\Program')

# Define list of points
vFlux = np.linspace(-3, 3, 301)

# Define measurement objects (format .hdf5)
sPath = os.path.dirname(os.path.abspath(__file__))
MeasResonator = ScriptTools.MeasurementObject(
    os.path.join(sPath, 'PXI_SpectroscopyFindResonator.hdf5'),
    os.path.join(sPath, 'PXI_SpectroscopyFindResonatorOut.hdf5'))

MeasResonatorFine = ScriptTools.MeasurementObject(
    os.path.join(sPath, 'PXI_SpectroscopyFindResonatorFine.hdf5'),
    os.path.join(sPath, 'PXI_SpectroscopyFindResonatorFineOut.hdf5'))

MeasQubit = ScriptTools.MeasurementObject(
    os.path.join(sPath, 'PXI_SpectroscopyFindQubit.hdf5'),
    os.path.join(sPath, 'PXI_SpectroscopyFindQubitOut.hdf5'))

# Go through list of points
```

[1]For more information about Labber, the reader is referred to **http://labber.org**

```
for n1, value_1 in enumerate(vFlux):
    t0=0
    if(n1==0):
        t0=time.time()
    print 'Yokogawa Voltage [mV]:', 1000*value_1
    # Set flux bias
    MeasResonator.updateValue('Yoko coil - Voltage', value_1)
    MeasResonatorFine.updateValue('Yoko coil - Voltage', value_1)
    MeasQubit.updateValue('Yoko coil - Voltage', value_1)

    # 1. Find the resonator frequency
    (x,y) = MeasResonator.performMeasurement()
    # Take absolute value in case y is complex
    y = abs(y)
    # look for the peak position
    print 'Resonator position [GHz]:', x[np.argmin(y)]/1E9

    # Set the center frequency of the fine trace at the center of the resonance
    MeasResonatorFine.updateValue('SigGen 2 - Frequency',
                                  x[np.argmin(y)], 'CENTER')

    # 2. Re-measure the resonator more fine and at lower power
    (x,y) = MeasResonatorFine.performMeasurement()
    y = abs(y)

    # Fit the trace to a Lorentzian
    x=x*1E-9
    y=y*1E6
    def Lorentzian(f, f0, Gamma, A, offset):
        return (A*1/np.pi*Gamma*1E6/2/((f*1E9-f0*1E9)**2+(Gamma*1E6/2)**2)
        + offset*1E-6)*1E6
    try:
        popt, pcov = curve_fit(Lorentzian,x, y,np.array([x[np.argmin(y)],1,
        -(np.abs(y[0]+y[np.size(y)-1])/4),(np.abs(y[0]+y[np.size(y)-1])/2)]))
    except:
        popt=np.array([x[np.argmin(y)]])

    print 'Fitting parameters: ',popt

    # Set new frequency position to the fitted value
    MeasQubit.updateValue('SigGen 2 - Frequency', popt[0]*1E9)

    # 3. Measure the qubit locking the res probe to its resonant frequency
    (x,y) = MeasQubit.performMeasurement()

    # This code presents a projected remaining time of the measurement
    if(n1==0):
        t=time.time()-t0
    print 'Time left: ',
        str(datetime.timedelta(seconds=t*(np.size(vFlux)-n1-1)))

# Re-structure the data files
MeasResonator.rearrangeLog('Yoko coil - Voltage')
MeasResonatorFine.rearrangeLog('Yoko coil - Voltage')
MeasQubit.rearrangeLog('Yoko coil - Voltage')
```

E.2 Monte Carlo simulation for error budget

The following MATLAB code was mainly developed by Andreas Bengtsson, with the aim to simulate the histograms aquired when probing the parametric oscillations, comparing the cases with and without an applied π-pulse on the qubit.

```
% --- Monte Carlo input parameters ---
T1 = 4.24;            % Qubit relaxation time, T1
T = 45e-3;            % Qubit temperature, [K]
td = 0.372;           % Readout delay time, [us]
tr = 0.300;           % Readout duration time, [us]
n = 100000;           % Number of counts
muOn = 14.5;          % Gaussian mean value, ON
muOff = 0;            % Gaussian mean value, OFF
sigmaOn = 2.2;        % Gaussian standard deviation, ON
sigmaOff = 2.02;      % Gaussian standard deviation, OFF
nbins = 121;          % Number of voltage bins
start = -23.5;        % Voltage interval start [mV]
stop = 23.5;          % Voltage interval stop [mV]
piF = 0.955;          % Pi-pulse fidelity
nTime = 20;           % Number of time steps
Switchrate = 0.024/tr;% Rate of switching between pi-shifted states

fq = 4.8865e9;        % Qubit frequency
h = 6.62607e-34;      % Planck's constant
kb = 1.38065e-23;     % Boltzmann's constant

% --- Define Gaussian distributions and exponential decay ---
g=@(params,x)params(1)/(params(2)*sqrt(2*pi))*exp(-1/2*...
((x-params(3))/params(2)).^2);
f=@(t)(1-exp(-t/T1));
x=linspace(start-10,stop+10,1000);
t=linspace(0,5);
Time=linspace(td,td+tr,nTime);
TimeStep = Time(2)-Time(1);
gOn=g([1,sigmaOn,muOn],x);
gOff=g([1,sigmaOff,muOff],x);

% --- Define Boltzmann distribution for thermal exitation ---
fd=1/(exp(h*fq/(kb*T)));

% --- Monte Carlo simulation of events ---
On = zeros(1,n);
Off = On;

for j=1:n
    Qubit = 0;
    if rand>fd
        Qubit = 0; % Qubit in |0>
        if rand<piF
            Qubit = 1; % Qubit in |1> after pi-pulse
            if rand>f(td)
                Qubit = 1; % Qubit in |1> before readout
            else
                Qubit = 0; %Qubit in |0> before readout
            end
```

```
        else
            Qubit = 0; % Pi-pulse did not excite qubit
        end

        % Perform measurement
        if Qubit == 1
            Decayed = 0;
            Switched = 1;
            for i=1:length(Time) % Simulate relaxtion during readout
                if (rand>exp(-1/T1*TimeStep)*(1/T1*TimeStep) && Decayed == 0)
                    if rand<Switchrate*TimeStep
                        On(j) = On(j) + Switched*...
                        normrnd(muOn,sigmaOn*sqrt(length(Time)));
                        Switched = -Switched;
                    else
                        On(j) = On(j) - Switched*...
                        normrnd(muOn,sigmaOn*sqrt(length(Time)));
                    end
                else
                    Decayed = 1;
                    On(j) = On(j) + normrnd(muOff,sigmaOff*sqrt(length(Time)));
                end
            end

            if rand>1/2 %Simulate bi-stable
                On(j) = On(j)/length(Time);
            else
                On(j) = -On(j)/length(Time);

            end
        else
            On(j) = normrnd(muOff,sigmaOff);
        end
        Off(j) = normrnd(muOff,sigmaOff);

    else
        Qubit = 1; % Qubit thermally populated
        if rand>piF
            Qubit = 1; % Pi-pulse did not work
            if rand>f(td)
                Qubit = 1; % Qubit did not relax before readout
                Decayed = 0;
                Switched = 1;
                for i=1:length(Time) % Simulate relaxtion during readout
                    if (rand>exp(-1/T1*TimeStep)*(1/T1*TimeStep) && Decayed == 0)
                        if rand<Switchrate*TimeStep
                            On(j) = On(j) + Switched*...
                            normrnd(muOn,sigmaOn*sqrt(length(Time)));
                            Switched = -Switched;
                        else
                            On(j) = On(j) - Switched*...
                            normrnd(muOn,sigmaOn*sqrt(length(Time)));
                        end
                    else
                        Decayed = 1;
                        On(j) = On(j) + normrnd(muOff,sigmaOff*sqrt(length(Time)));
```

```
                    end
                end
                if rand>1/2 %Simulate bi-stable
                    On(j) = On(j)/length(Time);
                else
                    On(j) = On(j)/length(Time);
                end
            else
                Qubit = 0; %Qubit relaxed before readout
                On(j) = normrnd(muOff,sigmaOff);
            end
        else
            Qubit = 0; % Pi-pulse worked
            On(j) = normrnd(muOff,sigmaOff);
        end

        % No pi-pulse
        if rand>f(td)
            Qubit = 1; % Qubit didn't relax before readout
            Decayed = 0;
            Switched = 1;
            for i=1:length(Time) % Simulate relaxtion during readout
                if (rand>exp(-1/T1*TimeStep)*(1/T1*TimeStep) && Decayed == 0)
                    if rand<Switchrate*TimeStep
                        Off(j) = Off(j) + Switched*...
                        normrnd(muOn,sigmaOn*sqrt(length(Time)));
                        Switched = -Switched;
                    else
                        Off(j) = Off(j) - Switched*...
                        normrnd(muOn,sigmaOn*sqrt(length(Time)));
                    end
                else
                    Decayed = 1;
                    Off(j) = Off(j) + normrnd(muOff,sigmaOff*sqrt(length(Time)));
                end
            end
            if rand>1/2 %Simulate bi-stable
                Off(j) = Off(j)/length(Time);
            else
                Off(j) = -Off(j)/length(Time);
            end
        else
            Qubit = 0; %Qubit relaxed before readout
            Off(j) = normrnd(muOff,sigmaOff);
        end
    end
end

% --- Define plot parameters ---
bins = linspace(start,stop,nbins);
nOn = hist(On,bins);
nOff = hist(Off,bins);

POn=zeros(1,(length(bins)-1)/2+1);
POff=POn;
for k = 1:length(POn)
```

```
    POn(k) = sum(nOn((length(bins)-1)/2-k+2:(length(bins)-1)/2+k))/n;
    POff(k) = sum(nOff((length(bins)-1)/2-k+2:(length(bins)-1)/2+k))/n;
end
Fidelity = abs(POn-POff);

% --- Import data ---

FileName = 'PXI_ParametricOscillatorReadout_0.95V_FidelityRegionSearch_...
LineCutHist_0.25dBm_Pump.hdf5';
Traces=double(hdf5read(FileName,'/Traces/Digitizer 1 - Voltage mean unaveraged'));
Data=double(hdf5read(FileName,'/Data/Data'));
PumpPower = 0.250;
PumpFrequency = 5.208E9:(5.225E9-5.208E9)/170:5.225E9;
TraceOn = 2*42-1+(2*1-2)*length(PumpFrequency);
TraceOff = 2*42-1+(2*1-2)*length(PumpFrequency)+1;

% --- Complex representation of the ON and OFF traces
Z_On = complex(squeeze(Traces(TraceOn,1,:)),squeeze(Traces(TraceOn,2,:)));
Z_Off = complex(squeeze(Traces(TraceOff,1,:)),squeeze(Traces(TraceOff,2,:)));

% Extract the I and Q vectors
I_On = real(Z_On);
Q_On = imag(Z_On);

I_Off = real(Z_Off);
Q_Off = imag(Z_Off);

% Find the angle needed to rotate the data down on the real axis
CorrAngle = angle(mean(abs(I_On)) + 1j.*mean(abs(Q_On)));
Z_On = Z_On.*exp(1j*(pi/2-sign(mean(I_On.*Q_On)).*CorrAngle));
Z_Off = Z_Off.*exp(1j*(pi/2-sign(mean(I_On.*Q_On)).*CorrAngle));

ImOn = imag(Z_On)*1e3;
ImOff = imag(Z_Off)*1e3;

% Construct 1D histograms of the projected complex data
[hOn,xOn] = hist(ImOn,bins);
[hOff,xOff] = hist(ImOff,bins);

figure()
semilogy(xOff,hOff,'bo')
hold on
semilogy(xOn,hOn,'ro')
semilogy(bins,nOn,'r')
semilogy(bins,nOff,'b')

xlabel('Voltage [mV]')
ylabel('Counts')
legend('W/o \pi-pulse', 'With \pi-pulse')
fixFig(20,20,18,18)
hold off
```

Bibliography

[1] R. P. Feynman. Simulating Physics with Computers. *Int. Jour. of Th. Phys.*, 21:467–488, 1982.

[2] David P Divincenzo. The Physical Implementation of Quantum Computation. *Fortschritte der Physik*, (48), 2000.

[3] A. Blais, R-S. Huang, A. Wallraff, S. M. Girvin, and R. Schoelkopf. Cavity quantum electrodynamics for superconducting electrical circuits: An architecture for quantum computation. *Phys. Rev. A*, 69(6):062320, 2004.

[4] A. Wallraff, D. I. Schuster, A. Blais, L. Frunzio, J. Majer, S. Kumar, S. M. Girvin, and R. J Schoelkopf. Strong coupling of a single photon to a superconducting qubit using circuit quantum electrodynamics. *Nature*, 431:162–167, 2004.

[5] K. H. Onnes. The Superconductivity of Mercury. *Comm. Phys. Lab. Univ. Leiden*, 122:251, 1911.

[6] R. P. Feynman. *Lectures on physics*, volume vol III. Pearson Addison-Wesley, 2006.

[7] M. Tinkham. *Introduction to superconductivity*, volume 2nd edition. Dover Publications Inc., 2004.

[8] T. van Duzer and C. W. Turner. *Principles of superconductive devices and circuits*, volume 2nd edition. Prentice Hall PTR, 1999.

[9] B. D. Josephson. Possible new effects in superconductive tunnelling. *Phys. Lett.*, 1:251, 1962.

[10] C. P. Wen. Coplanar Waveguide: A Surface Strip Transmission Line Suitable for Nonreciprocal Gyromagnetic Device Applications. *IEEE Transactions on Microwave Theory and Techniques*, MTT-17:12, 1969.

[11] D. M. Pozar. *Microwave engineering*, volume 3rd edition. John Wiley and sons, inc., 2005.

[12] P. A. M. Dirac. The quantum theory of the emission and absorption of radiation. *Proc. Roy. Soc.*, A114:243, 1927.

[13] A. Einstein. Strahlungs-emission und -absorption nach der quantentheorie. *Verhandlungen der Deutschen Physikalischen Gesellschaft*, 18:318–323, 1916.

[14] S-I. Tomonaga. On a relativistic invariant formulation of the quantum theory of wave fields. *Progress of Theoretical Physics*, 1:27, 1946.

[15] J. Schwinger. On quantum-electrodynamics and the magnetic moment of the electron. *Phys. Rev.*, 73:416, 1948.

[16] R. P. Feynman. Space-time approach to non-relativistic quantum mechanics. *Rev. Mod. Phys.*, 20:367, 1948.

[17] S. Haroche and D. Kleppner. Cavity quantum electrodynamics. *Physics Today*, 42:24, 1989.

[18] S. Haroche and J-M. Raimond. *Exploring the Quantum: Atoms, Cavities, and Photons*. Oxford University Press Inc., New York, USA, 2006.

[19] Duty T. Wilson, C. M. and P. Delsing. *Fluctuating Nonlinear Oscillators, Edited by M. Dykman*. Oxford Univ. Press, 2012.

[20] B. Yurke and J. S. Denker. Quantum network theory. *Phys. Rev. A*, 29(3-4 PART 2):(3), 1419–1437, 1984.

[21] W. Wustmann and V. Shumeiko. Parametric resonance in tunable superconducting cavities. *Phys. Rev. B*, 87:184501, 2013.

[22] K. Sundqvist, S. Kintaş, M. Simoen, P. Krantz, M. Sandberg, C. M. Wilson, and P. Delsing. The pumpistor: a linearized model of a flux-pumped superconducting quantum interference device for use as a negative-resistance parametric amplifier. *Appl. Phys. Lett.*, 103:102603, 2013.

[23] M. Wallquist, V. Shumeiko, and G. Wendin. Selective coupling of superconducting charge qubits mediated by a tunable stripline cavity. *Phys. Rev. B*, 74(22):224506, 2006.

[24] M. A. Castellanos-Beltran and K. W. Lehnert. Widely tunable parametric amplifier based on a superconducting quantum interference device array resonator. *Appl. Phys. Lett.*, 91:083509, 2007.

[25] T. Yamamoto, K. Inomata, M. Watanabe, K. Matsuba, T. Miyazaki, W. D. Oliver, Y. Nakamura, and J. S. Tsai. Flux-driven Josephson parametric amplifier. *Appl. Phys. Lett.*, 93:042510, 2008.

[26] M. Sandberg, C. M. Wilson, F. Persson, T. Bauch, G. Johansson, V. Shumeiko, T. Duty, and P. Delsing. Tuning the field in a microwave resonator faster than the photon lifetime. *Appl. Phys. Lett.*, 92:203501, 2008.

[27] M. Faraday. *Philosophical Transactions of the Royal Society (London)*, 121:299–318, 1831.

[28] L. D. Landau and E. M. Lifshitz. *Mechanics, 3rd edition*. Elsevier Science, 1982.

[29] B. Yurke, P. G. Kaminsky, R. E. Miller, E. A. Whittaker, A. D. Smith, A. H. Silver, and R. W. Simon. Observation of 4.2-K equilibrium-noise squeezing via a Josephson-parametric amplifier. *Phys. Rev. Lett.*, 60(9):764–767, 1988.

[30] A. Palacios-Laloy, F. Nguyen, F. Mallet, Patrice Bertet, D. Vion, and D. Esteve. Tunable resonators for quantum circuits. *J. Low Temp. Phys.*, 151(3-4 PART 2):1034–1042, 2008.

[31] E. A. Tholen, A. Ergul, E. M. Doherty, F. M. Weber, F. Gregis, and D. B. Haviland. Nonlinearities and parametric amplification in superconducting coplanar waveguide resonators. *Appl. Phys. Lett.*, 90:253509, 2007.

[32] B. Huard. *Quantum information with superconducting circuits.* Systemes mesoscopiques et effet Hall quantique Ecole Normale Superieure de Paris - ENS Paris, 2014.

[33] N. Roch, E. Flurin, F. Nguyen, P. Morfin, P. Campagne+Ibarcq, M. H. Devoret, and B. Huard. Widely Tunable, Nondegenerate Three-Wave Mixing Microwave Device Operating near the Quantum Limit. *Phys. Rev. Lett.*, 108:147701, 2012.

[34] M. H. Devoret. *Les Houches, session LXIII.* Elsevier Science, 1995.

[35] S. H. Strogatz. *Nonlinear dynamics and chaos.* Addison-Wesley Publishing Company, USA, 1994.

[36] M. I. Dykman, C. M. Maloney, V. N. Smelyanskiy, and M. Silverstein. Fluctuational phase-flip transitions in parametrically driven oscillators. *Phys. Rev. E*, 57(5):5202–5212, 1998.

[37] C. M. Wilson, T. Duty, M. Sandberg, F. Persson, V. S. Shumeiko, and P. Delsing. Photon Generation in an Electromagnetic Cavity with a Time-Dependent Boundary. *Phys. Rev. Lett.*, 105(23):233907, 2010.

[38] K. M. Sundqvist and P. Delsing. Negative-resistance models for parametrically flux-pumped superconducting quantum interference devices. *EPJ Quantum Technology*, 1(1):6, 2014.

[39] J. Koch, T. M. Yu, J. Gambetta, A. A. Houck, D. I. Schuster, J. Majer, A. Blais, M. H. Devoret, S. M. Girvin, and R. J. Schoelkopf. Charge-insensitive qubit design derived from the Cooper pair box. *Phys. Rev. A*, 76(4):042319, 2007.

[40] M. Büttiker. Role of quantum coherence in series resistors. *Phys. Rev. B*, 33:3020, 1986.

[41] Y. Nakamura, Y. A. Pashkin, and J. S. Tsai. Coherent control of macroscopic quantum states in a single-Cooper-pair box. *Nature*, 398:786–788, 1999.

[42] K. Bladh, T. Duty, D. Gunnarsson, and P. Delsing. The single Cooper-pair box as a charge qubit. *New Journal of Physics*, 7:180, 2005.

[43] D. Vion, A. Aassime, A. Cottet, P. Joyez, H. Pothier, C. Urbina, D. Esteve, and M. H. Devoret. Manipulating the quantum state of an electrical circuit. *Science*, 296:886, 2002.

[44] A. R. Lide. *Handbook of chemistry and physics, 85^{th} edition.* CRC Press LLC, 2004.

[45] J. Bardeen, L. N. Cooper, and J. R. Schrieffer. Theory of superconductivity. *Phys. Rev.*, 108:1175, 1957.

[46] E. T. Jaynes and F. W. Cummings. Comparison of quantum and semiclassical radiation theories with application to the beam maser. *Proc. IEEE*, 51:(1): 89–109, 1963.

[47] C. C. Gerry and P. L. Knight. *Introductory Quantum Optics.* Cambridge University Press, Cambridge, England, 2005.

[48] D. I. Schuster, A. Wallraff, A. Blais, L. Frunzio, R.-S. Huang, J. Majer, S. M. Girvin, and R. J. Schoelkopf. ac Stark Shift and Dephasing of a Superconducting Qubit Strongly Coupled to a Cavity Field. *Phys. Rev. Lett.*, (94):123602, 2005.

[49] A. Fragner, M. Goppl, J. M. Fink, M. Baur, R. Bianchetti, P. J. Leek, A. Blais, and A. Wallraff. Resolving Vacuum Fluctuations in an Electrical Circuit by Measuring the Lamb Shift. *Science*, (322):1357, 2008.

[50] R. Vijay, D. H. Slichter, and I. Siddiqi. Observation of Quantum Jumps in a Superconducting Artificial Atom. *Phys. Rev. Lett.*, 106(11):110502, 2011.

[51] E. Jeffrey, D. Sank, J. Y. Mutus, T. C. White, J. Kelly, R. Barends, Y. Chen, Z. Chen, B. Chiaro, A. Dunsworth, A. Megrant, P. J. O'Malley, C. Neill, P. Roushan, A. Vainsencher, J. Wenner, A. N. Cleland, and J. M. Martinis. Fast accurate state measurement with superconducting qubits. *Phys. Rev. Lett.*, 112(19):257402, 2014.

[52] Z. R. Lin, K. Inomata, W. D. Oliver, K. Koshino, Y. Nakamura, J. S. Tsai, and T. Yamamoto. Single-shot readout of a superconducting flux qubit with a flux-driven Josephson parametric amplifier. *Appl. Phys. Lett.*, 103(13):132602, 2013.

[53] Z. R. Lin, K. Inomata, K. Koshino, W. D. Oliver, Y. Nakamura, J. S. Tsai, and T. Yamamoto. Josephson parametric phase-locked oscillator and its application to dispersive readout of superconducting qubits. *Nature Commun.*, 5(2):4480, 2014.

[54] A. Lupascu, S. Saito, T. Picot, P. C. de Groot, C. J. P. M. Harmans, and J. E. Mooij. Quantum non-demolition measurement of a superconducting two-level system. *Nature Phys.*, 3(2):119–125, 2007.

[55] F. Mallet, F. R. Ong, A. Palacios-Laloy, F. Nguyen, P. Bertet, D. Vion, and D. Esteve. Single-shot qubit readout in circuit quantum electrodynamics. *Nature Phys.*, 5(11):791–795, 2009.

[56] K. W. Murch, E. Ginossar, S. J. Weber, R. Vijay, S. M. Girvin, and I. Siddiqi. Quantum state sensitivity of an autoresonant superconducting circuit. *Phys. Rev. B*, 86(22):220503, 2012.

[57] M. D. Reed, L. DiCarlo, B. R. Johnson, L. Sun, D. I. Schuster, L. Frunzio, and R. J. Schoelkopf. High-fidelity readout in circuit quantum electrodynamics using the jaynes-cummings nonlinearity. *Phys. Rev. Lett.*, 105(17):173601, 2010.

[58] M. Boissonneault, J. M. Gambetta, and A. Blais. Improved superconducting qubit readout by qubit-induced nonlinearities. *Phys. Rev. Lett.*, 105(10):100504, 2010.

[59] N Bergeal, F Schackert, M Metcalfe, R Vijay, V E Manucharyan, L Frunzio, D E Prober, R J Schoelkopf, S M Girvin, and M H Devoret. Phase-preserving amplification near the quantum limit with a Josephson ring modulator. *Nature*, 465(7294):64–68, 2010.

[60] I. Siddiqi, R. Vijay, F. Pierre, C. M. Wilson, M. Metcalfe, C. Rigetti, L. Frunzio, and M. H. Devoret. RF-Driven Josephson Bifurcation Amplifier for Quantum Measurement. *Phys. Rev. Lett.*, 93(20):207002, 2004.

[61] I. Siddiqi, R. Vijay, F. Pierre, C. M. Wilson, L. Frunzio, M. Metcalfe, C. Rigetti, R. Schoelkopf, M. H. Devoret, D. Vion, and D. Esteve. Direct Observation of Dynamical Bifurcation between Two Driven Oscillation States of a Josephson Junction. *Phys. Rev. Lett.*, 94(2):027005, 2005.

[62] M. A. Castellanos-Beltran, K. D. Irwin, G. C. Hilton, L. R. Vale, and K. W. Lehnert. Amplification and squeezing of quantum noise with a tunable Josephson metamaterial. *Nature Phys.*, 4:929–931, 2008.

[63] V Schmitt, X Zhou, K Juliusson, B Royer, A Blais, P Bertet, D Vion, and D Esteve. Multiplexed readout of transmon qubits with Josephson bifurcation amplifiers. *Phys. Rev. A*, 90:062333, 2014.

[64] R. N. Simons. *Coplanar Waveguide Circuits, Components, and Systems*. John Wiley & Sons, 2001.

[65] P. Krantz, Y. Reshitnyk, W. Wustmann, J. Bylander, S. Gustavsson, W. D. Oliver, T. Duty, V. Shumeiko, and P. Delsing. Investigation of nonlinear effects in Josephson parametric oscillators used in circuit quantum electrodynamics. *New J. Phys.*, 15(10):105002, 2013.

[66] F. Cuccureddu, S. Murphy, I. V. Shvets, M. Porcu, H. W. Zandbergen, N. S. Sidorov, and S. I. Bozhko. Surface morphology of c-plane sapphire (α-alumina) produced by high temperature anneal. *Surface Science*, 604(15-16):1294–1299, 2010.

[67] S. Curiotto and D. Chatain. Surface morphology and composition of c-, a- and m-sapphire surfaces in O2 and H2 environments. *Surface Science*, 603(17):2688–2697, 2009.

[68] Primož Rebernik Ribič and Gvido Bratina. Behavior of the (0 0 0 1) surface of sapphire upon high-temperature annealing. *Surface Science*, 601(1):44–49, 2007.

[69] G. J. Dolan. Offset masks for lift-off photoprocessing. *Appl. Phys. Lett.*, 31:337, 1977.

[70] J. G. Simmons. Generalized Formula for the Electric Tunnel Effect between Similar Electrodes Separated by a Thin Insulating Film. *Journal of Applied Physics*, 34(6):1793–1803, 1963.

[71] V. Da Costa, C. Tiusan, T. Dimopoulos, and K. Ounadjela. Tunneling phenomena as a probe to investigate atomic scale fluctuations in metal/oxide/metal magnetic tunnel junctions. *Physical Review Letters*, 85(4):876–879, 2000.

[72] E. Z. Luo, S. K. Wong, a. B. Pakhomov, J. B. Xu, I. H. Wilson, and C. Y. Wong. Tunneling current and thickness inhomogeneities of ultrathin aluminum oxide films in magnetic tunneling junctions. *Journal of Applied Physics*, 90(10):5202–5207, 2001.

[73] K. Gloos, P. J. Koppinen, and J. P. Pekola. Properties of native ultrathin aluminium oxide tunnel barriers. *Journal of Physics: Condensed Matter*, 15(10):1733–1746, 2003.

[74] G. K. White and P. Meeson. *Experimental techniques in low-temperature physics*. 4th Edition. OUP Oxford, 2002.

[75] V. E. Manucharyan, E. Boaknin, M. Metcalfe, R. Vijay, I. Siddiqi, and M. H. Devoret. Microwave bifurcation of a Josephson junction: Embedding-circuit requirements. *Phys. Rev. B*, 76:014524, 2007.

[76] P. Bertet, F. R. Ong, M. Boissonneault, A. Bolduc, F. Mallet, A. C. Doherty, A. Blais, D. Vion, and D. Esteve. *Fluctuating Nonlinear Oscillators, Edited by M. Dykman*. Oxford Univ. Press, 2012.

[77] M. D. Reed, B. R. Johnson, A. A. Houck, L. Dicarlo, J. M. Chow, D. I. Schuster, L. Frunzio, and R. J. Schoelkopf. Fast reset and suppressing spontaneous emission of a superconducting qubit. *Appl. Phys. Lett.*, 96(20):203110, 2010.

[78] E. A. Sete, J. M. Martinis, and A. N. Korotkov. Quantum theory of a bandpass Purcell filter for qubit readout. *Phys. Rev. A*, 92(1):012325, 2015.

Appended papers